THE STABILITY AND WALL STRUCTURE
OF CYLINDRICAL DOMAINS
IN MAGNETIC FILMS

By

Ⓒ TERENCE GERARD WREFERD BLAKE, B.Sc., M. Eng.

A Thesis

Submitted to the School of Graduate Studies

in Partial Fulfillment of the Requirements

for the Degree

Doctor of Philosophy

McMaster University

October 1980

CYLINDRICAL DOMAINS IN MAGNETIC FILMS

DOCTOR OF PHILOSOPHY (1980)
(Physics)

McMASTER UNIVERSITY
Hamilton, Ontario

TITLE: The Stability and Wall Structure of Cylindrical Domains in Magnetic Films

AUTHOR: Terence Gerard Wreferd Blake, B.Sc. (University of Calgary)

M.Eng. (McMaster University)

SUPERVISOR: Professor E. Della Torre

NUMBER OF PAGES: 160

ACKNOWLEDGEMENTS

I would very much like to thank Dr. Edward Della Torre for his continued encouragement and support, and for many important suggestions and much helpful technical advice.

I would also like to express my appreciation for many productive discussions with Dr. Waguih S. Ishak and Dr. C.C. Shir, and for advice and guidance from Drs. C.V. Stager and B.K. Garside, the members of my thesis committee.

Special gratitude is due Dr. C.A. Baker for assistance in the preparation of this document, and for great encouragement throughout the course of the work.

I wish to thank also Marilyn Mlynek for typing the manuscript with precision and for doing revisions under difficult circumstances.

ABSTRACT

A model is presented of a cylindrical domain ("magnetic bubble") with its wall in a uniaxially anisotropic magnetic film, and data obtained from this model's numerical implementation are analyzed.

A finite-difference, static energy minimization, micromagnetic model [23] of an axisymmetric domain wall in a magnetic film has been further developed in its physical formulation and numerical techniques. The various contributions to total energy calculated from the resulting magnetic configuration have been applied to the determination of average domain radius by means of an energy-minimization domain model developed for the purpose. The domain radius was needed to complete the wall-model algorithm and to allow it to converge to an accurate solution. This thesis describes the two aspects of this theoretical analysis, the wall model and the domain model, and the interaction between them.

The entire algorithm has been used to model magnetic bubbles in systematic surveys of applied magnetic fields and of film material parameters, namely saturation magnetization M_s, normalized anisotropy constant Q, and normalized wall energy density of bulk material, λ. Structural features of the resulting wall magnetic configurations are displayed. A comprehensive selection of features are quantified and their dependence on domain radius and on material parameters are presented and their physical explanations are discussed. Domain stability properties are derived from the theoretical model and their dependence on material parameters is analyzed.

TABLE OF CONTENTS

FIGURES

TABLES

SYMBOL DEFINITIONS

See also section 1.2.

Section	Symbol	Definition
2.1.1	α	azimuthal angle of position. $\hat{\alpha}$: unit vector.
2.1.1	ϕ	azimuthal angle of magnetization orientation.
2.1.1	θ	polar angle of magnetization orientation.
3.2	Δr	$= r_o - r_g$; should be small.
1.3.1	a	$= 2r/T$; variational aspect ratio of thin-walled bubble of radius r.
3.1	a_o	$= 2r_o/T$; bubble aspect ratio.
7.2	a_c	aspect ratio at bubble collapse.
2.2.3	$\bar{D}$	demagnetization field geometrical factor (matrix).
2.2.3	$\hat{D}$	primitive functions for demagnetization factors $\bar{D}$.
2.2.3	$\bar{d}$	integrand in demagnetization factor $\bar{D}$.
2.1.2	d_r, d_z	dimensions of grid cells (Figure 2.2).
2.2.1	dV_i	volume of i^{th} cell of grid.
2.2.5	E_d	grid region self-demagnetizing energy.
2.2.5	E_f	energy of grid region due to $\vec{H}_f$.
2.2.1	E_{Ku}	energy of grid region due to uniaxial anisotropy.
2.2.4	E_x	energy of grid region due to exchange interaction.
5.5	HBL	horizontal Bloch line.
	$\vec{h}$	$= \vec{H}/M_s$, normalized field; depends on subscript.
2.2.2	$\vec{H}_B$	applied external (bias) field.

2.2.5	$\vec{H}_d$	grid region self-demagnetizing field.
2.2.5	$\vec{H}_f$	stray (fringing) field from domain regions.
2.2.4	$\vec{H}_x$	exchange equivalent field.
7.2	H_c	bias field at bubble collapse.
7.2	H'_c	Thiele-theory collapse field.
2.2.4	K_{ur}	$= K_u + A/r_j^2$; coefficient of anisotropy and axisymmetric exchange energies.
6.1	l_{BL}	$= (2A/\mu_o M_s^2)^{\frac{1}{2}}$; nominal Bloch line width.
1.3.2	l_w	$= \pi(A/K_u)^{\frac{1}{2}}$; classical Bloch wall width
2.1.1	$\vec{M}$	magnetization vector.
2.1.1	$\hat{m}$	unit vector in direction of magnetization.
2.1.1	m_r, m_α, m_z	components of $\hat{m}$.
2.2.3	p_j	$= r_j/r_i$; relative radius of source point.
3.2	Δr	$= r_o - r_g$; should be small.
2.1.1	r	distance from bubble axis. $\hat{r}$: unit vector.
3.2.1	r_e	radius of exterior radial boundary of grid.
2.1.2	r_g	radius of centre of grid.
2.2.3	$\vec{r}_i$	position of field point, centre of cell i.
3.2.1	r_i	radius of inner boundary of grid region.
2.2.3	r_{ji}	$= \lvert\vec{r}_i - \vec{r}_j\rvert$, distance from one point to another.
2.2.4	r_j	radius of centre of j^{th} column of grid.
3.1	r_o	radius at which $m_z = 0$, $\theta = \pi/2$, averaged over the film thickness.
2.2.3	s_j	$= (z_i - z_j)/r_i$; reduced z-coordinate of source point.
2.1.1	z	distance from film midplane. $\hat{z}$: unit vector.

CHAPTER 1

INTRODUCTION AND BACKGROUND

The purposes of this thesis are: to derive a model of cylindrical magnetic domains and their micromagnetic wall structures in films; to elaborate numerical implementations of each aspect of the model; to present data obtained by applying the model to sets of film material parameters and applied magnetic fields; and to discuss physical explanations of the results.

The rest of this chapter describes in general terms the cylindrical domains and the related "magnetic bubble" technology, the conventional material parameters and their relations to domain and wall structure, and previous theoretical work in the study of magnetic bubbles and domain walls.

Chapter 2 describes the finite-difference, iterative, micromagnetic energy-minimization model of the thick, axisymmetric wall. Chapter 3 presents the new model of the domain, in which energies computed from the wall configuration are used to find a total-energy minimum nearby in radius; the accurate radius is required for convergence by the cylindrical wall model. Chapter 4 discusses the numerical methods used in the iterative calculations of Chapter 2.

Chapters 5, 6 and 7 present results of computer runs. Chapter 5 gives an overview of wall structure, with maps of various kinds. Chapter 6 concentrates on the dependence of measurable quantities of wall structure on domain aspect ratio and on certain film material parameters. Chapter 7 shows how the model can be used to predict domain stability limits and then does so for the ranges of material parameters of Chapter 6. In Chapter 8 we draw conclusions from the work and suggest some possible future investigations.

The numerical data in Chapters 6 and 7 are in dimensionless units. The material parameters presented in section 6.1, and the theoretical treatments of Chapters 2 and 3 are in rationalized MKS units [22].

Symbol definitions may be found in the table in the front matter, or in section 1.2; otherwise, they are used only locally within a section.

1.1 MAGNETIC DOMAINS IN UNIAXIAL THIN FILMS

This section will describe the phenomena that result in magnetic bubble technology [16].

If a thick (1 - 6 micron garnet) film has uniaxial magneto-crystalline anisotropy, its easy axis perpendicular to the film plane, the magnetization tends to lie along that axis, up or down. The magnetization is normally discouraged from being in the same direction all over an entire film (about 1 cm. square) by its own magnetic field. This demagnetizing field is considerably reduced when the film spontaneously divides into domains, one set magnetized up and the other down. The resulting pattern has the form of a maze of meandering stripes. See Figure 1.1; here,

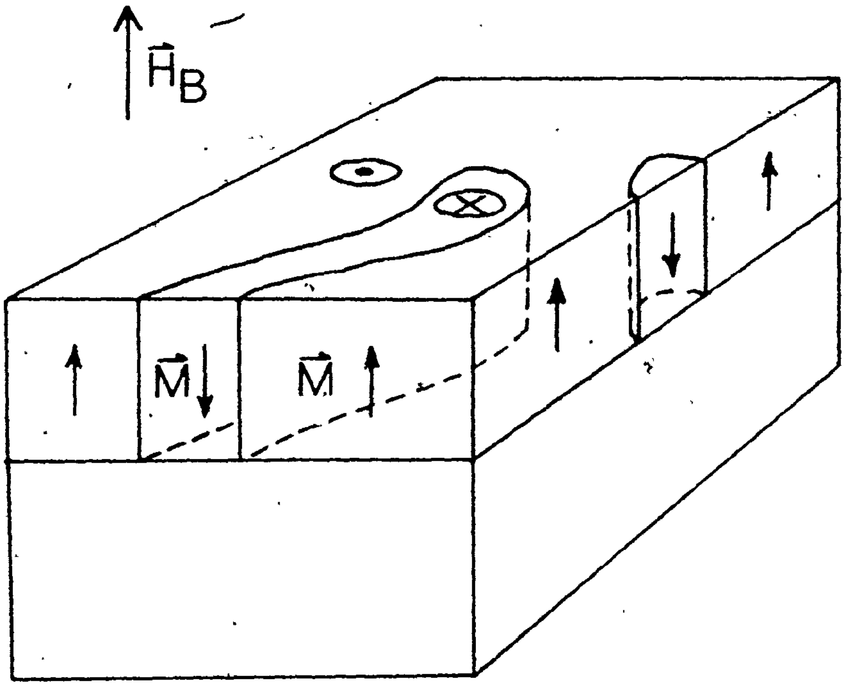

Fig. 1.1 Uniaxial magnetic film with stripe domains, on a nonmagnetic substrate.

the demagnetizing field is biased by the external field H_B (see below).

At the atomic level, the magnetic moments are held closely parallel by the quantum-mechanical exchange interaction. This means that the moments are parallel in stripe regions as wide as the demagnetizing field effect will allow. The stripes are separated by wall regions in which the magnetization direction is gradually reversed from one side to the other (see Fig. 1.2). At the centre of the wall and the centre of the film, the magnetization must lie in the planes of both; this is called a Bloch wall structure. At the junctions of the central region of the wall and the film surfaces, the local demagnetizing field tends to reorient the magnetization part of the way toward the wall normal. Wall magnetization along the wall normal would be called a Néel wall structure. The width and internal structure of the walls (plus such material dynamic parameters as the spin precession damping coefficient and the coercivity) determine the properties of wall motion.

From a stripe pattern, bubbles may be produced by the application of a magnetic field (a bias field) directed normal to the film. The magnetization tends to lie along the direction of the bias field so the wall regions move to make one set of stripes wider at the expense of the other set (Fig. 1.1). Under increasing bias, the latter set of stripes shorten as well, and suddenly shrink to circles. Over a range of bias field strengths, the circular magnetic bubbles are stable, decreasing in diameter with in-

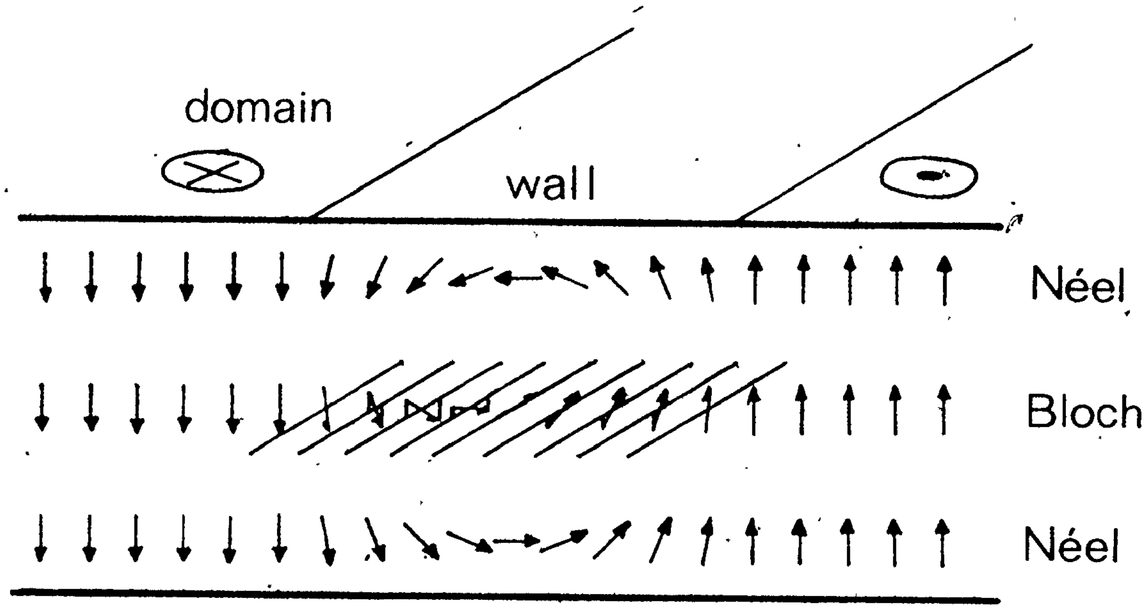

Fig. 1.2 Wall between two domains in a uniaxial magnetic film.

creasing bias field. The former set of stripes, whose magnetization was parallel to the bias field - the bubbles' magnetization is anti-parallel - will have grown together to fill the film outside the bubbles.

If the bias field is increased further, beyond a limit characteristic of the film, the bubbles collapse and disappear. In technologically useful films, the widths of stable bubbles (and zero-bias stripes) are the same order of magnitude as the film thickness.

Given an overall bias field in the range of bubble stability, if a local field can be applied at an edge of a bubble, the bubble wall there will move. If the local field is parallel to the bias field on one side of the bubble, and anti-parallel to it on the other, the wall moves inward on the former side and outward on the latter, so the bubble itself moves.

The usual way these local fields are produced in bubble devices is by means of shaped mesas of magnetic metal ($Ni_{.8}Fe_{.2}$, permalloy) deposited on the surface of the film. As shown in Fig. 1.3, the permalloy elements have shape details even smaller than the bubbles they are to manipulate.

An applied field H_{xy} in the film plane will not normally move domain walls, but it will magnetize the permalloy shapes, whose demagnetizing fields are sufficiently localized that they move the bubbles short distances. If the direction of the drive field is changed slightly, still in the film plane, the permalloy stray field distribution changes so that the bubble is moved

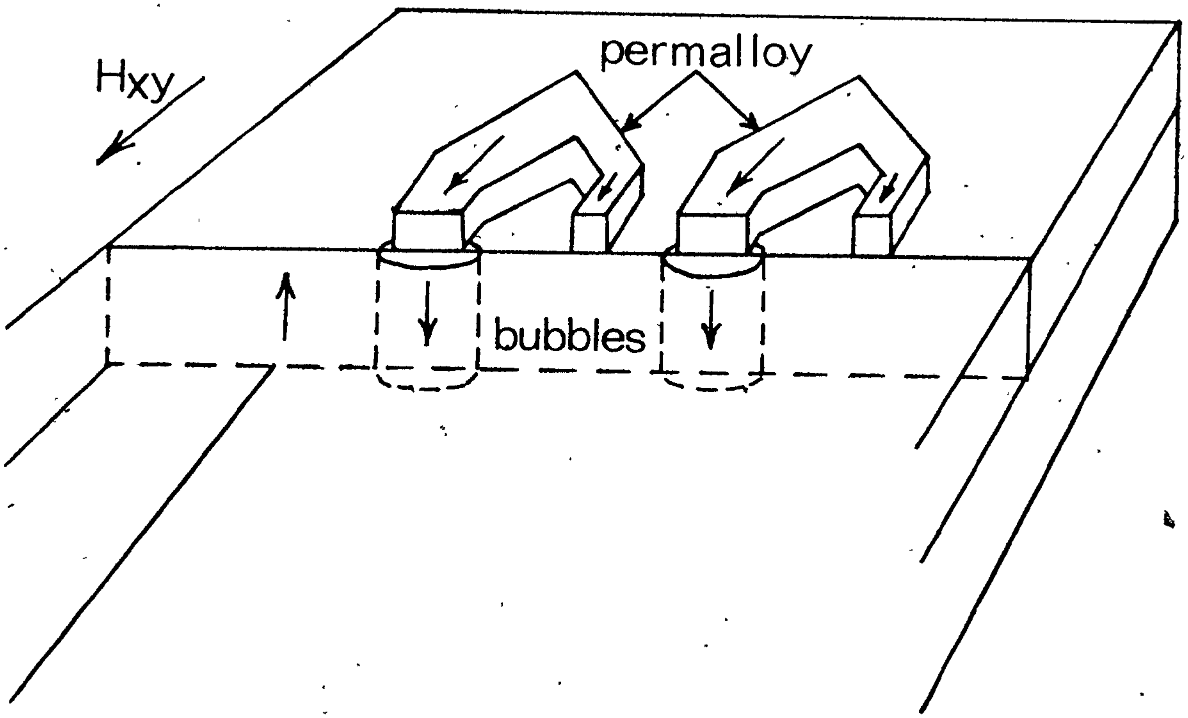

Fig. 1.3 Bubble film with permalloy propagation elements.

another short distance. When the direction of the drive field is rotated continuously, the bubble moves through the pattern of permalloy with a speed determined by the pattern's period, and limited by the bubble's wall structure and by the gyromagnetic properties of the film material. In commercially available devices, the rotating field frequency is of the order of 10^5 cps; higher-frequency designs are presently in the research stage.

The permalloy pattern defines a storage of information in which a position contains a binary "1" if occupied by a bubble, a binary "0" if not. Information may be written into this memory by creating bubbles, and leaving spaces, in a propagating stream. One way bubbles are generated is by cutting an elongated seed bubble with a local field, parallel to the bias field, produced by a pulse of current in a conductor deposited on the film surface.

Bubbles may be detected, and thus information read from the memory, by the change in current measured in a permalloy conductor as the bubbles pass it. The resistance of the conductor changes in the presence of the stray field of a bubble.

On a memory chip, bubbles also have occasion to be switched from one path to another and to be split (replicated). These functions are accomplished by conductors (1-3 microns wide) aligned with permalloy configurations. The details of the permalloy and conductor shapes must be carefully optimized [16].

The foregoing is a description of the conventional features of bubble memory devices; however, wholly different but promising alternative approaches to each aspect are under active consideration in industry [16,36]. The subject of this thesis is a computer model of magnetic bubbles themselves and especially their wall structures. The thesis will describe the model and its predictions of the dependence of wall structure and domain stability on bubble size and on film material parameters.

1.2 MATERIAL PARAMETERS AND WALL STRUCTURE

This section will outline how the properties of the bubbles that occur in a film are related to parameters that characterize the film. The present work assumes a simple, homogeneous film, without effects of commonly employed processes such as ion implantation or permalloy thin film deposition. A magnetic film is described by quoting its thickness and a set of material parameters, which set may be chosen from the following list (the choice made in the present work will be given in section 6.1):

M_s	(Amp/m; Oe) saturation magnetization.
K_u	(J/m^3); erg/cm^3) coefficient of energy density associated with the magneto-crystalline uniaxial anisotropy (section 2.2.1).
H_K	$= 2\ K_u/\mu_o M_s^2$ (Amp/m; Oe) equivalent field of the uniaxial anisotropy interaction.
Q	$= H_K/M_s$; normalized anisotropy coefficient.
A	(J/m; erg/cm) coefficient of exchange interaction (section 2.2.4).
l_w	$= \pi\sqrt{A/K_u}$ (m; cm); classical width of a 180-

degree Bloch wall occurring in bulk material.

σ_A = $4\sqrt{AK_u}$ (j/m^2; erg/cm^2); energy density associated with a Bloch wall.

λ = $\sigma_A/\mu_o M_s^2$ (m; cm); the characteristic length of the material.

λ/T normalized material length.

Stable bubble radii are directly related to the normalized material length, λ/T; the Thiele analysis [51] of this subject, including the limits of stability of bubble domains, will be discussed in section 1.3.1. In practice, λ/T is controlled primarily by the selection of M_s; smaller bubbles require a larger M_s. However, a large M_s also implies a small Q, which may mean the stability of the bubble is inadequate. If Q is less than unity, the magnetization is expected to lie in the plane of the film so bubbles would not exist.

High Q is associated with low-mobility domain walls because large K_u implies a narrow wall width l_w. Wall mobility depends on the magnetic moments in the film reorienting themselves as the wall region passes their locations. A given speed of reorientation corresponds to a given time for passage of a wall region, so a wide wall will move faster than a narrow one, under a given applied field, damping parameter, and coercivity.

If a lower Q is obtained by means of an increased M_s at the same K_u and bubble diameter, the increase in A needed to maintain λ/T fixed will result in a larger wall width, l_w. The stronger exchange interaction holds the moments more closely parallel so the transition region between domains, the wall, is broader. (In section 6.1, the selection of sets of material parameters for the present study are shown to be based on considerations of this kind.)

This simplified analysis, the one usually made, assumes a Bloch wall. In fact, the stray fields from the magnetization in the vicinity of the wall change the wall structure by twisting the magnetization near the film surface away from the wall tangent, and also by broadening the wall profile there.

For a steady-state wall structure, it is clearly the narrowest part of the wall that determines the wall velocity. The wall twist, together with oscillatory and transient features of wall dynamics further complicate the motion of wall and bubble domains. However, the present work is devoted to the study of non-Bloch wall structures and their static effects on domain stability and expected quasi-static motion.

1.3 PREVIOUS WORK

Most analyses of magnetic domain problems have focussed on the structure of the domain wall. However, the early basic theoretical work on magnetic bubbles, due to A.A. Thiele and described in section 1.3.1, assumed a thin wall whose structural details are inconsequential. It is the treatment most often referred to in practice by those involved in magnetic bubble technology.

In section 1.3.2 are discussed some of the other treatments, the wall models. The following properties will be identified for each:

1. Its dimensionality - both that inherent in the theory and that actually implemented in the published results.
2. The extent to which it is analytic, variational (Ritz method), or discretized grid (finite difference).
3. Whether its physical formulation is static (energy or torque minimization) or dynamic (Landau-Lifshitz-Gilbert equation).
4. The major approximations made, e.g., separation of variables, assumption of a limited width of the wall region, etc.

1.3.1 Thiele's Domain Theory.

The principal analysis of magnetic bubble stability was due to A.A. Thiele [50,51,9]. We will discuss his treatment in some detail because the development of our radius calculation in Chapter 2 is based on similar principles. Also, the bubble stability results of Chapter 5 will be understood by reference to Thiele's analysis.

Thiele let the walls between domains be thin (infinite ratio of anisotropy to exchange), and ignored their variable structure, characterizing them by a single material-dependent parameter, the Bloch wall surface energy density, σ_w. The domain shape is given by the radius function,

$$r(\alpha) = r_o + \Delta r_o + \sum_{n=1}^{\infty} \Delta r_n \cos\left[n(\alpha-\alpha_n-\Delta\alpha_n)\right]. \qquad (1.1)$$

The stability of the domain with respect to changes in size, Δr_o, and shape, Δr_n, is given by the appropriate variations of the total energy. The zero-order term is associated with bubble size and stability against collapse, the first-order term with elliptical distortion (stripe-out), and so on. For circular bubbles, the first derivative of the total energy with respect to radius is given by (MKS units)

$$\frac{\partial E}{\partial a} = \pi\, T^2\, [\sigma_A + \mu_o M_s^2 (aT\, \frac{H_B}{M_s} - T\, F(a)] \ , \qquad (1.2)$$

where a = 2r/T is the aspect ratio of the bubble, F(a) is a function of the complete elliptic integral of the second kind, and the three terms on the right refer to the wall energy, the Zeeman energy due to the bias field, and the demagnetizing energy. Correspondingly, the second derivative is

$$\frac{\partial^2 E}{\partial a^2} = \pi T^3\, \mu_o M_s^2\, (\frac{H_B}{M_s} - \frac{dF}{da}) \ . \qquad (1.3)$$

Bubble stability criteria may be understood with the help of Fig. 1.4 [9]. The bubble aspect ratio is determined by the vanishing of the first derivative, Eq. (1.2) a condition equivalent to

$$\frac{H_B}{M_s} = (F(a) - \lambda/T) \ / \ a \ . \qquad (1.4)$$

For the aspect ratio to be stable against collapse, it is required that

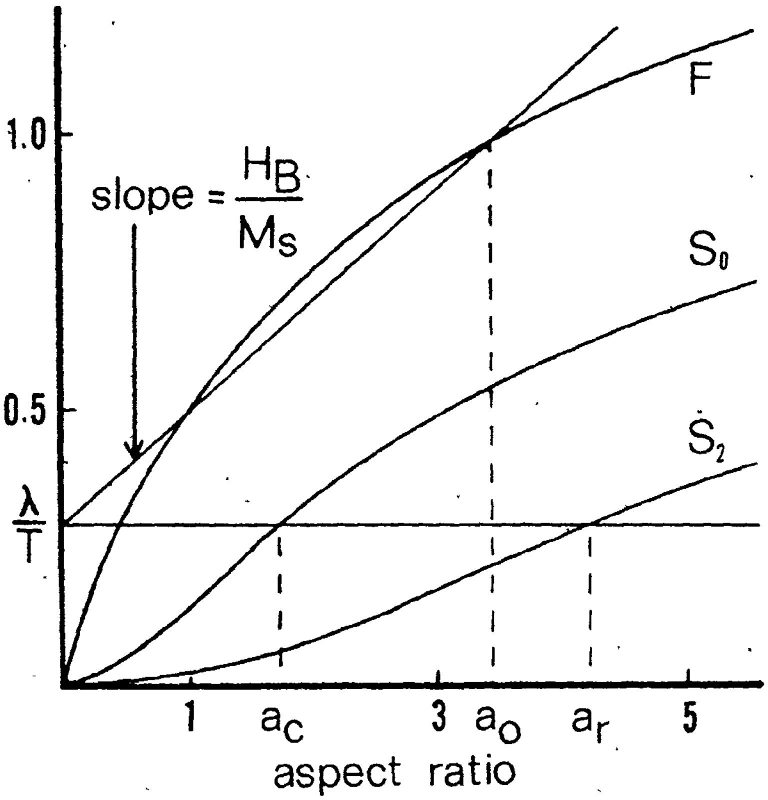

Fig. 1.4 Schematic graphical analysis of bubble stability [9,51].

$$\frac{H_B}{M_s} - \frac{dF}{da} > 0 \qquad (1.5)$$

from Eq. (1.3). Defining

$$S_o(a) = F(a) - a\,\frac{dF}{da} \quad , \qquad (1.6)$$

we have for this condition, using Eq. 1.4,

$$\lambda/T < S_o(a) \ . \qquad (1.7)$$

Other functions $S_n(a)$ were defined and led to the conditions for stability against distortions of order n:

$$\lambda/T > S_n(a). \qquad (1.8)$$

The axisymmetric model presented in this thesis is not sensitive to elliptical (n=2) and higher-order distortions.

The functions F(a), $S_o(a)$, and $S_n(a)$ together with the above stability conditions, have provided a sound basic understanding of magnetic bubbles. Graphical [9] and numerical [31] implementations of the theory have made it even more illuminating and useful. However, its underlying approximations compromise the accuracy of the results obtained, especially in low-Q garnet films. One purpose of this thesis work is to determine appropriate corrections for bubble materials of current interest.

1.3.2 Wall Models and Solutions.

The structure of magnetic domain walls is on a scale between that of domains and that of atomic moments. Theoretical investigation at this scale is properly governed by the discipline of micromagnetics, a field associated with W.F. Brown [12, 11]. The micromagnetic principle that magnetization is a continuous vector function, equal in magnitude to the saturation value characteristic of the material, has been respected in the work to be described in this section. The nonlocal nature of the demagnetizing field interaction [1], however, was in some cases neglected in favor of a local approximation to facilitate analysis or computation.

Ferromagnetic domain wall theory began with the derivation by F. Bloch [8] of the properties of a plane wall in an infinite medium. In this one-dimensional situation, the magnetization lies in the plane of the wall so that demagnetizing fields are eliminated. Minimizing the total of the exchange and anisotropy energies [17], we arrive at the well-known profile of the polar angle in a Bloch wall centred at x_o,

$$\theta = 2 \tan^{-1} \exp[(x_o - x) \sqrt{K_u/A}] \tag{1.9}$$

The wall width and surface energy density (section 1.2) follow from this expression.

Tu [53] developed a direct energy-minimization scheme for the magnetization configuration of a bubble, and Lin and Tu [35] published results in the form of computed energies for a bubble having a one-dimensional Bloch wall.

DeBonte [19] presented a variational model of a thick-walled static bubble; the Bloch-wall polar angle function was modified to have suitable behavior near the bubble axis. He then [20] computed the stability properties of such a bubble.

Slonczewski [46,47,37] derived the forms of moving twisted walls whose width was much less than both the domain size and the thickness of the (high Q) film. He made the further approximations that the stray field due to the film surfaces of the neighboring domains depended only on z within the wall region, and that the azimuthal angle did not vary with position perpendicular to the wall. This is equivalent to a local approximation for the magnetostatic interaction within the wall. The subsequent calculation was an analytical solution of the equations of motion derived from the Landau-Lifshitz-Gilbert equation. It led to a study of Bloch lines (see section 5.5) within domain walls and their influence on anomalous motion of the walls.

This local approximation approach was pursued variationally by Hubert [30], who studied thinner films of lower Q. Schlömann [39,40] developed a variational formulation of the structure of isolated plane walls in films. The azimuthal twist was constrained to have the form of a sine function. He derived the structures of walls in thick films of general Q [41] and in stripe-domain structures [42].

DeBonte [21] also carried out a variational calculation for static stripe domains with twisted walls. Polar and azimuthal angles were each constrained to Jacobian elliptic functions of one position variable. Detailed results on the dependence of wall structure quantities on film material parameters were presented.

Computers have often been used to determine magnetic configurations by the repetitive application of physically simple calculations, with arbitrarily small approximations, to the discrete values of functions defined over a region of space. Most discretized-grid wall calculations [24] have been finite-difference, rather than finite-element, and they have been two-dimensional rather than three, to limit computation time. The latter characteristic has meant that the wall studied was plane, the elementary grid cells being cylinders of rectangular cross-section, infinite in the direction parallel to the wall and the film.

Examples are the work of LaBonte [34] on thin metal (e.g., permalloy) films, and Henry and Brown [29] and Shir [43] on garnet bubble films. Shir's model was dynamic, a time integration based on torques calculated from the Landau-Lifshitz-Gilbert equation; the others involved the determination of the static energy minimum at each grid cell.

These computations strike a compromise between having a grid much wider than the expected wall width, and having a cell width small enough to resolve the centre of the wall. A grid width equal to three times the classical Bloch wall width ($l_w = \pi\sqrt{K_u/A}$) is typical. In the past, published domain-wall models have not used non-uniform grids [7], nor adaptive grid-reconstruction during the computation (this work), nor a coarse grid for the demagnetizing field and a fine one for the other interactions (this work).

The choice of grid width is related to the boundary conditions at the sides of the grid. While other models set the magnetization there to coincide with the direction in the adjacent structured domains, Shir [43] implemented variable boundary conditions by postulating a Bloch-wall profile containing the computed θ-value just inside the grid.

A model presented by Della Torre, Hegedus, and Kadar [23] utilized demagnetizing factors derived for rings of rectangular cross-section [28,32,27], thereby studying closed axisymmetric walls. This is a three-dimensional situation described by two spatial co-ordinates. The wall configuration was determined by the zeroing of static energy derivatives. The wall-configuration relaxation in the present work was developed from this model.

CHAPTER 2

THE PHYSICAL MODEL OF THE DOMAIN WALL

The basic model of the wall was developed [23] prior to the present work. It is described in this chapter, with modifications noted. Modifications are associated principally with section 2.3 on boundary conditions, section 2.4 on initial conditions, section 2.5 on grid adjustments, and with Chapter 4 on numerical methods.

2.1 OVERVIEW

2.1.1 Co-ordinate System and Symmetries.

We shall locate a point in space by its cylindrical coordinates, (r, α, z). Since the magnetization in the film has fixed magnitude, equal to its saturation value, M_s Amp./m, it is specified by its orientation angles:

$$\vec{M} = M_s\ \hat{m}(\theta,\phi) \tag{2.1}$$

$$= M_s\ (\sin\theta\ \cos\phi\ \hat{r} + \sin\theta\ \sin\phi\ \hat{\alpha} + \cos\theta\ \hat{z}), \tag{2.2}$$

where $\hat{r}$ and $\hat{\alpha}$ are functions of α.

The z-axis (r=0) coincides with the bubble axis. The magnetization is axisymmetric:

$$\theta(r,\alpha,z) = \theta(r,0,z) \tag{2.3}$$

$$\phi(r,\alpha,z) = \phi(r,0,z) \tag{2.4}$$

The bubble is discretized as a collection of rings, as depicted in Fig. 2.1. Within each elementary cell, θ and ϕ are fixed (ϕ is measured everywhere from the radial direction, Eq. (2.2)).

We also assume symmetry about the film midplane (at z=0):

$$\theta(r,\alpha,z) = \theta(r,\alpha,-z), \tag{2.5}$$

$$\phi(r,\alpha,z) = \pi - \phi\,(r,\alpha,-z). \tag{2.6}$$

Eq. (2.6) means that $\phi(r,\alpha,0) = \pm\,\pi/2$; exactly at the midplane of the film, the wall is of the Bloch type (section 1.3.2).

2.1.2 The Grid.

Figure 2.2 is a schematic diagram of the grid, laid over a cross-section of the bubble cut radially from its axis.

The interior of the bubble is a right circular cylinder, which is a special case of an elementary ring whose inside radius is zero; the domain exterior to the bubble is a ring whose inside radius is finite and whose outside radius approaches infinity. The grid over the wall region will be about 3 l_w wide; how the grid width and radius are reset during the computation will be discussed in section 3.5.

As shown in Fig. 2.2, the grid is two-tier. The fine cells each contain a uniform magnetization and are used in the finite-difference calculations of the exchange interaction, the anisotropy and bias field interactions, and the relaxation of the magnetization orientation. The coarse cells are used in the calculation of the demagnetizing factors and fields, because the calculation time increases as the square of the number of cells involved.

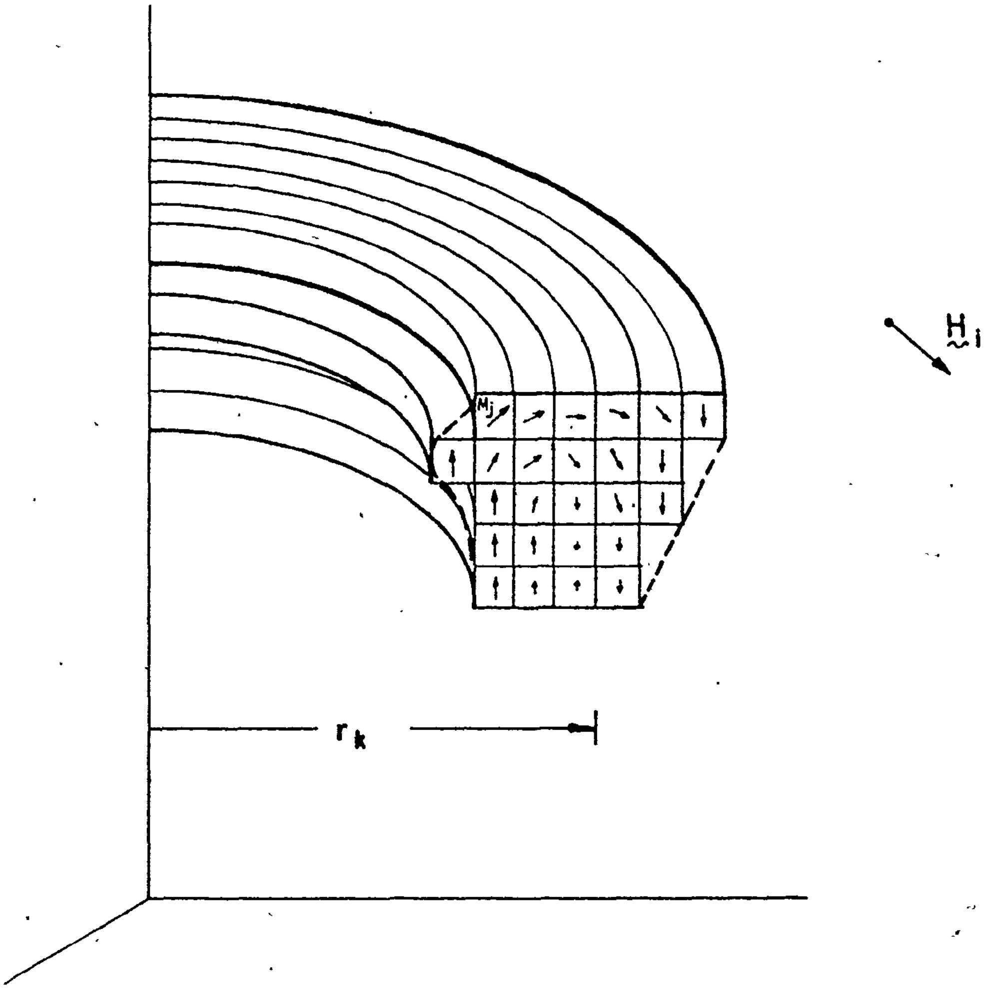

Fig. 2.1 Elementary volumes, each containing uniform axisymmetric magnetization [28].

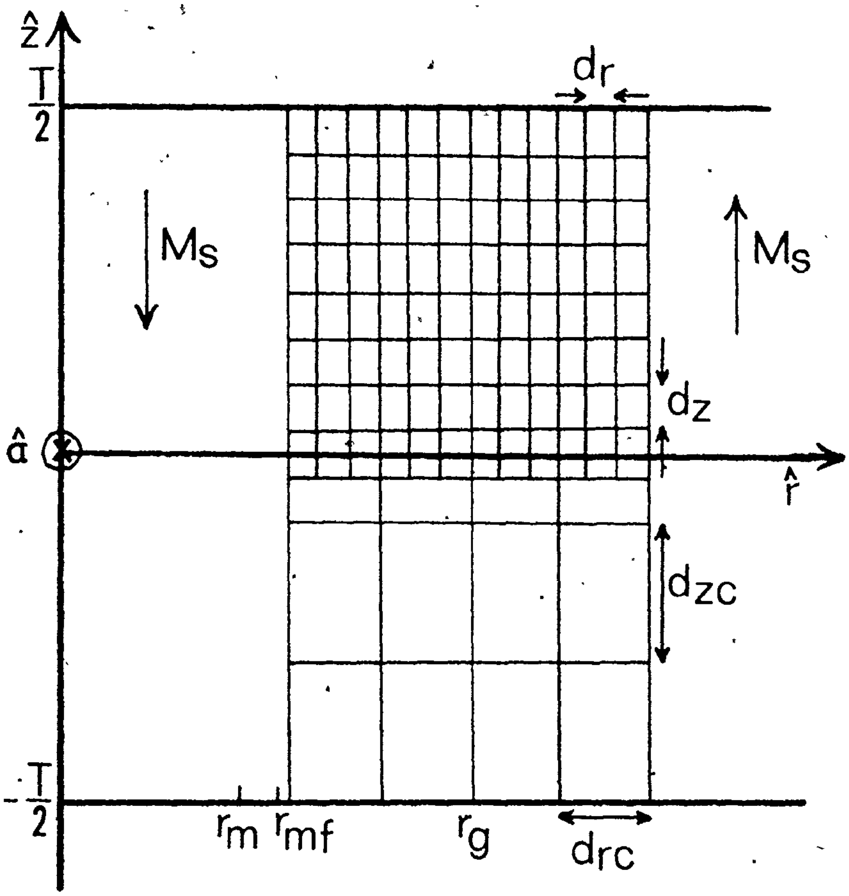

Fig. 2.2 The discretized grid for the finite-difference and demagnetizing field calculations.

Each coarse row and column contains an odd number of fine rows and columns, respectively. In the present work, the coarse grid is 10 columns by 13 rows and the fine grid is 30 columns by 20 rows, so the fine grid has three times the resolution of the coarse grid. Due to symmetry, the fine grid covers only the upper half of the wall region; the centres of the bottom fine row and the middle coarse row coincide at z=0.

The demagnetizing field was calculated exactly (section 2.2.3) only in the upper half of the coarse grid, ten rows by seven columns, but all the coarse grid cells were sources for the field. The computation time for an entire iteration, including calculation of all fields and magnetization reorientation, was reduced by a factor of nearly eight from what it was when the demagnetizing factors and field were calculated on the fine grid.

Finally, we note that the field points are at the centres of cells, while the film surface coincides with the upper surfaces of the cells of the top row.

2.1.3 Summary of the Algorithm.

The magnetic configuration in the wall region is found iteratively. For each fine grid cell the following is done:

The demagnetizing field and the exchange field are calculated and added to the bias field. The ϕ for the cell is reset to equal the azimuthal angle of this local total equivalent field. The θ is reset by locating the nearest zero of the first variation of the total bubble energy. The total energy is the sum of the Zeeman energy due to the total equivalent field (section 2.2.5) and the uniaxial anisotropy energy.

The cells of each column are scanned from the film surface to the midplane. The columns are scanned from the edges of the grid toward its centre (see section 4.2). The largest change in orientation found at any of the cells is compared to a fixed criterion. If the criterion is still smaller, the scan of the grid is repeated; if not, the algorithm has converged, and further interactions would have negligible effect on the magnetization configuration.

The entire numerical algorithm has a nested structure. After the wall configuration is relaxed by a number of iterations, energies are computed and a new domain radius is calculated. At this point, the grid may be adjusted to cover the wall configuration better. Then the relaxation iterations are run again, with new domain stray fields and other changes associated with the grid being at a new radius. When both the relaxation algorithm and the radius calculation call for no further significant changes, the solution is established.

2.2 SOURCES OF ENERGY

2.2.1 Uniaxial Anisotropy.

In rare-earth iron garnet bubble films, the easy axis, perpendicular to the film plane, is produced primarily by the ordering of the mixed rare-earth ions on their possible crystal sites during liquid epitaxial growth [9, p. 120]. This growth anisotropy is typically much greater than the stress anisotropy, which arises from a lattice-spacing mismatch between the film and the non-magnetic substrate. We neglect the residual cubic anisotropy, which for a (111)-oriented film causes a three-fold in-plane symmetry [36].

The uniaxial anisotropy energy of the i^{th} cell, of volume dV_i, is

$$(dE_{Ku})_i = K_u \sin^2 \theta_i \, dV_i \ . \tag{2.7}$$

2.2.2 Bias Field.

The externally-applied bias field is uniform in magnitude throughout the film and oriented in the positive z direction:

$$\vec{H}_B = M_s \, h_B \, \hat{z}. \tag{2.8}$$

The energy of the magnetization of cell i, in the presence of this field, is

$$(dE_B)_i = -\mu_o \, M_s^2 \, \vec{h}_B \cdot \hat{m}_i \, dV_i . \tag{2.9}$$

2.2.3 Demagnetizing Fields.

The self-demagnetizing field of the film containing domains and a wall is calculated as the magnetostatic field at each point due to the magnetization at each other point [10]. The microscopic calculation [11, p. 32] is approximated by the discretization into cells of uniform magnetization. The following discussion is a summary of [28].

In general [22, p. 505],

$$\vec{H}(\vec{r}_i) = - \frac{1}{4\pi} \, \text{grad}_i \left\{ \int_{\substack{\text{all}\\\text{space}}} \vec{M}_j \cdot \text{grad}_j \frac{1}{r_{ji}} \, dv_j \right\}, \tag{2.10}$$

where $\vec{r}_i$ is the field point and $\vec{M}_j$ is at a source point. Given our collection of axisymmetrically magnetized rings, it was possible to derive demagnetizing factors $\bar{D}$, each dependent only on the geometry, relative to the field point $\vec{r}_i$, of an individual ring, as depicted in Fig. 2.3. The field to one ring is then

$$\vec{H}\,(\vec{r}_i) = \bar{D}\,\vec{M}_j. \tag{2.11}$$

$\bar{D}$ is a matrix operator given by

$$\bar{D} = \frac{1}{4\pi} \int_{\alpha_i}^{\alpha_i+2\pi} d\alpha_j \int_{r_1}^{r_2} dr_j \int_{z_1}^{z_2} dz_j\, \bar{d}(\vec{r}_j,\vec{r}_i), \tag{2.12}$$

where, from Eq. (2.10), with $\vec{M}_j$ axisymmetric over V_j,

$$\vec{H}(\vec{r}_i^{\,o}) = -\frac{1}{4\pi}\left[\int_{V_j} \frac{\bar{d}}{r_j r_i^2}\, dv_j\right] \vec{M}_j^{o}. \tag{2.13}$$

where the superscript 0 refers to α=0.

Defining relative variables,

$$p_j = r_j \,/\, r_i\,, \tag{2.14}$$

$$s_j = (z_i - z_j) \,/\, r_i\,, \tag{2.15}$$

$\bar{D}$ may be written (letting α_i be 0),

$$\bar{D} = \frac{1}{4\pi} \int_0^{2\pi} d\alpha \int_{p_1}^{p_2} dp \int_{s_1}^{s_2} ds\; \bar{d}\,(p,\, \alpha,\, s). \tag{2.16}$$

The elements of $\bar{d}$ were derived from Eqs. (2.10) and (2.13).

Due to cylindrical symmetry, the only nonzero elements of the 3x3 matrices $\bar{D}$ and $\bar{d}$ are the corner ones, those not referring to the α components of either $\vec{M}_j$ or $\vec{H}(\vec{r}_i)$.

Within a cell the magnetization is uniform in p(r) and

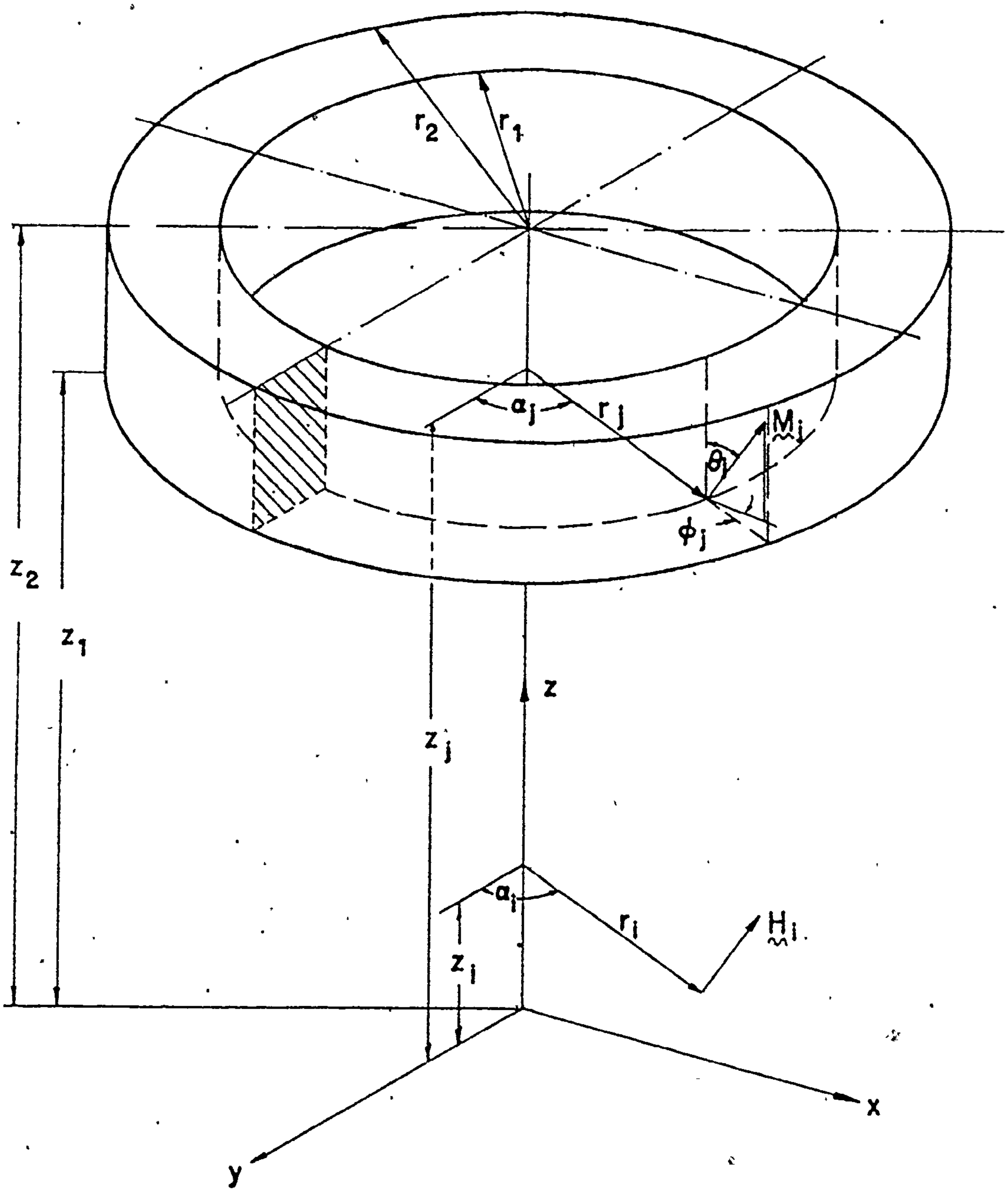

Fig. 2.3 Co-ordinate system for the geometrical demagnetizing factors [28].

in s(z), so a primitive function could be defined as

$$\hat{D}\ (p,s) = \frac{1}{4\pi}\int_{o}^{2\pi} d\alpha \int_{p_o}^{p} dp \int_{s_o}^{s} ds\ \bar{d}(p,\alpha,s), \qquad (2.17)$$

so that

$$\bar{D} = \hat{D}(p_1,s_1) - \hat{D}(p_1,s_2) - \hat{D}(p_2,s_1) + \hat{D}(p_2,s_2), \qquad (2.18)$$

where (p_o,s_o) is a point within the rectangle indicated in Eq. (2.18), and the integrated functions at (p_o,s_o) cancel.

Expressions for the components of $\hat{D}$ were derived in terms of complete elliptic integrals of the first, second, and third kinds; these integrals are evaluated [32] by algorithms due to Bulirsch [13]. The $\hat{D}$ components need be computed only once for a grid, whatever magnetic configuration it holds.

The primitive functions have important symmetries, of reflection in s and, of course, translation in z (Eq. (2.15)), and each grid cell has two primitive functions in common with each of its nearest neighbor cells. The computation and storage of demagnetizing factors are thus made more efficient by this approach.

Also, the primitive functions at the corners of the grid coincide with those of the two rings representing the domain regions. The other primitive functions for the domain rings, at r approaching zero and infinity, have simple limiting values [28]. Therefore, the demagnetizing fields from the domain regions, sometimes called stray or fringing fields, are conveniently calculated at each grid cell along with the wall region demagnetizing field.

Since the field points $\vec{r}_i$ are at the centres of cells and the primitive demagnetizing factors are evaluated with respect to the corners of cells, mathematical singularities do not arise. However, it is an approximation, especially when the cells j and at $\vec{r}_i$ coincide, to use a single value of $\bar{D}$, rather than integrating over $\vec{r}_i$ within the cell. In the worst case [28], when the cell is nearly square, D_{rr} and D_{zz} have maxima and minima, respectively, with respect to both r and z, near the centre of the cell, so even then they may compensate each other. In any case, the functions are not strongly varying. The approximation appears to be a reasonable one.

When the self-demagnetizing field of the wall region is calculated, each coarse cell is considered to have a uniform magnetization orientation equal to that of the fine cell at its centre. After the demagnetizing fields are calculated at the centres of the coarse cells over the upper half of the wall region, their values at the fine cells are interpolated, by a cubic spline along each column and linearly between one coarse column centre and the next.

2.2.4 Equivalent Field for Exchange Interaction.

Exchange is a quantum-mechanical interaction between the atomic spins that give rise to the magnetization itself. In bubble garnets, it aligns and contra-aligns the spins on the different crystal sites so that there is a net magnetization M_s. Where other magnetic interactions upset the parallelism of $\vec{M}$, there is an exchange energy density proportional to A, the exchange constant, which depends on the crystal structure and the atomic species.

The magnetic field which would produce at $\vec{M}$ a magnetostatic self-energy density equal to the exchange energy density is called the exchange field $\vec{H}_x$:

$$(dE_x)_i = -\tfrac{1}{2}\, \mu_o\, \vec{H}_x \cdot \vec{M}_i\, dV_i \tag{2.19}$$

The exchange field can be derived from differentiation of the exchange energy density [10,11,49]; the result is

$$\vec{H}_x\ \overbrace{(\vec{r}_i) = \frac{2A}{\mu_o M_s^2}\ \mathrm{grad}_i^2\, \vec{M}_i}, \tag{2.20}$$

which may be regarded as a phenomenological expression [11, p. 135]. In cylindrical co-ordinates,

$$\mathrm{grad}^2 = \frac{1}{r}\frac{\partial}{\partial r} + \frac{\partial^2}{\partial r^2} + \frac{1}{r^2}\frac{\partial^2}{\partial \alpha^2} + \frac{\partial^2}{\partial z^2}\ . \tag{2.21}$$

We represent the first, second, and fourth terms in Eq. (2.21) by central difference formulae referred to the grid cells (Fig. 2.2); with $\hat{m}_i = \vec{M}_i / M_s$, numbering columns j and rows k, and omitting second subscripts when they are j or k,

$$\begin{aligned}(\mathrm{grad}^2\, \hat{m})_{jk} = {} & \frac{1}{r_k}\,\frac{\hat{m}_{j+1}-\hat{m}_{j-1}}{2dr} + \frac{\hat{m}_{j+1}-2\hat{m}_j+\hat{m}_{j-1}}{dr^2} \\ & + \frac{\hat{m}_{k+1}-2\hat{m}_k+\hat{m}_{k-1}}{d_z^2}\end{aligned} \tag{2.22}$$

$$\begin{aligned} = {} & \frac{1}{d_r^2}\left[\left(1+\frac{d_r}{2r_j}\right)\hat{m}_{j+1} + \left(1-\frac{d_r}{2r_j}\right)\hat{m}_{j-1}\right] \\ & + \frac{1}{d_r^2}\left(\hat{m}_{k+1}+\hat{m}_{k-1}\right) \\ & - \frac{2}{d_r^2}\,\hat{m}_{jk} - \frac{2}{d_z^2}\,\hat{m}_{jk}\end{aligned} \tag{2.23}$$

In the variation of energy with θ_i, the last two terms of Eq. (2.23) (which are the central terms of the three-term finite differences of Eq. (2.22)) give the constant $\vec{M}_i \cdot \vec{M}_i = M_s^2$, so they are omitted. However, they are included in the calculation of energies for the domain radius variation.

There are no cell divisions in the α co-ordinate, so the third term from Eq. (2.21) is calculated separately. From this term is derived in the Appendix the energy density $(A/r^2)\sin^2\theta$ (see also [18]). Since this has the same θ dependence as the uniaxial anisotropy energy, Eq. (2.7), it is conveniently included by replacing K_u by $K_{ur} = K_u + A/r^2$. This change was made to the wall model for the present work.

The effect of the exchange contribution is to multiply K_u by

$$1 + \frac{A/r^2}{K_u} = 1 + \frac{l_w^2}{\pi^2 r^2} , \qquad (2.24)$$

so it is significant if the material's Bloch wall width is comparable to the bubble radius.

2.2.5 Definitions of Energies and Energy Variations.

When the total energy of the bubble is being computed (see Ch. 3), the formulas used are standard. The grid self-demagnetizing terms include a factor of ½ to allow for double counting:

$$E_d = -\tfrac{1}{2}\,\mu_o \int_{\text{grid}} \vec{H}_d \cdot \vec{M}\, dv \qquad (2.25)$$

$$= -\tfrac{1}{2}\,\mu_o\, M_s^2 \int_{grid} \vec{h}_d \cdot \hat{m}\, dv \qquad (2.26)$$

The terms from the domain regions' fringing field omit the factor of ½ on the basis of reciprocity [10]: the magnetostatic energy in the grid region due to the saturated regions is equal to the energy in the saturated regions due to the stray field from the grid region, and the latter energy must be included. Therefore,

$$E_f = -\,\mu_o\, M_s^2 \int_{grid} \vec{h}_f \cdot \hat{m}\, dv \qquad (2.27)$$

The applied bias field is from an external source, the energy of which matches the corresponding energy of the film material by the reciprocity principle. The bias field energy of the grid region is, therefore,

$$E_B = -\,\mu_o\, M_s^2 \int_{grid} \vec{h}_B \cdot \hat{m}\, dv \qquad (2.28)$$

The exchange energy is calculated from an equivalent field which acts on a grid cell to produce a self-energy, by the definition of $\vec{H}_x$ (Eq. (2.19)):

$$E_x = -\tfrac{1}{2}\,\mu_o\, M_s^2 \int_{grid} \vec{h}_x \cdot \hat{m}\, dv \qquad (2.29)$$

When the direction of $\vec{M}$ is varied during the relaxation of a cell (section 4.1), changes in the magnetostatic energy of the cell are matched, by reciprocity, by changes in the energies of the other grid cells, of the domain regions, and of the external magnet producing the bias field. Therefore, we consider the variations in

$$E_{di} = - \mu_o M_s^2 \int_{V_i} \vec{h}_d \cdot \hat{m}_i \, dv \tag{2.30}$$

and, still,

$$E_{fi} = - \mu_o M_s^2 \int_{V_i} \vec{h}_f \cdot \hat{m}_i \, dv, \tag{2.31}$$

$$E_{Bi} = - \mu_o M_s^2 \int_{V_i} \vec{h}_B \cdot \hat{m}_i \, dv. \tag{2.32}$$

The change in exchange energy of cell i due to a reorientation of $\hat{m}_i$ would be duplicated by changes in the exchange energies of the cell's nearest neighbors (Eq. (2.22)), if those energies were re-evaluated. Therefore, the appropriate expression is like that for the grid self-demagnetizing field (Eq. (2.30)),

$$E_{xi} = - \mu_o M_s^2 \int_{V_i} \vec{h}_x \cdot \hat{m}_i \, dv. \tag{2.33}$$

2.3 BOUNDARY CONDITIONS

Special consideration must be given to the columns at the edges of the grid and the row at the surface of the film. (The row at z=0 is treated according to the symmetries of θ and ϕ about z=0, section 2.1.1). These boundary conditions are needed primarily for computing the equivalent exchange field. The radial boundary conditions are also used in the mapping of a configuration to a new grid when it is found that the existing grid radius or width is unsuitable (section 3.5). The surface boundary conditions are also used in the extrapolation of surface values of quantities that describe wall structure (Chapters 5 and 6).

2.3.1 Film Surface Boundary Condition.

The magnetization at the surface of the film tends to be closely parallel to the magnetization just below the surface, due to the one-sided aligning exchange interaction. Therefore [10,43]

$$\left(\frac{\partial}{\partial z}\hat{m}\right)_{\text{surface}} = 0. \tag{2.34}$$

The second derivative of $\hat{m}$ at the top row of the grid, adjacent to the surface, is required for the exchange field. Numbering the top row n,

$$\left(\frac{\partial^2\hat{m}}{\partial z^2}\right)_n = \left[\left(\frac{\partial\hat{m}}{\partial z}\right)_{n+\frac{1}{2}} - \left(\frac{\partial\hat{m}}{\partial z}\right)_{n-\frac{1}{2}}\right]/d_z \tag{2.35}$$

where d_z is the cell height (Fig. 2.2), and the surface is one half cell above the centre of the top row. Now,

$$\left(\frac{\partial^2\hat{m}}{\partial z^2}\right)_n = [0 - (\hat{m}_n - \hat{m}_{n-1})/d_z]/d_z \tag{2.36}$$

$$= -(\hat{m}_n - \hat{m}_{n-1})/d_z^2 \tag{2.37}$$

This expression is equivalent to that obtained by differentiating a second-order polynomial fit through the two rows closest to the surface, constrained to have a vanishing derivative at the surface. A straightforward derivation may be applied to a third-order polynomial; the effect of the improved accuracy is to allow the surface effect (Eq. (2.34)) to be more localized at the surface, as is realistic. It was the third-order expression,

$$\left(\frac{\partial^2 \hat{m}}{\partial z^2}\right)_n = - \frac{24}{23} \frac{\hat{m}_n - \hat{m}_{n-1}}{d_z^2} - \frac{1}{23} \frac{m_n - 2m_{n-1} + m_{n-2}}{d_z^2} \qquad (2.38)$$

which was implemented in the present work.

The choice of surface boundary condition is important, because without it (letting $\vec{M}_{n+1} = 0$, [23]), the realistic magnetic configuration near the surface would not be obtained. This configuration is characterized (section 5.1, [43]) by the locally reduced gradients of the orientation angles; the θ-contours (Figs. 5.5, 5.6), otherwise flaring wider near the surface [23], curve back to be perpendicular to it, while the $\phi(z)$ profiles (Figs. 5.7, 5.8) also acquire an inflection in tending toward zero slope at the surface.

2.3.2 Radial Boundary Conditions.

Earlier finite difference calculations [34,23] have assumed "hard" boundary conditions: cells at the sides of the grid experienced exchange interactions directly with the saturated domains. The grid then had to be wide enough that the $\hat{m}_i$ in the border columns would appropriately undergo very little deviation from $\hat{m} = \pm \hat{z}$ in the adjacent domain regions. For a (computationally efficient) uniform grid, this would limit resolution where the magnetization gradients were large, especially when part of the wall was narrow and part flared (Ch. 5; [43]).

A way to give the treatment both realism and high resolution is to use a flexible boundary condition based on an expected magnetization profile, such as that of Shir [43]. In the present work, we do not assume a particular internal wall structure, but do define a function which takes values measured in the two columns nearest the side of the grid, and which approaches suitable limiting values as r approaches zero and infinity.

We consider the function

$$f(x) = \frac{\theta_e - \theta(x)}{r(x)} \tag{2.39}$$

where θ_e is the extreme value of $\theta(x)$: that is, $\theta_e=\pi$ when extrapolating at the inner radial boundary, $\theta_e=0$ when extrapolating at the outer one. The position variable x is measured in units of d_r from the centre of the second column in from the subject boundary, increasing toward the location of θ_e.

We intend to use the function of Eq. (2.39) to extrapolate $\theta(x)$ a short distance from the grid. We assume

$$f(x) = f(0)\ b^x\ , \tag{2.40}$$

where b is a constant; since Eq. (2.39) can be evaluated at cells in the column at the boundary (x=1) and in the next column (x=0),

$$b = \frac{\theta_e - \theta(1)}{r(1)} \cdot \frac{r(0)}{\theta_e - \theta(0)}\ . \tag{2.41}$$

Of course, $\theta(1)$ and $\theta(0)$ are evaluated separately for each row to be extrapolated. Solving Eqs. (2.39)-(2.40),

$$\theta(x) = \theta_e - [(\theta_e-\theta(0))(\frac{\theta_e-\theta(1)}{\theta_e-\theta(0)})^x(\frac{r(0)}{r(1)})^x \frac{r(x)}{r(0)}] \quad (2.42)$$

This expression is used when the configuration is to be mapped to a wider grid, or to a grid shifted in radius (section 2.5).

For the calculation of the exchange field at the boundary column by Eq. (2.23), we must extrapolate θ to an additional column just outside the grid, at x=2. From Eq. (2.42), and returning to the measurement of distance x in meters (but from the same origin),

$$\theta(2d_r) = \theta_e - \frac{(\theta_e-\theta(1d_r))^2}{\theta(0)-\theta_e} [1 - (\frac{d_r}{r(d_r)})^2] \quad (2.43)$$

The last factor on the right becomes important when the grid gets close to the bubble axis, where $\theta = \theta_e = \pi$. However, at the outer boundary of the grid, the profile extends to infinity and should not depend on grid radius in that way; therefore, by assuming $d_r << r$, we use a plane-wall extrapolation there.

As the magnetization is relatively close to the film perpendicular near the sides of the grid, the azimuthal angle φ becomes less important. The extrapolation of φ is according to the simple and conservative formula,

$$\phi(2) = \phi(1) + (\phi(1)-\phi(0)) + [\phi(1)-\phi(0)-(\phi(0)-\phi(-1))]. \quad (2.44)$$

2.4 INITIAL CONDITIONS

The algorithm begins with magnetization orientations present in the grid cells. One could have the initial $\hat{m}_i$ randomly oriented [34], but this would be prohibitively expensive in computation time. To ensure that the solution obtained is not at a false minimum of energy (that is, a minimum only because a significant parameter is constrained), we need to have adequate degrees of freedom in the calculation. This is accomplished in the present model by the inclusion of domain radius as a variable (Ch. 3).

An experimental run of the present computation, starting from an abrupt-transition wall,

$$\theta(r) = \pi/2 + (\pi/2)\ \mathrm{sign}\ (r_g - r), \tag{2.45}$$

was unstable near the centre of the grid at r_g. The conclusion was that a randomized start would also be non-converging.

However, when the initial $\theta(r)$ profile was linear, from π to zero, and the initial $\phi(z)$ profile was constant at zero, the result approached the one reached when a Bloch-wall profile for $\theta(r)$ and a linear twist in $\phi(z)$ were present. This encouraged the assumption subsequently made, that analytical theories give a configuration from which the true static minimum-energy configuration can be reached by continuous descent in energy [43]. A good initialization was considered to have little affect on the final result, but would eliminate many early iterations.

The initial $\theta(r)$ profile, obtained from DeBonte [19], was

$$\theta(r) = 2\tan^{-1}\exp[(r-r_g)/l_w] - \ln\frac{r}{r_g}\ , \tag{2.46}$$

where the last term removes a singularity in the exchange energy at $r=0$; the first term is the familiar Bloch-wall profile. Note that there is no width flaring near the film surface, and no radius bulging; θ is initially independent of z.

The initial twist function ϕ(z) was constructed from DeBonte's stripe-wall results [21,31]. His values of maximum twist at the surface and of z at half maximum were used in a formula for a smooth variation of ϕ. The function was independent of r.

The initial grid width was three times the width (section 5.1) measured from the θ profile, Eq. (2.46). The initial grid radius was found from Thiele's domain theory [51,9], using DeBonte's [21,31] wall energy density. However, before any wall-relaxation iterations were performed, the calculation of Ch. 3 was carried out to improve the estimate of the radius. If, during wall relaxation, the grid were allowed to be far from the domain radius suited to the energy of the current wall configuration, the stray fields from the domain regions might be so inappropriate that they would distort the wall configuration and the associated wall energy. Since that wall energy is important in the calculation of domain radius, the approach to the total solution of wall configuration and domain radius could be significantly delayed.

2.5 ADJUSTMENTS OF THE GRID

2.5.1 Relationships Between the Grid and the Wall Configuration.

After many iterations, the wall configuration differed considerably from its initial form. As flaring (section 5.4.3), bulging (section 5.4.2), and drifting (Ch. 3 introduction, section

3.4) appear, the original grid may become too narrow or not centred on the fringes of the broadest part of the wall. Simple calculations were developed for the present work to detect this situation (this section) and to correct it (section 2.5.2).

While the change of radius of section 3.4 involves varying the radii of the grid and wall configuration together, the radial adjustment considered here refers to the radius of the grid only; the grid is seen as a window through which some portion, ideally a central portion, of the wall is viewed.

The number of grid columns was fixed and the column widths were uniform. Therefore, the optimum grid width represented a compromise between adequate resolution in the vicinity of large magnetization gradient (near $\theta=\pi/2$), and inclusion of the wall fringes, where the magnetization was still oriented significantly away from the film perpendicular. The latter condition also determines the position of the centre of the grid with respect to the configuration - the magnetization should be oriented equally far from the film plane in each of the two edge columns.

Values of θ were chosen from the Bloch-wall formula,

$$\theta_{edge} = 2 \tan^{-1} \exp[\pm \frac{3}{2} (\frac{13}{15} \frac{\pi}{2})] \qquad (2.47)$$

where half the nominal grid width is about 3/2 the material Bloch wall width. The resulting values of θ_{edge} were $0.082\ \pi$ and $0.918\ \pi$. The radial locations of these values in the wall configuration were found for each row, and a grid width and centre radius were calculated to put the θ_{edge} values at the border columns. This, then, was a minimum advisable grid width, w_{min}.

On the other hand, a maximum advisable column width was calculated from a criterion, $(\Delta\theta)_c$, for the maximum difference between neighboring values of θ. The value of $(\Delta\theta)_c$ was 0.11 π.

It was decided to give more weight to w_{min}, allowing a large $\Delta\theta$ if need be [29]. The desired grid width was chosen to be

$$w_g = \max\,(w_{min},\ (w_{min} + w_{max})/2). \tag{2.48}$$

2.5.2 Mapping the Wall to a New Grid.

If the grid width was not suited to the width of the wall configuration (section 2.5.1), or if the grid was not centred on the wall where the wall was widest, then a new grid had to be laid down on the existing wall configuration. The z_k of the new rows would be the same as the old, but the r_j of the new columns would be different.

To avoid losing the accuracy achieved after many iterations in the old grid, cubic spline interpolations along each row were used to obtain initial values of the new θ_{jk}, ϕ_{jk} from the old ones. The θ_{jk}, ϕ_{jk} for columns that lay outside the region of the old grid were extrapolated according to the radial boundary conditions of Eqs. (2.42) and (2.44). To avoid extrapolation errors, the displacement of the new grid from the old was limited.

CHAPTER 3

DOMAIN ENERGY ANALYSIS

Each iteration of the wall relaxation will slightly translate the θ-profile in the grid toward the correct domain radius associated with the minimum total energy. The slowness of this effect can be understood by analogy with stiff differential equations [26]; the displacement of the domain wall appears to have a much larger duration of relaxation (cf. time constant) than does the reconfiguration of the internal structure of the wall.

In any case, the wall configuration must not be permitted to propagate a significant amount out of the grid, lest errors grow and wall structure information be lost. To avoid this situation and to speed solution, we periodically recalculate the minimum-energy bubble radius and reset the grid radius accordingly. The formulation and implementation of this procedure is the subject of this chapter.

Given a wall configuration in the grid, we minimize the total system energy with respect to the domain radius, which is defined as the radius, averaged over z, of the wall centre. We intend to make a small adjustment to the grid radius, conceptually shifting the entire configuration in or out along with it.

We require an approximate formula for the first variation of the total energy with radius, so that the nearest zero of this variation, taking the sign of the second variation into account, is the desired radius.

We choose a second-order approximation for the energy, compatible with a second-order Taylor series for the magnetostatic energy. Although we will apply the approximation only locally in radius, the dependence of energy on bubble radius has the overall appearance of a cubic function [35, 37 p. 20, 15]. Therefore, a quadratic function for the derivative of the energy is reasonable.

3.1 DOMAIN THEORY

To calculate a realistic domain radius, it was necessary to incorporate domain-theory ideas into the model. In general, a domain model estimates the location of domain walls, which are assumed to be thin and featureless, but carry a surface energy density characteristic of the material. The basic domain theory of bubbles, due to Thiele [50,51], agrees well with experiment for high-Q materials (thin walls). We seek a method which will be more general, and which will use information from an existing computed wall configuration, but which need only be more accurate for small perturbations of the existing domain radius.

The relevant part of Thiele's analysis is summarized in section 1.3.1. Before we use his results in the present formulation, we note the following points.

The bubble aspect ratio in section 1.3.1 is based on the radius at a wall of negligible thickness. In a thick-walled bubble, $\theta=\pi/2$ ($m_z=0$) at the middle of the wall region, on a surface extending from one film surface to the other around the bubble. The average distance of this surface from the bubble axis we define to be the bubble radius, denoted by r_o (aspect ratio, $a_o=2r_o/T$).

The wall surface energy density in Thiele's treatment was taken to be the characteristic Bloch wall value (σ_A, section 1.2). This may be improved upon in the present model by computing energies over the grid to calculate a better value, σ_w. Care must be taken in the assignment of energies to the wall [40].

In Eq. (1.2), the term in F(a) is the derivative of the magnetostatic energy of a thin-walled bubble. We will replace this term by a Taylor series expansion about a_o, the existing aspect ratio, to make the analysis mathematically simpler, yet accurate in the prediction of small excursions from a_o.

3.1.1 Quadratic Approximation for the Derivative of Total Energy.

We will assume that, over a limited range of aspect ratio near a_o, the derivative of the total energy of the bubble can be approximated by a second-degree polynomial:

$$\frac{dE_t(a)}{da} = E_t'(a) = W_{t1}' + a\,W_{t2}' + a^2\,W_{t3}' \qquad (3.1)$$

Hereafter, E will refer to energies and W to coefficients in polynomials of a, where the primes denote that the polynomial represents a derivative with respect to aspect ratio.

The formula (3.1) would be a Taylor expansion about a_o after incorporating factors in a_o and a_o^2 into the coefficients.

If the coefficients were known, the roots of Eq. (3.1) would give the aspect ratio at which $E_t'(a)=0$. We may then choose the root at which

$$W_{t2}' + 2a\, W_{t3}' > 0 \tag{3.2}$$

as the stable minimum-energy aspect ratio. If it should be too far from a_o, we shall adjust the grid (and configuration) radius by some smaller amount, in the indicated direction. The calculation of this chapter may then be repeated.

Now, we must derive calculable expressions for the coefficients in Eq. (3.1). The coefficients are:

$$\begin{aligned} W_{t1}' &= W_1' + W_{1M}', \\ W_{t2}' &= W_2' + W_{2M}', \\ W_{t3}' &= W_{3M}' \end{aligned} \tag{3.3}$$

where subscript M refers to the magnetostatic self-demagnetizing energy, and

$$W_1' = \left[\frac{\partial}{\partial a}\left(E_{Ku} + E_x + E_{B\Delta} + E_{M\Delta}\right)\right]_{a_o} \tag{3.4}$$

$$W_2' = \left[\frac{\partial^2}{\partial a^2}\ E_{B2}\right]_{a_o} \tag{3.5}$$

where Δ denotes that the quantity is the difference between the computed energy and the energy calculated for a thin-wall bubble.

Thus, W_1' is the first derivative of the wall energy (defined according to Schlömann [40]), which is considered to have approximately a linear dependence on wall radius, as does the grid volume. Details will be found in section 3.2.

E_{B2} is approximately the magnetostatic energy of the bubble domain interior due to the bias field. It has the same dependence on aspect ratio, quadratic (hence the subscript "2"), as has the volume of the bubble interior, a solid cylinder. E_{B2} will be discussed further in section 3.2.2.

3.1.2 Taylor Series Analysis of Domain-Model Demagnetizing Energy.

A Taylor expansion for the derivative of the bubble self-demagnetizing energy may be written

$$E_M'(a) = W_{M1}' + (a-a_o) W_{M2}' + \frac{(a-a_o)^2}{2} W_{M3}', \tag{3.6}$$

$$= W_{1M}' + a W_{2M}' + a^2 W_{3M}', \tag{3.7}$$

where W_{1M}', W_{2M}', and W_{3M}' appear in Eq. (3.3), and are, from Eq. (3.6),

$$W_{1M}' = W_{M1}' - a_o W_{M2}' + \frac{a_o^2}{2} W_{M3}', \tag{3.8}$$

$$W_{2M}' = W_{M2}' - a_o W_{M3}', \tag{3.9}$$

$$W_{3M}' = \tfrac{1}{2} W_{M3}'. \tag{3.10}$$

It is important to note that these formulas refer to a thin wall domain model of the bubble.

To relate W_{M1}', W_{M2}', and W_{M3}' to the Thiele functions $F(a_o)$ and $S_o(a_o)$ of section 1.3.1, we proceed as follows. First, from Eqs. (3.6) and (1.2),

$$W_{M1}' = E_M' (a_o) \tag{3.11}$$

$$= - \frac{cT}{2} F(a_o) \tag{3.12}$$

where $c = 2\pi\mu_o M_s^2 T^2$. Next, from Eq. (3.6),

$$W'_{M2} = [\frac{d}{da} E'_M(a)]_{a_o} \quad . \tag{3.13}$$

But, from Eq. (3.11), (3.12) and (1.6),

$$\frac{d}{da_o} (E'_M(a_o)) = - \frac{cT}{2} \frac{dF}{da_o} \tag{3.14}$$

$$= - \frac{cT}{2} [F(a_o) - S_o(a_o)]/a_o . \tag{3.15}$$

For $a \cong a_o$, we let

$$[\frac{d}{da} E'_M(a)]_{a_o} \cong \frac{d}{da_o} E'_M(a_o), \tag{3.16}$$

so,

$$W'_{M2} \cong - \frac{cT}{2} [F(a_o) - S_o(a_o)]/a_o . \tag{3.17}$$

Now, we integrate Eq. (3.7) to find an expression for the magnetostatic energy of a thin-wall bubble of aspect ratio a_o:

$$E_{MTW}(a_o) = \int_o^{a_o} E'_M(a)\, da \tag{3.18}$$

$$= a_o W'_{1M} + \frac{a_o^2}{2} W'_{2M} + \frac{a_o^3}{3} W'_{3M} \tag{3.19}$$

and $E_{MTW}(0) = 0$. The coefficients in Eq. (3.19) are just those of Eq. (3.7).

Using Eqs. (3.8), (3.9), (3.10), and solving Eqs. (3.19), (3.12), and (3.17) for W'_{M3},

$$W'_{M3} = \frac{6}{a_o^3} [E_{MTW}(a_o) + \frac{a_o cT}{4} (F(a_o) + S_o(a_o))] . \tag{3.20}$$

$E_{MTW}(a_o)$ may be computed by a discrete-element method using appropriate ring demagnetizing factors (section 3.2.1). Given E_{MTW} and algorithms for computing the functions $F(a_o)$ and $S_o(a_o)$ [27], we can calculate W'_{1M}, W'_{2M}, and W'_{3M}, from Eqs. (3.8), (3.9), (3.10), (3.12), (3.17), and (3.20), for use in Eq. (3.3).

3.2 WALL-MODEL ENERGIES

The domain-model calculation of bubble radius is affected by the computed wall configuration through the quantities in Eq. (3.4). Also, the evaluation of Eq. (3.5) and of E_{MTW} in Eq. (3.20) require techniques associated with the wall model.

This section is concerned with the measurement of contributions to wall energy, and by implication, with the assignment of energy contributions to the wall or to the domain regions. We define the wall energy according to Schlömann [40]: "the sum of anisotropy and exchange energy stored in the wall plus the dipolar interaction energy associated with the actual wall minus the dipolar interaction energy associated with an infinitely sharp wall".

3.2.1 Wall Demagnetization Energy.

Having considered the variation of the demagnetization energy of a thin-walled bubble, with reference to the Thiele formulation, in section 3.1.2, we must now account for the demagnetization energy due to the existence of the magnetic configuration in the grid. That is, we add to the wall energy the difference between the computed total demagnetizing energy and the thin-wall bubble demagnetizing energy:

$$E_{M\Delta} = E_M - E_{MTW}. \qquad (3.21)$$

The total demagnetization energy of the bubble, E_M, is computed as follows. The reference state is the saturated film, with $\theta=0$, $\vec{M}=M_s\hat{z}$. We measure the magnetostatic energy in the various regions of the film, and pair terms of bubble-state energy with corresponding terms of saturation-state energy.

With reference to Fig. 3.1, we will employ the following subscripts.

d:	demagnetizing field of magnetization in the grid;
ds:	Demagnetizing field of the same region, in the saturated state;
f:	fringing, or stray, field from the domain regions outside the grid;
g:	grid region;
z:	$\hat{z}$-component of a field;
i,e:	fields from saturated domain regions interior and exterior, respectively, to the bubble;

and r_i and r_e are the radii of the radial boundaries of the grid at the interior and exterior domain regions. The z and α integrations are always from $-T/2$ to $T/2$ and from zero to 2π, respectively, and are always to be associated with dV.

For clarity, we first consider the grid and non-grid regions separately. In the grid region,

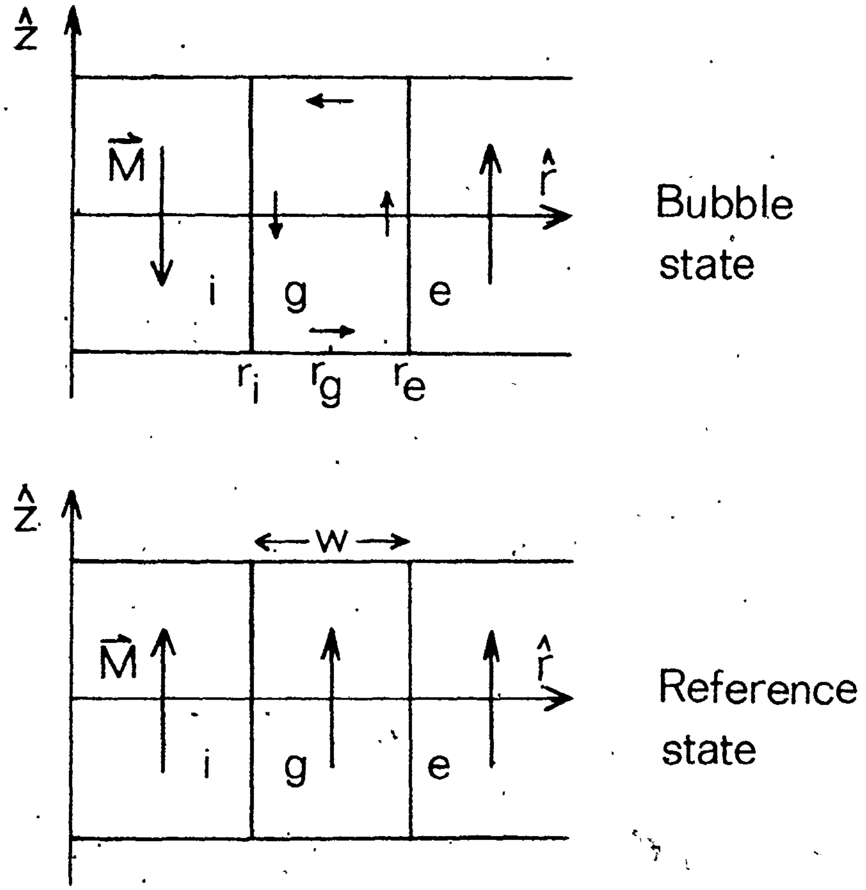

Fig. 3.1 Notation for the organization of demagnetizing energies.

$$E_{Mg} = -\tfrac{1}{2}\,\mu_o\,M_s^2 \int_g \hat{m}\cdot\vec{h}_d\,dV$$

$$-\tfrac{1}{2}\,\mu_o\,M_s^2 \int_g \hat{m}\cdot\vec{h}_f\,dV$$

$$-\tfrac{1}{2}\,\mu_o\,M_s^2\,V_g. \qquad (3.22)$$

The second term of this formula is matched (according to the principle of reciprocity), by the magnetostatic energy in the domain regions, inside and outside the bubble, due to the stray field of the magnetization in the grid region. It therefore appears also in the expression for the energy in those saturated regions, which are not covered by the grid:

$$E_{Ms} = -\tfrac{1}{2}\,\mu_o\,M_s^2 \int_g \hat{m}\cdot\vec{h}_f\,dV$$

$$-\,[-\tfrac{1}{2}\,\mu_o\,M_s^2 \int_g (h_{fiz} + h_{fez})\,dV]$$

$$-\,[-\tfrac{1}{2}\,\mu_o\,M_s^2 \int_g (\vec{h}_{ds})_z\,dV$$

$$+\tfrac{1}{2}\,\mu_o\,M_s^2 \int_g (\vec{h}_{ds})_z\,dV].$$

$$+\,\mu_o\,M_s^2 \int_o^{r_i} (\vec{h}_{fe})_z\,dV$$

$$+\,\mu_o\,M_s^2 \int_{r_e}^{\infty} (\vec{h}_{fi})_z\,dV. \qquad (3.23)$$

Here, the third and fourth terms (ignoring square parentheses) add to zero and were put in as a step in simplification of the expression. The second and third terms make up the energy of the grid region in the saturated state, just the product of the grid volume and the energy density. The fifth and sixth terms are like the terms of bias field energy in saturated regions (see section 3.2.3), and they are equal by reciprocity. After simplifying,

$$\begin{aligned} E_{Ms} = & - \tfrac{1}{2} \mu_o M_s^2 \int_g \hat{m} \cdot \vec{h}_f \, dV \\ & - \tfrac{1}{2} \mu_o M_s^2 V_g \\ & - \tfrac{1}{2} \mu_o M_s^2 \int_g (\vec{h}_{ds})_z \, dV \\ & + 2 \mu_o M_s^2 \int_o^{r_i} (\vec{h}_{fe})_z \, dV \end{aligned} \tag{3.24}$$

Now, the total demagnetization energy (referred to the state of saturation of the entire film) is

$$E_M = E_{Mg} + E_{Ms} \tag{3.25}$$

$$\begin{aligned} = & - \tfrac{1}{2} \mu_o M_s^2 \int_g \hat{m} \cdot \vec{h}_d \, dV \\ & - \mu_o M_s^2 \int_g \hat{m} \cdot \vec{h}_f \, dV \\ & - \mu_o M_s^2 V_g - \tfrac{1}{2} \mu_o M_s^2 \int_g (\vec{h}_{ds})_z \, dV \\ & + 2 \mu_o M_s^2 \int_o^{r_i} (\vec{h}_{fe})_z \, dV. \end{aligned} \tag{3.26}$$

The terms containing integrations are all computed using appropriate ring-demagnetizing factors [32].

The thin-wall bubble magnetostatic self-energy (section 3.1.2) is computed from the demagnetizing field, $\vec{h}_{fTW}$, of a ring bounded by cylinders at the mean $m_z=0$ radius, r_o, of the wall and at infinite radius. The energy is, using reciprocity,

$$E_{MTW} = - \mu_o M_s^2 \int_o^r (\vec{h}_{fTW})_z \, dV. \tag{3.27}$$

The region bounded by the film surfaces, the z-axis and r_o is divided into ring-cells and the magnetostatic energy in the cells is computed and summed.

We may now calculate $E_{M\Delta}$ from Eqs. (3.21), (3.26), and (3.27), for use in Eq. (3.4). As in the case of bias field energy, we assume that $E_{M\Delta}$ is an approximately linear function of radius, for aspect ratios near a_o.

3.2.2 Applied Bias Field Energy.

The greater part of the bias field energy is in the saturated interior of the bubble, at radii less than $r_i=r_g-w/2$, where according to Fig. 3.1, r_g is the radius of the centre of the grid and w is the grid width. With r_o the average radius where $\theta=\pi/2$, we define a quantity Δr by

$$r_g = r_o - \Delta r. \tag{3.28}$$

Then the inner domain bias energy is

$$E_{B2} = - 2 \mu_o M_s^2 h_B \pi (r_o - \Delta r - \frac{w}{2})^2 T, \tag{3.29}$$

so

$$\left(\frac{\partial^2}{\partial a^2} E_{B2}\right)_{a_o} = \frac{T^2}{4} \left(- 2 \mu_o M_s^2 h_B \pi 2 T\right) \tag{3.30}$$

that is,

$$\left(\frac{\partial^2}{\partial a^2} E_{B2}\right)_{a_o} = \frac{T^2}{4} \frac{2 E_{B2}}{r_i^2} \tag{3.31}$$

where the subscript "2" signifies a quadratic dependence on radius.

In addition, there was included in the domain analysis the energy of the saturated film between r_i and r_o. However, there was no bias field energy included in the wall energy density. Therefore, we require the difference in bias energy between the grid region with a magnetization configuration in it and a grid region with a thin wall at the radius r_o within it. The region of radius less than r_i is common to the two situations and cancels out, so

$$E_{B\Delta} = E_B - E_{BTW} \tag{3.32}$$

becomes

$$\begin{aligned} E_{B\Delta} = &- \mu_o M_s^2 \int_0^{2\pi} d\alpha' \int_{r_g - w/2}^{r_g + w/2} dr' \int_{-T/2}^{T/2} dz' \, m_z h_B r' \\ &- [-\mu_o M_s^2 h_B (\cos 0) \, 2\pi (r_o - \Delta r) \, w \, T] \\ &- [-2 \mu_o M_s^2 h_B 2\pi T (r_o - \tfrac{1}{2}(\Delta r + \tfrac{w}{2}))(\Delta r + \tfrac{w}{2})], \end{aligned} \tag{3.33}$$

where the first term is computed, over the grid of columns and rows, numbered (from zero) j and k, of dimensions d_r and d_z (Fig. 2.2), as

$$- \mu_o M_s^2 \int_o^{2\pi} d\alpha' \int_{r_g-w/2}^{r_g+w/2} dr' \int_{-T/2}^{T/2} dz' \; m_z \; h_B \; r'$$

$$= - \mu_o M_s^2 h_B d_r d_z 2\pi$$

$$\cdot \sum_{j,k} (m_z)_{jk} (r_o-(\Delta r + \frac{w}{2}) + \frac{d_r}{2} + jd_r. \qquad (3.34)$$

To obtain the derivative of Eq. (3.33) with respect to r_o ($= a_oT/2$), we divide each term by its factor that contains r_o. In the actual implementation, the derivative was calculated by dividing the energy $E_{B\Delta}$ by r_o itself, as was done with $E_{M\Delta}$, on the grounds that these are wall energies and the wall surface area is proportional to r_o. The reason this approximation was made for $E_{B\Delta}$ was to allow an iterative search for an improved radius without recomputing (3.34). The consequent errors in (3.34) approximately cancel out. Since Δr is small - it may be of either sign - the principal error arising in Eq. (3.33) is then proportional to w/4r, and occurs in the third term.

3.2.3 Exchange and Anisotropy Energies.

The magnetization direction is constant outside the grid, so the exchange energy is at its reference-state level there. The exchange energy within the grid is

$$E_x = \mu_o M_s^2 \int_o^{2\pi} r' \, d\alpha' \int_o^{\infty} dr' \int_{-T/2}^{T/2} dz' \; \vec{h}_x \cdot \hat{m}. \qquad (3.35)$$

To compute E_x numerically, we sum over the grid:

$$E_x = \mu_o M_s^2 \cdot 2\pi \, d_r \, d_z \sum_{j,k} (\vec{h}_x \cdot \hat{m})_{jk} \, r_j \,, \qquad (3.36)$$

where

$$r_j = r_o - \Delta r - \frac{w}{2} + \frac{d_r}{2} + j \, d_r \,, \qquad (3.37)$$

and notation is given in Fig. 2.2 and section 3.2.2; columns are numbered (from zero) by j, rows by k.

We neglect the small r_j - dependence of $\vec{h}_x$ itself (Eq. (2.23)), and consider

$$E'_x = \frac{\partial E_x}{\partial a} = \mu_o M_s^2 \pi T d_r d_z \sum_{j,k} (\vec{h}_x \cdot \hat{m})_{jk} \tag{3.38}$$

This does not include the cylindrical symmetry contribution to energy density (Eq. (A.6) whereby the anisotropy constant is effectively altered by a small amount (Eq. (2.24)). We neglect the effect of this small, high-order, r_j-dependent correction in calculating the derivative of the anisotropy energy. The energy is

$$E_{Kur} = \int_o^\infty dr' \int_{-T/2}^{T/2} dz' \int_o^{2\pi} r' d\alpha' K_{ur} \sin^2\theta \tag{3.39}$$

$$= 2\pi d_r d_z \sum_{j,k} (K_{ur} \sin^2\theta)_{jk} r_j \tag{3.40}$$

The derivative of this energy is then

$$\frac{\partial E_{Kur}}{\partial a} = E'_{Kur} = \pi d_r d_z T \sum_{j,k} (K_{ur} \sin^2\theta)_{jk}. \tag{3.41}$$

3.3 DETERMINATION OF APPROPRIATE APPLIED BIAS FIELD

During the iterations described in Ch. 2, the wall configuration changes and the energy density in the wall decreases. The effect of this on the range of bubble stability can be seen from Eq. (1.4) and Fig. 1.4. The situation will be explained with reference to the Thiele theory [51], which treats the whole range of stability, as well as to the present domain analysis, which focusses on a local range of aspect ratio.

As shown in Fig. 1.4, the stability limits are set, within the approximations of the Thiele theory, by the normalized material length, λ/T. The material length is proportional to wall energy density (section 1.2), so we will be concerned with the apparent normalized material length, λ^*/T, obtained from the computational measurement of the actual wall energy. We will consider λ^*/T to be the level of the true horizontal line in Fig. 1.4.

At a given bias field, with decreasing λ^*/T, the stable aspect ratio, a_o, increases while the collapse and runout aspect ratios, a_c and a_r, both decrease. At lower λ^*/T, therefore, the bias field must be increased to shrink the bubble to within the (shifted) range of stability.

In the course of a typical computation, this effect was manifested by the apparent drifting of the stability range away from the neighborhood of the aspect ratio of the modelled bubble. That is, when the computed wall energy density (section 3.2) was substituted directly into the Thiele formulae [27], the predicted boundaries of the stability range in terms of applied field and aspect ratio drifted higher and lower respectively, as successive wall-relaxation iterations lowered that wall energy density. See also section 7.3.2.

Another related effect, discussed in section 6.5, is the fact that wall energy density decreases with increasing aspect ratio [4]. This means that the apparent stability margins for a bubble well within the range of stability are broader than the margins as measured at bubbles very close to collapse and runout.

Thus, we cannot expect that the algorithm will converge to a "true" bubble solution if the bias field is outside the apparent range of bubble stability. Therefore, when it is found ~~that the~~ existing bias field is outside the stability range, it is changed to lie within that range.

This method can be used not only to keep the bias field within the range of stability, but within a selected smaller interval within that range. It was so used, in order to obtain a set of modelled bubbles for each material, so that the dependence of bubble parameters on aspect ratio could be studied (Chapter 6). Numerical measurements on such a set of modelled bubbles were also used to calculate true limits of stability for each film (section 7.2).

3.4 ADJUSTMENT OF DOMAIN RADIUS

After the initialization of the wall configuration (section 2.4), and after each set of iterations of the wall configuration relaxation (section 4.1), the domain radius was checked. (The wall relaxation was stopped after a chosen number of iterations, or earlier if it was found not be be converging (Ch. 4).) The domain radius adjustment entailed the following:

1. The exchange field, demagnetizing fields, and bias field were calculated and added for each cell of the grid (section 2.2).
2. The various energies were computed (sections 3.1 and 3.2), and the minimum-energy domain radius was estimated (section 3.1.1).
3. The grid radius, r_g, from which the column radii, r_j, are calculated, was reset so as to make $r_o = r_g + \Delta r$ (section 3.2.2), the measured average radius at $\theta = \pi/2$, equal to the calculated new domain radius. That is, the grid and the configuration contained in it were translated together to a new interval of radii.
4. New demagnetizing factors had to be calculated (section 2.2.3); the algorithm then returned to the wall relaxation iterations.

Thus, there were two nested loops in the overall algorithm. The inner one relaxed the wall configuration toward a minimum energy (Ch. 4), while the outer one periodically sought a minimum-energy radius for the wall configuration as a whole.

The process was considered to terminate when both iterations were calling for negligible changes in their respective aspects of bubble structure, or when the wall radius was drifting in one direction within the grid during the relaxation loop (Ch. 3 introduction), while the domain model calculated a minimum-energy radius in the opposite direction.

The latter situation, which sometimes occurred near the final solution for unusual film parameters, was considered to be evidence of the limitation of the domain model. The algorithm handled the situation by making small (2% or less) translations in the grid radius, in the direction of wall configuration drift. This final step resulted in convergence of the wall relaxation in all cases studied except the very thin-walled and very small bubbles near collapse in the $\lambda/T=0.5775$, $Q=4.6$ film.

CHAPTER 4

NUMERICAL METHODS

In the discretized-grid model of the wall, we must minimize the bubble energy with respect to the magnetization in each grid cell and determine when all cell magnetizations are adequately close to their ultimate minimum-energy orientations. If necessary, we must try to improve the algorithm's progress toward the minimum-energy state. The numerical methods chosen to treat these problems are the subjects of this chapter.

4.1 CELL ENERGY MINIMIZATION

At each grid cell i, the total effective field $\vec{h}_i$ was found by adding together the demagnetizing field, the domains' stray field, the exchange field, and the bias field, each properly weighted as described in section 2.2.5:

$$\vec{h}_i = \vec{h}_d + \vec{h}_f + \vec{h}_x + \vec{h}_B. \tag{4.1}$$

The azimuthal angle of $\hat{m}_i$ is simply set to that of $\vec{h}_i$, but the polar angle, θ_i, must be found by finding the nearest minimum of the remaining energy,

$$dE_i = [K_{ur} \sin^2 \theta_i - \mu_o M_s^2 h_i |\hat{m}_i| \cos (\theta_i - \theta_{hi})] \, dV_i. \tag{4.2}$$

This is equivalent to finding the zero of the derivative with respect to θ_i,

$$0 = K_{ur} \sin 2\theta_i + \mu_o M_s^2 h_i \sin(\theta_i - \theta_{hi}). \tag{4.3}$$

In the present work, the modified false position (regula falsi) method [26] was used to locate the zero, starting with an interval bounded by θ_{hi} and the uniaxial anisotropy easy direction (up or down) nearest in orientation to $\vec{h}_i$. This method quickly narrows the interval which contains the zero, and was terminated when the interval became less than 10^{-6} radian. The method was chosen because it is not susceptible to instability, to lack of convergence or to seeking a zero outside the initial interval; it was fast enough that a negligible fraction of the total computing time was spent here.

4.2 SCAN OF THE GRID

After the new ϕ_i and θ_i were determined, $\hat{m}_i$ was immediately reoriented before repeating the procedure, including the calculation of the effective fields, at the next cell. In this way, new information is included in the configuration as soon as possible. Furthermore, this method constitutes a one-at-a-time search [3] (section 4.4) for a minimum-energy configuration.

The scan of the grid cells is ordered so that each column is scanned from the film surface down to the film midplane, and columns are selected alternately from each side successively toward the middle of the grid. This ordering was chosen because the exchange interaction tends to align the magnetizations of neighboring cells, so changes in orientation are passed more easily from one cell to the next in the direction of the scan. Since the surface of the film has a strong influence on the wall configuration, it was desirable to convey its effect throughout the grid as quickly as possible. In fact, wavelike disturbances may propagate through the array of grid cell magnetizations, and must be allowed to damp out.

The wall configuration was expected to broaden from its initial form [21], due to stray fields from the domain regions. To avoid the possibility of excessive broadening propagating out from the grid centre, the scan inward from the sides was chosen. Any broadening that is seen is, therefore, legitimate. The definition of wall width is discussed in section 5.4.3, and broadening is further discussed in section 6.2.

Another consideration in the ordering of the columns was the possibility that a consistent scan from one side to the other could shift the wall centre with respect to the grid by a similar process. This effect would have been slight, but in any case was removed, so any radial drift (section 3.4) could be considered physically significant.

4.3 DETERMINATION OF CONVERGENCE

When, in the n^{th} iteration, the new orientation $\hat{m}_i^n$ of the magnetization of the i^{th} cell was determined (section 4.1), the size of the vectorial change, $\hat{m}_i^n - \hat{m}_i^{n-1}$, was quantified by its first norm [23],

$$(\Delta\hat{m})_i^n = |\hat{m}_i^n - \hat{m}_i^{n-1}|^1 \qquad (4.4)$$

which is just the sum of the absolute values of the components:

$$(\Delta\hat{m})_i^n = (|m_r^n - m_r^{n-1}| + |m_\alpha^n - m_\alpha^n|$$

$$+ |m_z^n - m_z^{n-1}|)_i \qquad (4.5)$$

To detect convergence of the algorithm, the maximum such value found among all the cells, $(\Delta\hat{m})^n_{max}$, was compared to a fixed criterion. For this work, a criterion of 0.37 x 10^{-3} was chosen as follows.

Relaxation factors other than unity had been tried ($\hat{m}_i$ could be moved past the minimum-energy orientation, in anticipation of later reorientations in the same direction), but their performance was unpredictable and dependent on the particular film parameters, and they made the algorithm's behavior confusing. However, a relaxation factor of 1.35 gave promising results for several sets of material parameters. During these runs, $(\Delta\hat{m})^n_{max}$ was observed to decrease for a number of iterations, level off, then decrease again in a repeating pattern. A value of $(\Delta\hat{m})^n_{max}$ = 0.5 x 10^{-3} happened to occur after a "plateau", and since it was a relatively small value and later values could be expected to be much smaller, it was chosen as the termination criterion. When a relaxation factor of unity was chosen, the termination criterion was reduced by the same amount, for consistent comparison with earlier results.

The choice of termination criteria is typically controversial. Certainly, the fact that the maximum change from one iteration to the next is very small is no guarantee that the true solution ~~is not still far~~ from the existing configuration, because there could be many more iterations required before the solution is reached. When mathematically possible in such numerical searches, it is preferable to adopt a method in which the target solution is known to be contained within a shrinking interval. A simple example is the regula falsi method of section 4.1.

In the present case, this is not possible, so we do what is common in finite-difference methods. We assume that if the changes are very small, then they will not increase in later iterations and further effort will not alter the configuration significantly. Given the very small convergence criterion that was used in this work, $(\Delta m)^n_{max} < 0.37 \times 10^{-3}$, the expense in computation time required to further improve the accuracy of the solution was not worth the expected amount of the improvement.

Since we assume that there exists a stable configuration, of some finite energy, which the algorithm could eventually reach, and that the energy will not undergo sharp fluctuations as the algorithm proceeds, we feel justified in also assuming that $(\Delta\hat{m})_{max}$ will decrease when close to the minimum-energy configuration. In fact, experience with the algorithm leads to the assumption, used in the convergence acceleration method of section 4.4, that after the first twenty or so iterations, when $(\Delta\hat{m})_{max}$ is moderately small, $(\Delta\hat{m})_{max}$ will continually decrease as the minimum-energy configuration is approached.

4.4 ACCELERATION OF CONVERGENCE

In experimental runs, the wall-relaxation algorithm took many hundreds of iterations before convergence was reached. To reduce this computation time, a conceptually simple method was implemented whereby the neighborhood of the ultimate solution would be reached without performing many of the iterations along the way.

An iteration of the wall-relaxation algorithm involves the adjustment of each angular co-ordinate of each cell magnetization to produce the state whose current total energy is a minimum with respect to each. Thus, it is like a one-at-a-time direct search [3,14], through a space of 30 x 20 x 2 = 1200 dimensions, for the location, in this configuration space, of the point of minimum energy. Total energy is a function of position in configuration space.

When $(\Delta\hat{m})_{max}$ was small, while still substantially greater than the convergence criterion, each iteration evidently was moving the search only a short distance through configuration space. It was observed over many iterations that wall structural features and individual $\hat{m}_i$ orientations were changing progressively, not oscillating. This suggested that the search was moving slowly in a fairly consistent direction. The relaxation of the wall configuration was a naturally gradual process.

An obvious strategy was to linearly extrapolate from two successive configurations to a new location in configuration space. This would save the time of an entire iteration, and probably move the search to nearly the same position. It is called a pattern move [3,14], the pattern having been established by the iteration moves.

The idea is schematically illustrated, for a scalar function represented by contour levels in a two-dimensional space, in Fig. 4.1. The one-at-a-time search will be slow if the energy surface in configuration space is an elliptical valley oriented between all the co-ordinate axes, and even slower if it is a narrow, curving valley.

After a pattern move, another iteration is performed. If $(\Delta\hat{m})_{max}$ is less than for the previous iteration, we conclude we are closer to the target minimum energy, just as when doing only iterations (section 4.3). Then another pattern move can be made along the line from the configuration after the last iteration through the new configuration. The iteration serves not only to monitor $(\Delta\hat{m})_{max}$ and advance the algorithm, but also to correct the direction of pattern moves.

If the sequence of iterations and pattern moves is repeated, the pattern moves increase steadily and eventually get much greater than a typical iteration move. When, inevitably, a $(\Delta\hat{m})_{max}$ is larger than the previous one, we fear the pattern move has gone past the target solution to a point in configuration space that is further from the solution than the previous point. We might also suspect that the new point is simply up on the side of the narrow, curving valley in the energy surface in configuration space, where the steeper slope of the surface represents a

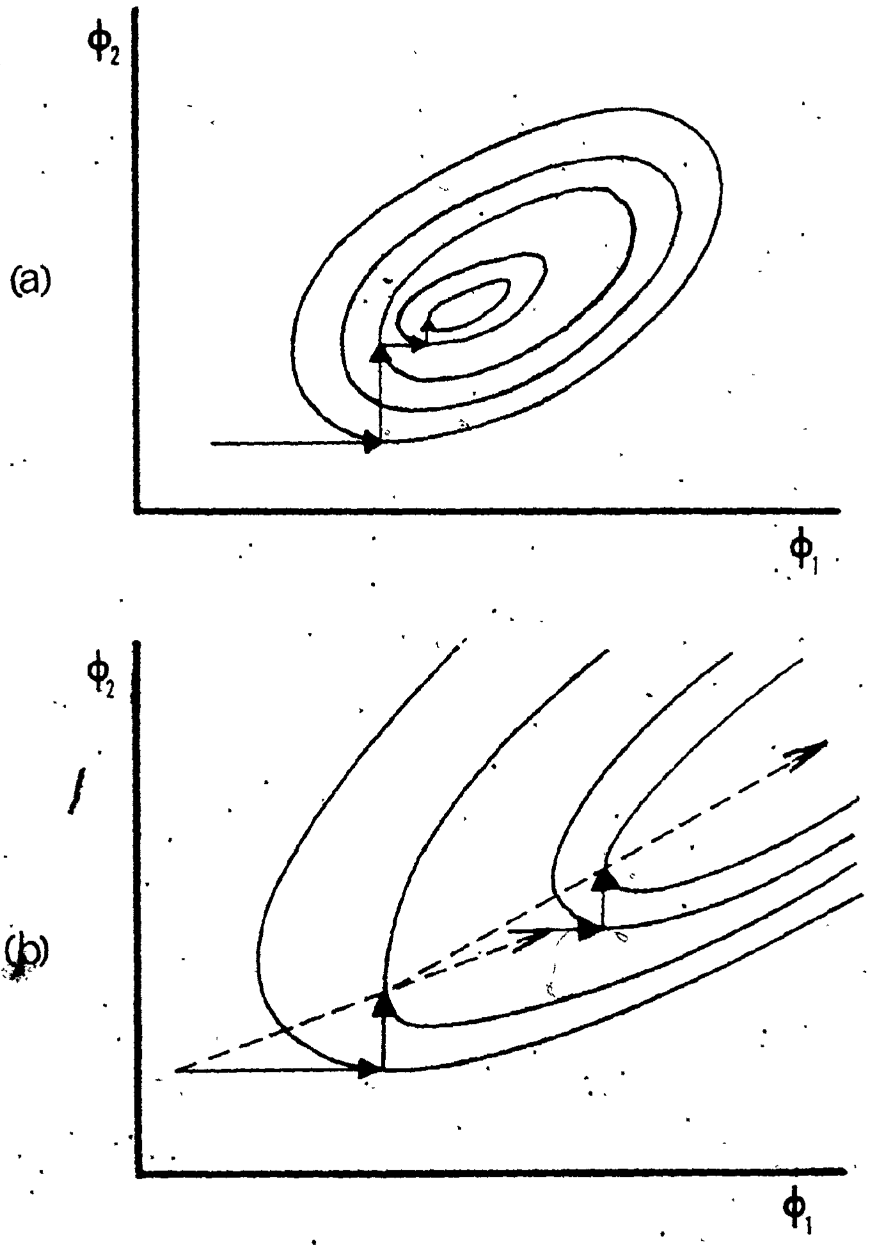

Fig. 4.1 Searches for the minimum-energy point in a (schematically, two-dimensional) space of wall configurations: (a) one-at-a-time, (b) pattern moves.

stronger generalized force on the configuration, making it move faster, as indicated by the larger $(\Delta\hat{m})_{max}$. But we have no way of knowing, so to be conservative and insure that the pattern moves never hinder the solution process, in this case we discard the pattern move and the subsequent iteration move, returning to the configuration prior to the "bad" pattern move.

Thus, the assumption that $(\Delta\hat{m})_{max}$ decreases with decreasing distance to the minimum-energy configuration may slow the search for that configuration by pattern moves. However, it does not deter the iteration moves from pressing the search as best they can.

CHAPTER 5

GENERAL STRUCTURE OF WALL CONFIGURATIONS

A numerical configuration of a bubble is the result of applying the algorithms of Chapters 2, 3, and 4 to a set of starting parameters describing the film and bias field. This configuration has a wall of unique three-dimensional structure at a characteristic radius from the bubble axis.

The purpose of this chapter is to present wall configurations and to describe their overall structural features qualitatively. The different representations emphasize different features. As well as being an introduction to the more quantitative analysis of the next chapter, this general discussion can itself provide a special understanding of domain wall structure.

Because of the symmetry about the film midplane, only the upper halves of walls are shown in these pictures. Due to the cylindrical symmetry, of course, the structure of a cross-section of the wall fully characterizes the three-dimensional wall structures, if the cylindrical nature of the wall region is kept in mind.

5.1 DISPLAY OF MAGNETIZATION VECTORS BY ARROWS

In Figs. 5.1 and 5.2, each arrow is the projection of a

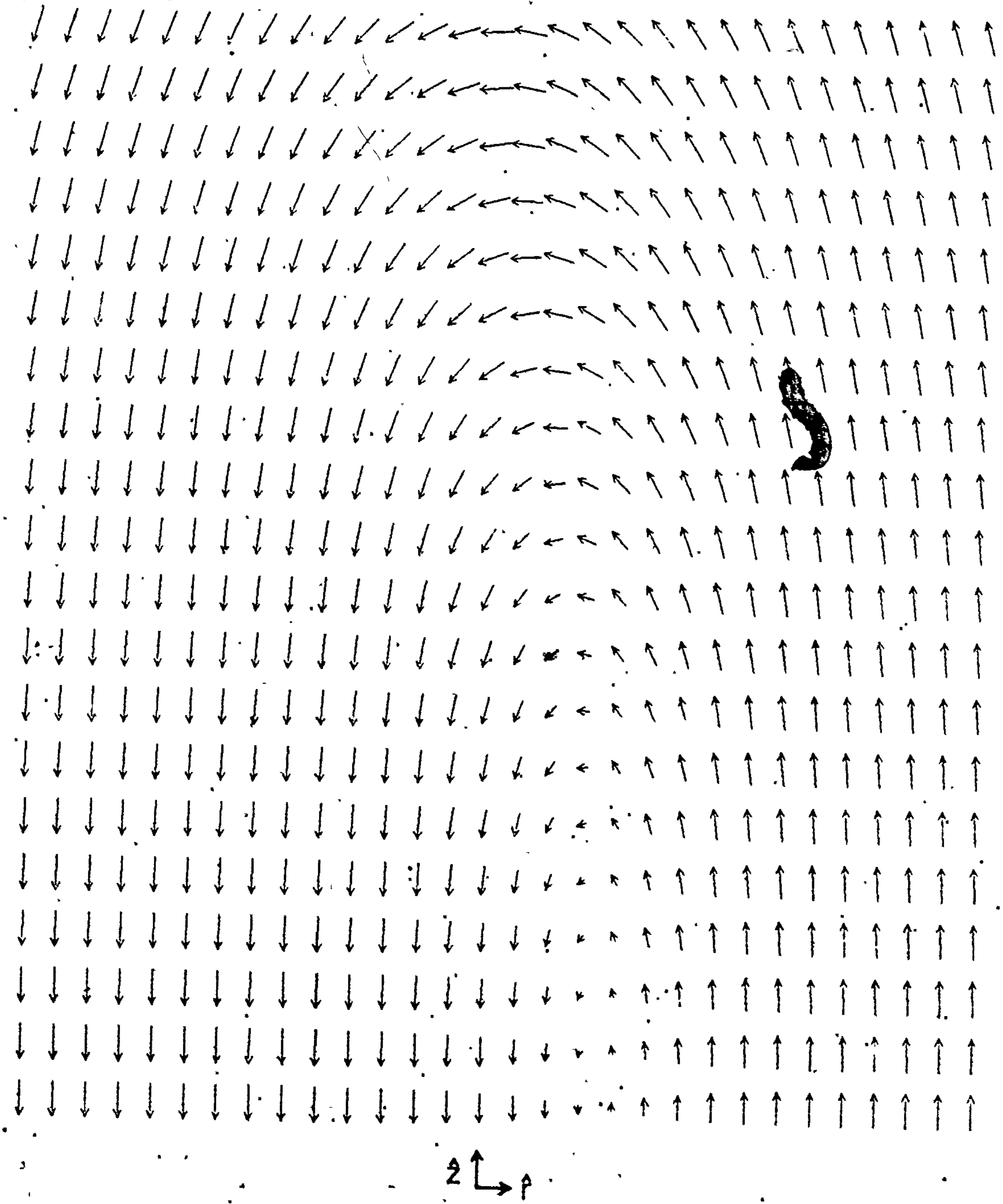

Fig. 5.1 Projections of $\hat{m}$ on $\hat{\rho}$ - $\hat{z}$ plane. Q=2.3, λ/T=.1155.

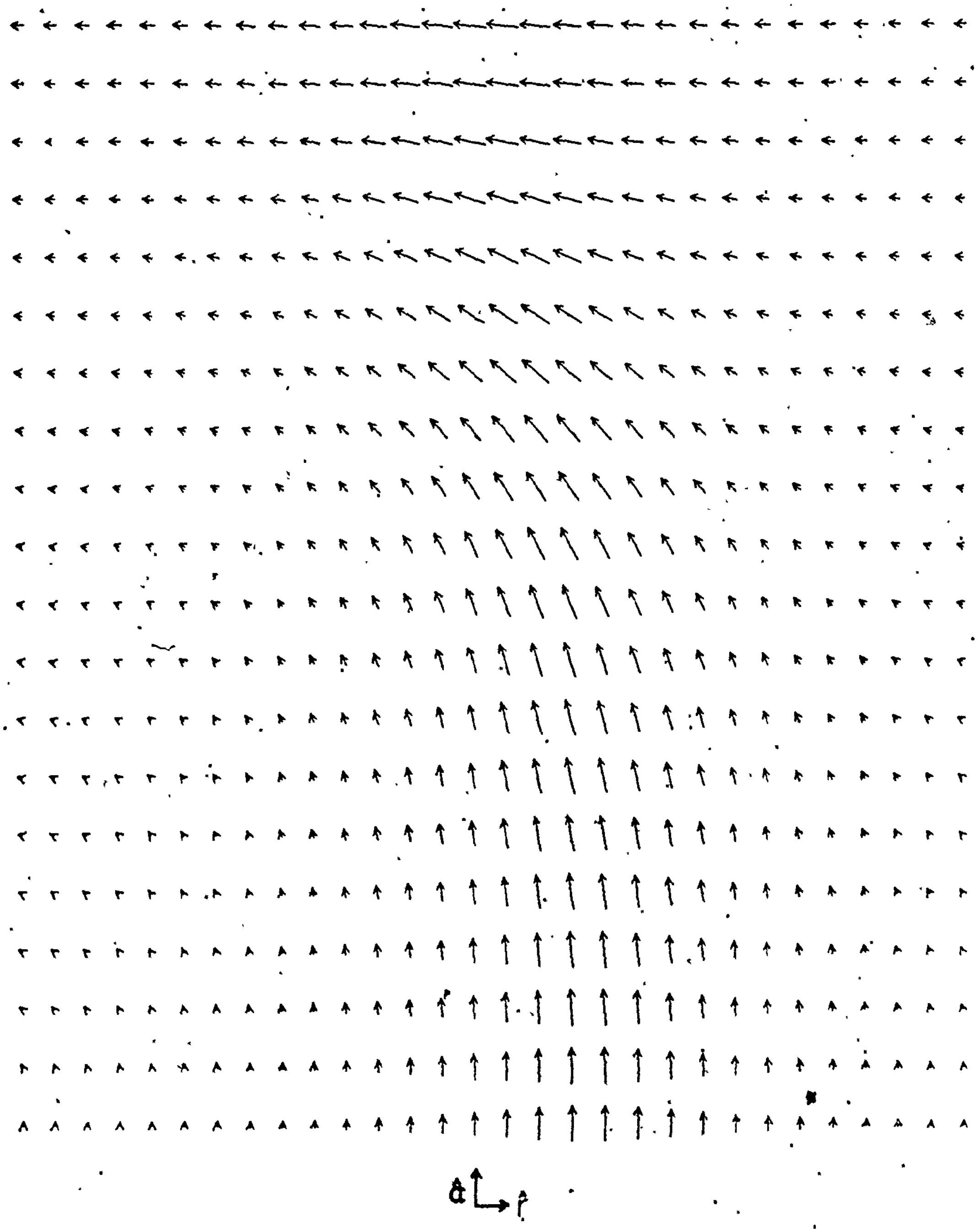

Fig. 5.2 Projections of $\hat{m}$ on $\hat{r}$ - α plane. Same bubble as in Fig. 5.1.

magnetization unit vector, $\hat{m}_i$, on the $\hat{r}$-$\hat{z}$ and $\hat{r}$-$\hat{\alpha}$ planes, respectively. The $\hat{m}_i$ were scaled to the separation of arrow centres in the figure; the height and width of the arrays of arrows were not scaled to the height and width of the grid. The bubble was moderately close to runout in a film of Q=2.3, λ/T=.1155 (see Table 6.1).

In Fig. 5.1 of the $\hat{r}$-$\hat{z}$ projections, the arrows are almost straight up at the right side, on the outer edge of the grid, and almost straight down at the left, on the inner boundary. The $\hat{r}$-$\hat{\alpha}$ projections of Fig. 5.2 almost vanish at the sides, of course, because $\hat{m} \cong \pm\, \hat{z}$ is nearly perpendicular to that plane. At the bottom centre of the $\hat{r}$-$\hat{\alpha}$ figure, $\hat{m} = \hat{\alpha}$ ($\theta=\pi/2$, $\phi=\pi/2$), while $m_r = m_z = 0$ in the $\hat{r}$-$\hat{z}$ view.

The centre of the wall is defined as the surface on which $m_z=0$ ($\theta=\pi/2$). Near the film surface, from the two figures it is clear that $\hat{m} \cong -\bar{r}$. The twist of $\hat{m}$ from $\hat{\alpha}$ at the film midplane toward $-\hat{r}$ at the film surface is especially clear in the $\hat{r}$-$\hat{\alpha}$ figure.

That θ is a function of z is clear from looking down a column of Fig. 5.1. The variation of ϕ with r is not so clear from Fig. 5.2, however; it will be seen explicitly in Fig. 5.3 below.

The overall appearance of the map of $\hat{r}$-$\hat{z}$ projections in Fig. 5.1 does suggest, in LaBonte's phrase [34], "a vortex pattern with a great deal of flux closure within the film".

5.2 RADIAL PROFILES OF ORIENTATION ANGLES

The members of the family of curves in Fig. 5.3 are plots of the azimuthal angle ϕ along every second row of grid cells, including the row at the film midplane and the one at the surface. The bubble is that of section 5.1, as it is for Fig. 5.4 below.

The lowest line is straight, at $\phi = \pi/2$, because symmetry about the film midplane so constrains the azimuthal angle. This means that for the film midplane row of the grid, the wall has the form of a pure Bloch wall.

The difference between the lowest two lines far from the centre of the grid is inconsequential, because $\hat{m} \sim \pm \hat{z}$ there, so the azimuthal angle is ill-defined.

Although $\frac{\partial \phi}{\partial r}$ is zero near the wall centre, nearby on either side there is substantial r-dependence of ϕ. This demonstrates the inaccuracy of the common assumption that $\phi = \phi(z)$. The azimuthal twist increases with proximity to the domain regions whose stray fields cause it [46].

Figure 5.4 contains similar plots of the polar angle, θ, in four equally-spaced rows, again including the film midplane and surface rows. Note that the ordinate is here inverted.

The surface row profile has the least slope, demonstrating wall width flaring at the surface. Moving toward the film midplane, the midpoints of the curves occur at larger radii; this is the phenomenon of wall radius bulging [51].

The profile of the film midplane row is that of a pure

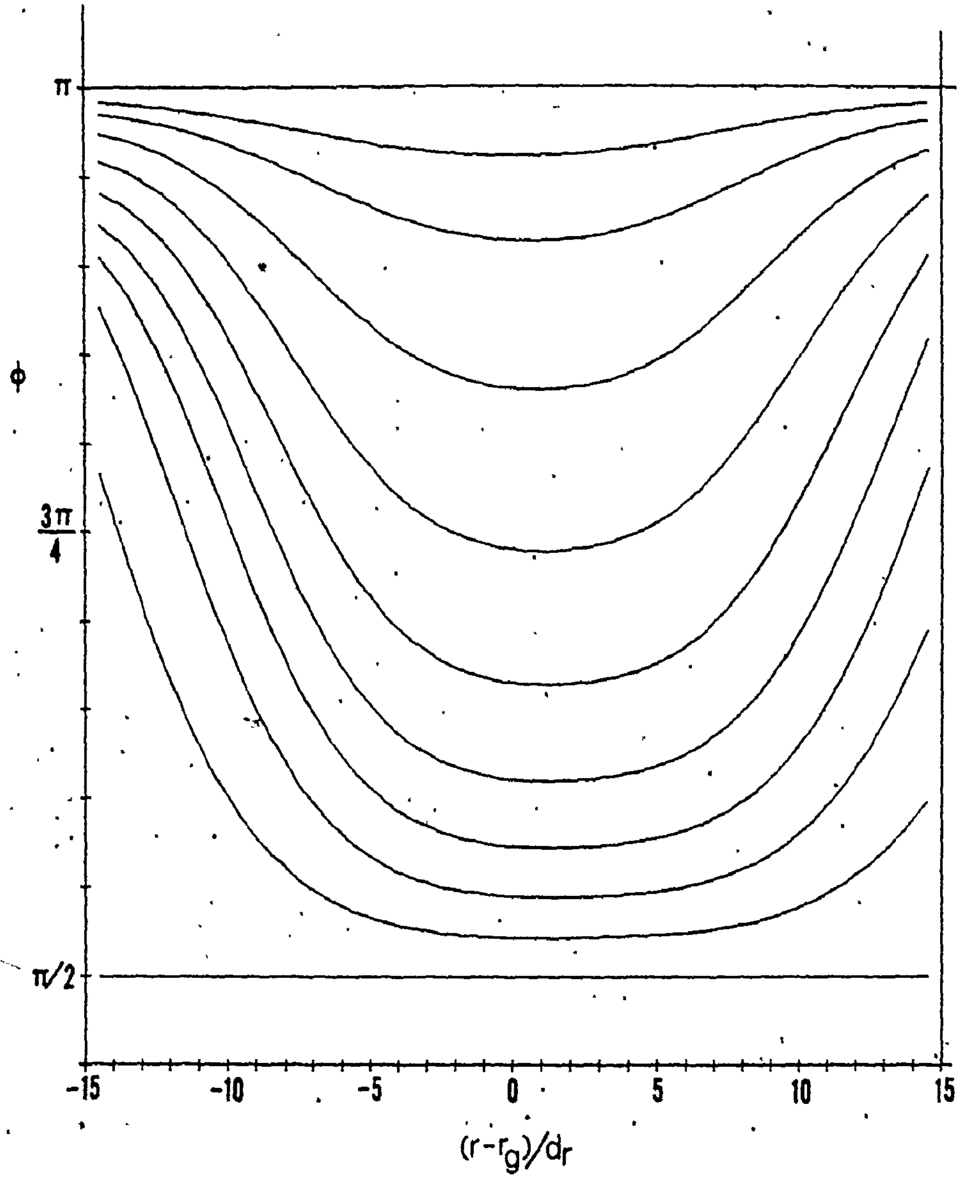

Fig. 5.3 Azimuthal angle ϕ as a function of radius, from the film surface. Same bubble as in Fig. 5.1.

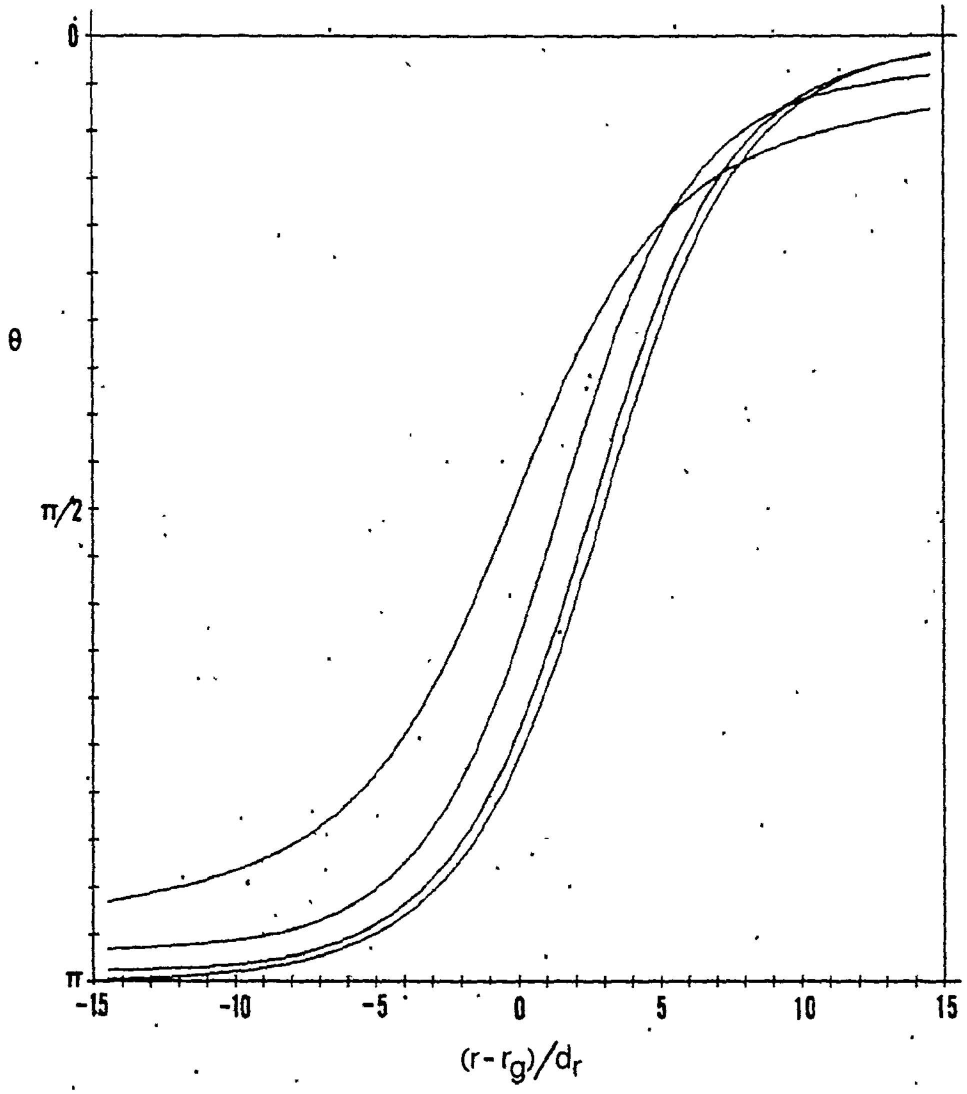

Fig. 5.4 Polar angle θ as a function of radius, from the film midplane to near the film surface. Same bubble as in Fig. 5.1.

Bloch wall (Eq. (1.9)), such as would be found in bulk material, far from surfaces. The next profile to it has similar slope, indicating that wall width flaring is very much localized near the surface in this film.

As seen from the top profile in Fig. 5.3, the top row contains an almost pure Néel wall, in which $\hat{m}$ would remain in the plane perpendicular to the wall. Conventionally, Néel walls occur between domains in which the magnetization is in the film plane, as it is in such Néel walls as well. The existence of the surface stray fields does not permit a direct comparison between our top-row profile and a conventional Néel profile [33], but our next profile lower in the figure is interesting in this respect. It is associated with values of ϕ intermediate between $\pi/2$ (Bloch wall) and π (Néel wall), and runs virtually parallel to the two lower-z curves, except near the domains on either side, where it levels off more. This behaviour may be attributable either to characteristic Néel-wall tails [33] due to the wall's own local demagnetizing field, to a local wall broadening due to the proximity of both domains and the film surface to the upper corners of the grid region, to a combination of these two effects, or to some other interaction with the ϕ profile in Fig. 5.3. These possibilities might provide interesting subjects for further investigation.

5.3 CONTOUR MAPS OF ORIENTATION ANGLES

Figure 5.5 contains [illegible] maps of [illegible] θ (ro[illegible]

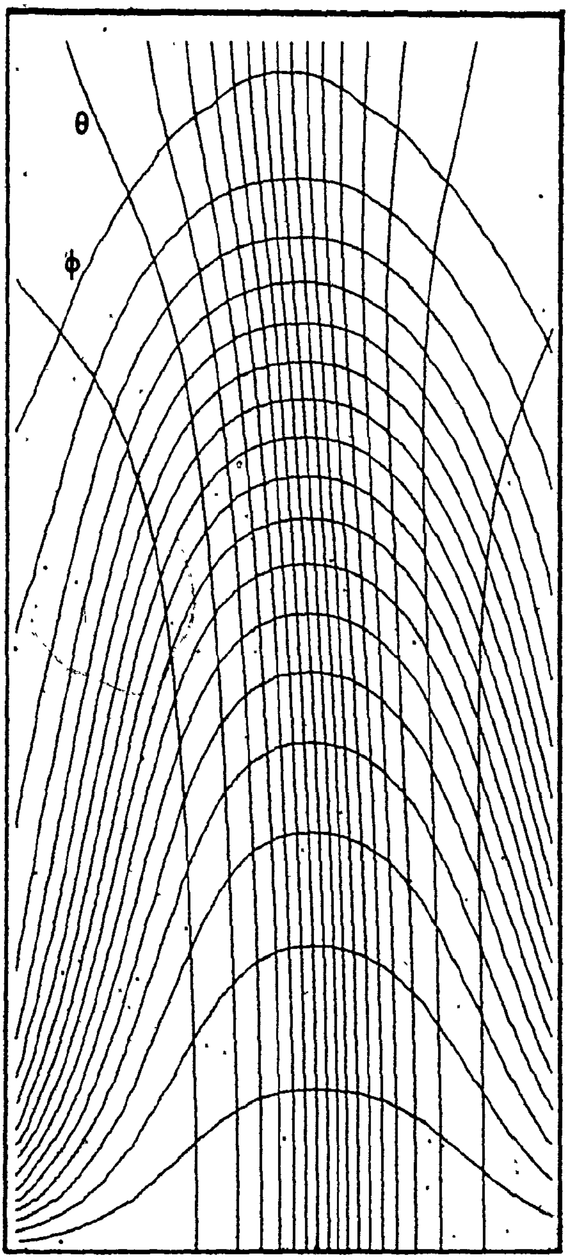

Fig. 5.5 Contour plots of polar and azimuthal angles θ and φ for Q=2.3, λ/T=.1155.

vertical) and ϕ (horizontal near the middle) for the wall of the bubble of section 5.1. The shapes of this and following maps are in scale to the shapes of the corresponding grids.

The contour lines trace constant values of the respective angles. They are perpendicular to the gradients of the angles, and their local densities are an indication of the magnitudes of those gradients. The θ contour levels were chosen to be at equal increments in the open interval from zero to π, the ϕ contours at equal increments in the open interval from $\pi/2$ to π.

The θ contours clearly show the wall radius bulging and width flaring, and the localization of the latter near the film surface. Also, the θ contours tend to become perpendicular to the surface, as expected from the surface boundary condition, Eq. (2.34).

Figure 5.6 shows the contour maps for a different bubble, one near the middle of the stability range in a film having Q = 2.3 (as in Fig. 5.5) and $\lambda/T = 0.231$ (0.1155 for Fig. 5.5). This figure shows the considerable wall width a bubble can have - it depends, classically, on λ/QT.

These contours show more clearly the influence of the surface boundary condition on both θ and ϕ. In comparison with Fig. 5.5, the θ gradients are, of course, much less; the ϕ twist is more uniform through the film thickness and reaches a smaller value at the surface.

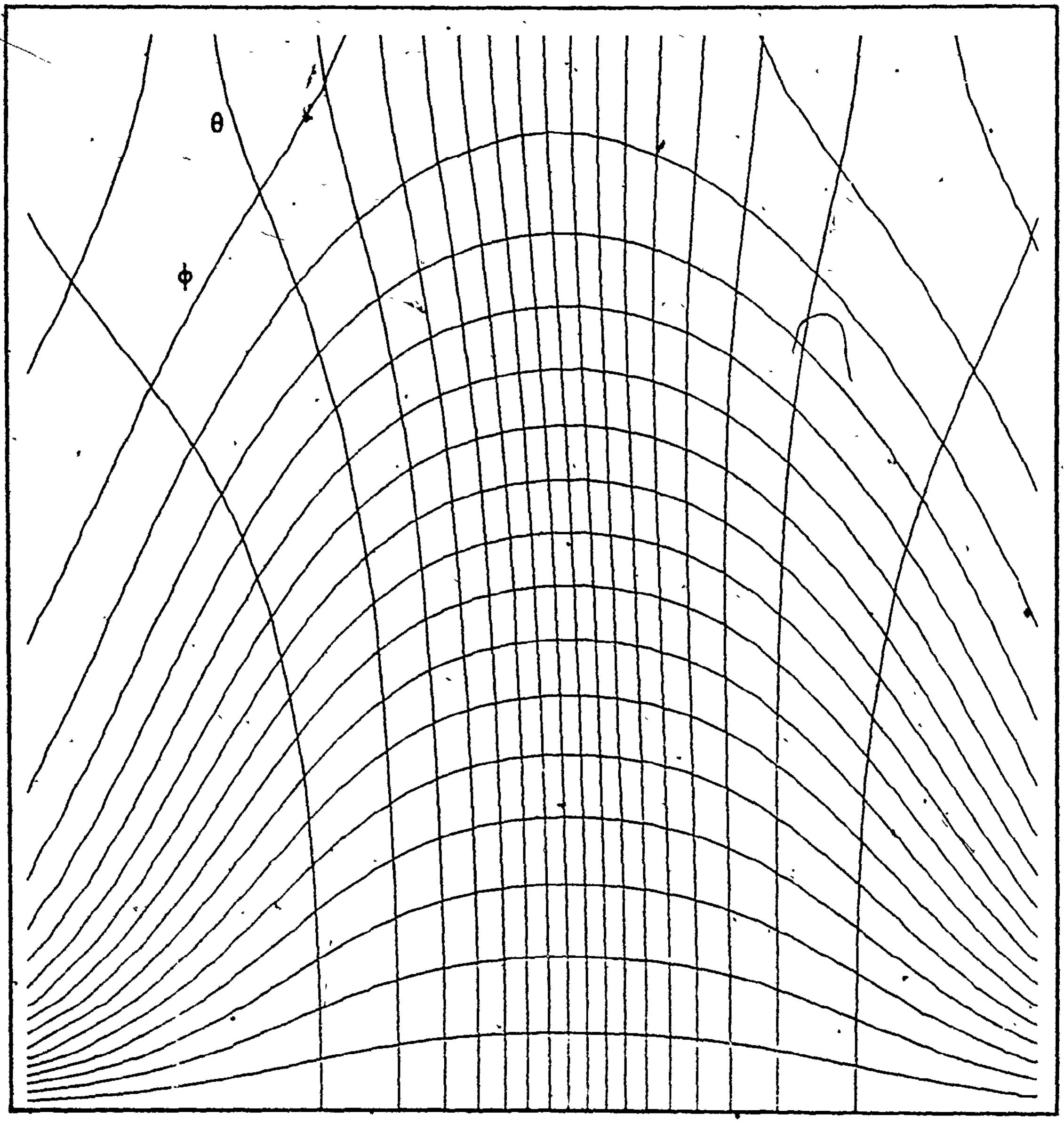

Fig. 5.6 Contour plots of θ and φ for Q=2.3, λ/T=.231.

5.4 WALL STRUCTURE PARAMETERS AS FUNCTIONS OF z

5.4.1 Azimuthal Angle Twist, $\phi(z)$.

The azimuthal angle contours of Fig. 5.5 indicate that along the wall centre, $\frac{\partial\phi}{\partial z}$ is smaller near the film midplane and near its surface than between those areas. The $\phi(z)$ profile is shown explicitly in Fig. 5.7, where it was plotted for bubbles in films of $\lambda/T = 0.231$, $Q = 1.15$, 2.3, and 4.6 (see Table 6.1). The values of $\phi(z)$ were those occurring at $\theta = \pi/2$ in each row (see section 5.4.2); the values extrapolated at the surface (according to the cubic polynomial that led to Eq. (2.38)) were added.

For these films, wall thickness decreases with increasing Q (see Table 6.2). As was found by others, the thinner the wall, the greater is the maximum twist [39,21] and the more it is localized near the surface [21]. In the present work, since the anisotropy constant K_u is fixed (see Table 6.1), the localization is related to the material's characteristic "Bloch line width",

$$l_{BL} = (2A/\mu_o M_s^2)^{\frac{1}{2}} , \qquad (5.1)$$

which quantifies the relative strengths of the exchange and demagnetizing fields. Smaller Bloch line width (in this case, higher Q; see Table 6.2) corresponds to larger allowed $\frac{\partial^2\phi}{\partial z^2}$ (weaker exchange field constant A, Eq. (2.20)) and more "structure" in the $\phi(z)$ profile, as is visible in Fig. 5.7.

DeBonte's [21] Ritz-method solutions for stripe domains (no bias field) represented sin $\phi(z)$ by a Jacobian elliptic function, cn, of complete elliptic integrals of the first kind, but the present bubble model has found [4] that this function gives

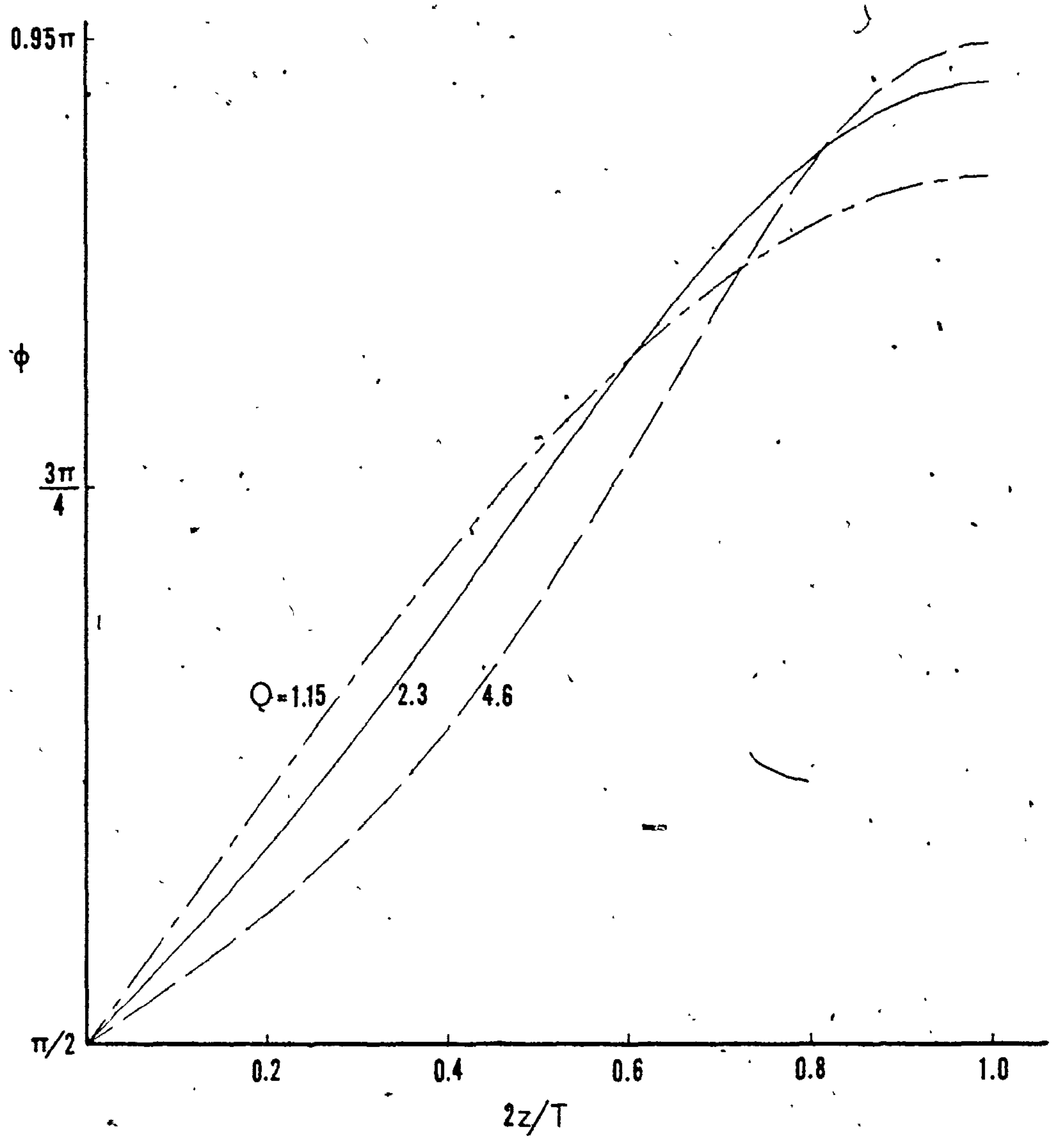

Fig. 5.7 Azimuthal angle, φ, at θ=π/2, vs. 2z/T, for bubbles in films of λ/T=0.231, Q=1.15, 2.3, and 4.6.

only a fair fit to the $\phi(z)$ profiles actually computed. DeBonte had suggested fitting $\phi(z)$ itself by the cn function, after Shirobokov [45], but this was mathematically intractable in his variational approach. However, Fig. 5.8 shows that DeBonte's function [21]

$$\phi(z) = \phi_1 \ \mathrm{cn}[(\frac{2z}{T} + 1)\ K(k_T),\ k_T], \tag{5.2}$$

where ϕ_1 and k_T are parameters and K is the complete elliptic integral, does fit very well the discrete $\phi(z)$ function found here for Q = 4.6, $\lambda/T = 0.231$.

As expected, it was found that the more curvature in the $\phi(z)$ profile (the narrower the Bloch line width), the less well could the cn function fit it. However, in general the azimuthal twist profile was well characterized by the function in Eq. (5.2) and its two parameters. The variations of the parameters with material parameters or bubble size were not investigated further, but the subject offers a promising approach to the quantitative characterization of domain wall structure, and to domain wall modelling as well.

5.4.2 Wall Bulging, r(z).

The wall radius, r(z), is defined as the radius at which $\theta = \pi/2$. We measured r(z) for a grid row by calculating a cubic spline of $\theta(r_j)$ across the row, then locating by interpolation the point where $\theta = \pi/2$. The radius is a function of z and Thiele [50] predicted it would be greater near the film midplane than near the film surface. According to his conjecture, this bulging was caused by the imbalance of stray fields from surface poles outside and in-

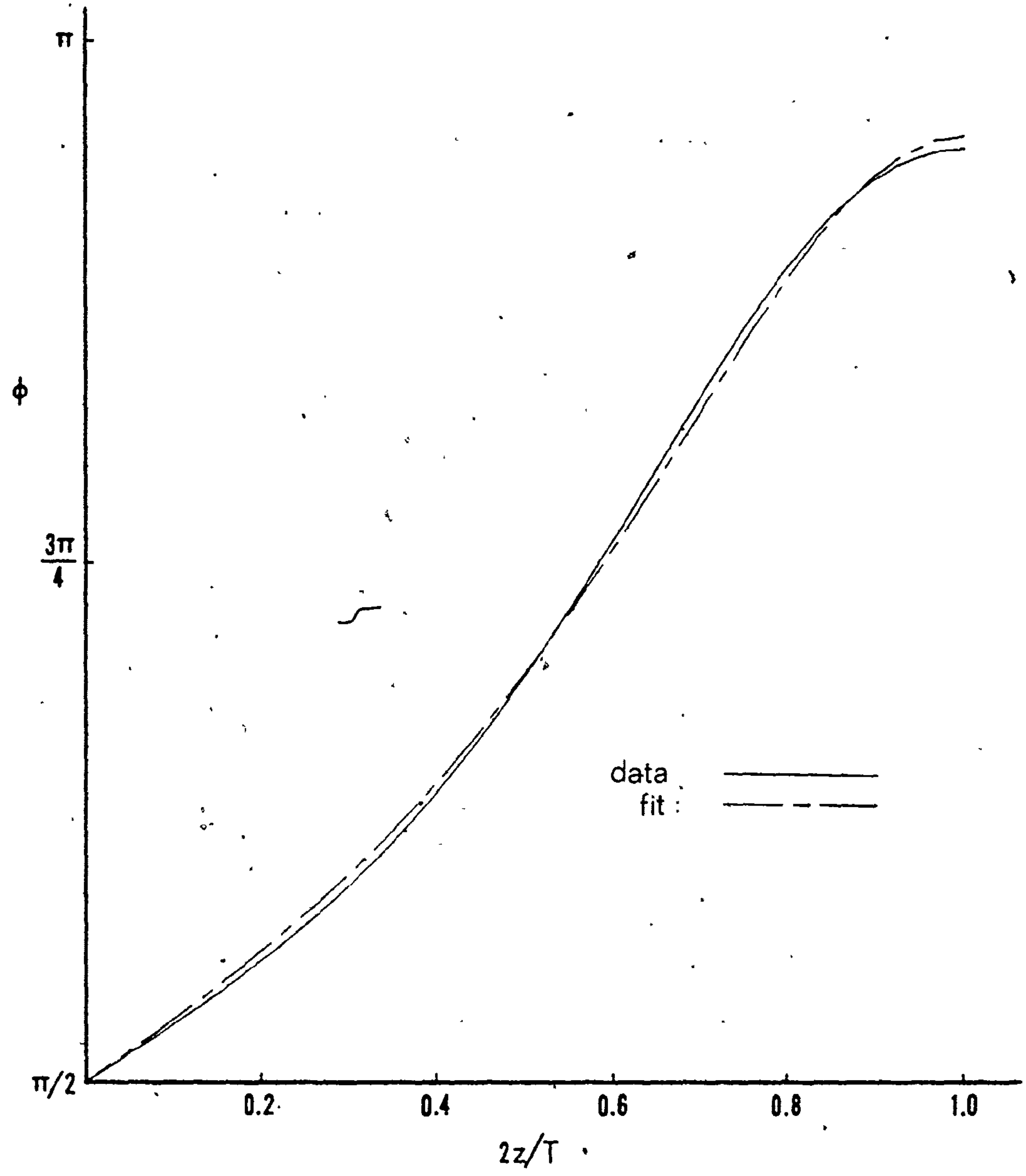

Fig. 5.8 Azimuthal angle, φ, vs. 2z/T, for λ/T=0.231, Q=4.6, with a fitted Jacobian elliptic function, cn.

side the bubble. We discuss the physical cause in section 6.4.

The radius bulging was clearly observed in Figs. 5.1, 5.3, and 5.5, but it is explicit in a graph of r(z) vs. z. The form of these profiles has been presented before [4]; in Fig, 5.9 we show the same data, normalized to the reciprocal of the aspect ratio of the respective bubble. That is, we plot $\frac{2r_o}{T}(r(z)-r(0))$ vs. 2z/T. The curves are from bubbles in a film of $Q = 2.3$, $\lambda/T = 0.231$ (see Table 6.1) at different bias fields, near collapse, near runout, and in between.

We note that the individual curves are smooth, showing little structure or localization near the film surface at $z = T/2$. In fact, near the surface, $\frac{\partial r(z)}{\partial z}$ decreases and the profile has qualitatively the shape predicted by Thiele [50].

For fixed film thickness T, we expect the amount of bulging to depend inversely on the film surface area of the bubble interior, since the smaller that area, the greater the imbalance in domain fields. Of course, we do not expect the dependence to be as simple as linear, but studying $\frac{2r_o}{T}(r(z)-r(0))$ gives an idea of the order of the dependence.

The curves of Fig. 5.9 have the same shape as those of [4], but the normalization has brought their maximum values closer together and reversed their order. The total bulging increases with decreasing radius [50,4], but Fig. 5.9 shows that the dependence is slightly less than linear for this film: normalization to a linear function of mean domain radius more than overcomes the dependence.

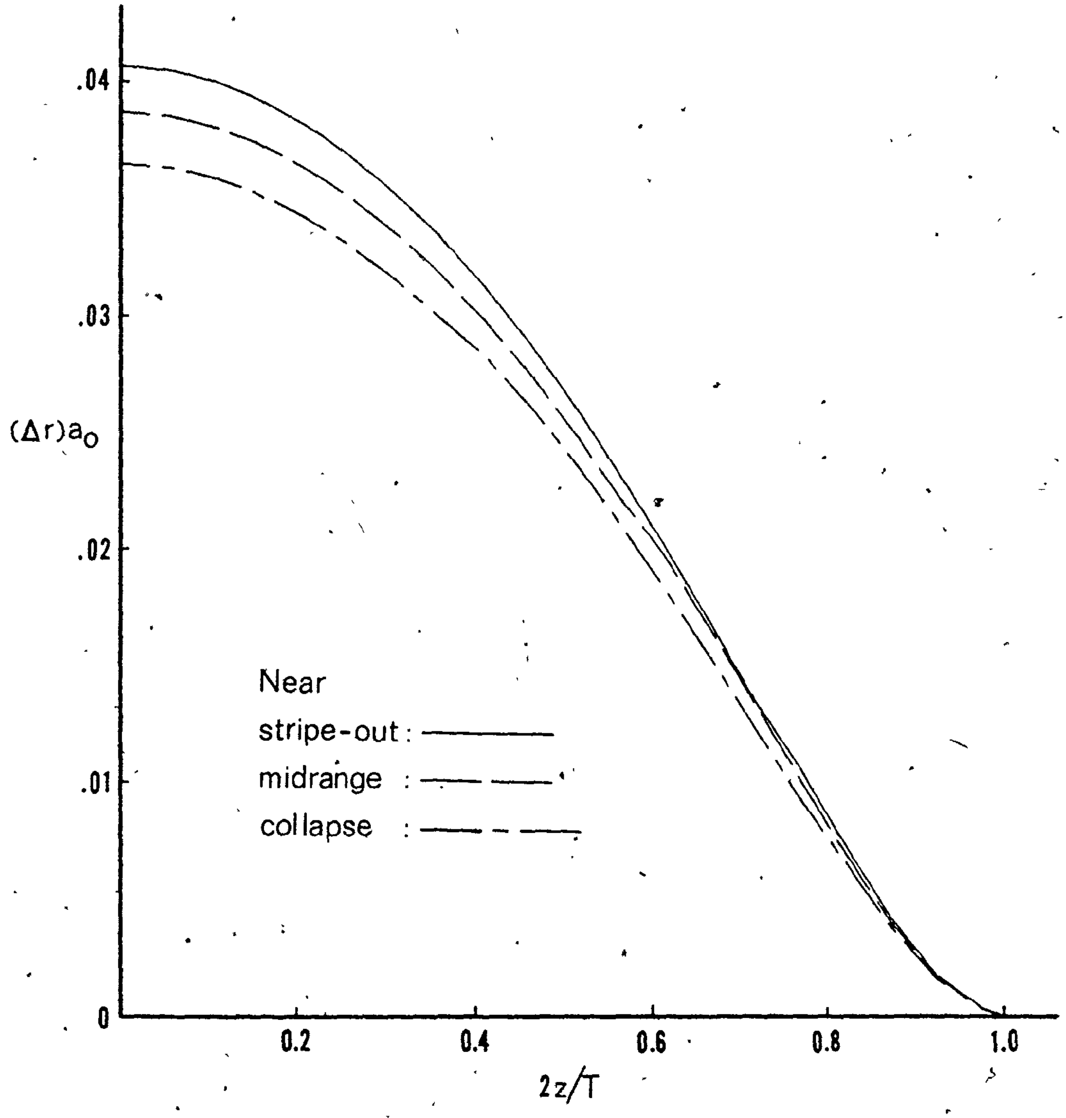

Fig. 5.9 Wall radius bulging normalized to reciprocal aspect ratio, $(2\,r_o/T)(r(z)-r(0))$ vs. $2z/T$, for three bias fields; $\lambda/T=0.231$, $Q=2.3$.

Since, given the finite, approximately fixed, wall width, the film surface area of the interior domain is a slightly stronger than quadratic function of r_o, this is perhaps an unexpected result. However, there are many complicating factors, including the diffuse nature of the wall and the nonuniformity of the demagnetizing fields. Since bulging is unique to curved domain walls, and their study is mathematically formidable [50], it is unlikely to be amenable to a simplified analysis such as that of Nedlin [38], who predicted bulging would increase with domain radius.

5.4.3 Wall Width, w(z).

The wall width could be defined as the distance between two values of m_z, say 8% and 92% of the total variation in m_z from one side of the wall to the other (compare section 2.5.1). Another approach is to linearly extrapolate the m_z profile from its slope at the centre of the wall (where $m_z=0$) to the extremal values $m_z=\pm1$, and define the distance between these values as the width of the wall. We have chosen the latter definition [17], which may be written as

$$w(z) = \pi/\left(\frac{\partial m_z}{\partial r}\right)_{m_z=0} \tag{5.3}$$

The discussion of section 5.2 suggests that the width by this definition does not give the whole story - identical slopes can occur between wall "edges" of different separation - but it is the conventional definition and the results presented here will be informative within its limitations.

As noted in sections 5.2 and 5.3, the wall width is also a function of z. The wall width for each row was measured from the cubic spline of $\theta(r_j)$ mentioned in section 5.4.2. After $r_o(z)$ was located, the derivative of the spline was evaluated at that point and the value of w(z) was calculated from Eq. (5.3).

Broadening of the wall near the film surface has been observed in finite-difference plane-wall models [43,29]. The contour maps in Figs. 5.5 and 5.6 show it quite clearly, although it is the separation of θ values that is visible, not the width defined from the slope of the $\theta(z)$ profile.

In a normal bubble wall (cf. section 5.5 below), a minimum width occurs at the film midplane, where z=0. (We will return to this point in section 6.2.1.) In Fig. 5.10 we plot w(z)-w(0), in units of film thickness, as a function of 2z/T. Again, the bubbles are at different bias fields in the film having $\lambda/T = 0.231$ and $Q = 2.3$.

We see that the width flaring is localized near the surface in this film, but that very near the surface, the width increase levels off, consistent with the boundary condition (Eq. (2.34)). Also, the flaring decreases with aspect ratio, as the bubble interior gets smaller.

Schlömann [39] and DeBonte [21] found an increase in wall width but their models did not admit flaring; θ was a function of r only, so the width of the wall was constant with z. Our results indicate that the width near the film midplane is close to, but slightly less than, that of a pure Bloch wall in the material.

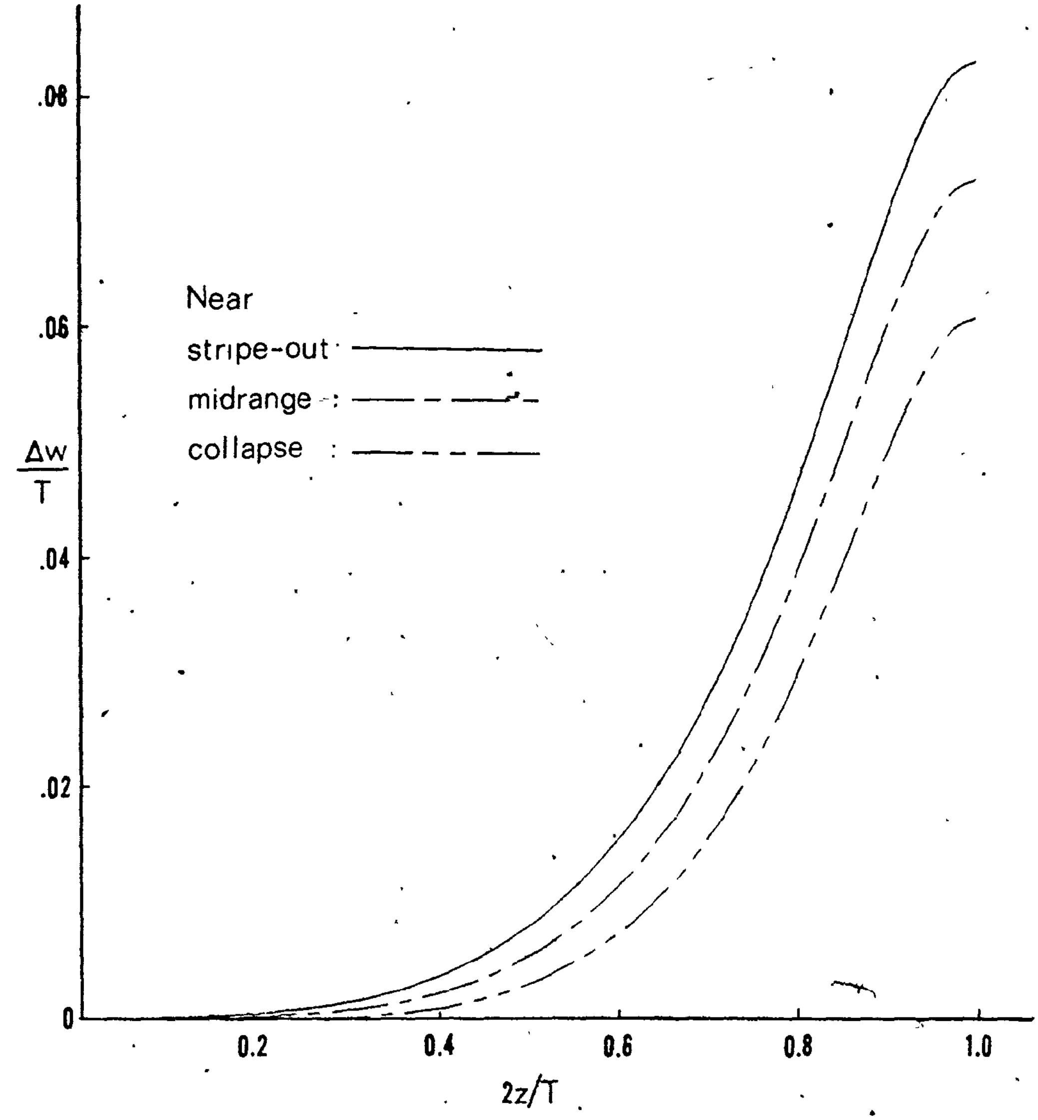

Fig. 5.10 Wall width flaring (w(z)-w(0))/T vs. 2z/T for same bubbles as Fig. 5.9.

In view of this fact and the observed flaring near the surface, the assignment of the same width to the entire wall is apparently a major approximation for low-Q domains.

5.5 WALLS CONTAINING HORIZONTAL BLOCH LINES

In a Bloch-type wall, the magnetization has zero component perpendicular to the wall plane. At the centre of such a wall, the magnetization may, with equal energy, point in either direction parallel to the wall tangent in the film plane. This opens the possibility of magnetization taking each direction in a different region of the same wall, the regions being separated by intervals of twist called Bloch lines. Theoretically, both horizontal and vertical Bloch lines are energetically possible in static bubble walls [37,41], although they are created dynamically [37] and are particularly important in wall motion [48]. Due to the requirement of cylindrical symmetry, the calculation discussed in this thesis can model only the horizontal Bloch lines (HBLs).

Bloch lines must occur in pairs, which have a total twist of 2π. In this work, bubbles were modelled from an initial configuration which included a twist in $\hat{m}(z)$ of 2π, centred on the film midplane, so only one of the Bloch lines (a twist of π) will appear in the grid. The boundary conditions did not demand that the twist be maintained, but there was apparently an energy barrier to unwinding, as expected.

In this section we discuss the results of a limited investigation of the structure of HBL-containing walls. As well as being of interest in themselves, these results will help promote the understanding of certain features of normal walls.

Figures 5.11 and 5.12 are arrow maps of $\hat{m}_i$ projections on the $\hat{r}$-$\hat{z}$ and $\hat{r}$-$\hat{\alpha}$ planes, respectively, for a wall having an HBL pair in a film of $Q = 2.3$, $\lambda/T = 0.231$, $T = 1.2$ μm, $M_s = 35{,}301$ Amp/m. In Fig. 5.12, the $\hat{r}$-$\hat{\alpha}$ map, if we follow the wall centre (where $\hat{m} = m_r\hat{r} + m_\alpha\hat{\alpha}$) from the bottom row (film centre) to the top, we see $\hat{m}$ rotate from the $-\hat{\alpha}$ direction ($\phi = -\pi/2$) through the $+\hat{r}$ direction ($\phi = 0$) and the $+\hat{\alpha}$ direction ($\phi = \pi/2$), completing the Bloch "line", and then $\hat{m}$ continues toward the $-\hat{r}$ direction ($\phi = \pi$) at the top, the film surface.

In Fig. 5.11 it is clear that the wall is of the Bloch type in the bottom row between the two Bloch lines, due to symmetry, and it is of the Bloch type again between the seventh and eighth rows, at the top of the visible Bloch line. Between these Bloch-type regions, at the fourth row, the wall is of the pure Néel type.

Figure 5.13 shows the $\phi(r)$ profiles for all the rows. The profile is constant not only for the film midplane row, where $\phi = \pi/2$ by symmetry, but also where the wall is locally of the Néel type, $\phi = 0$, in the fourth row. Near the wall centre, the profiles concentrate near the Bloch-like profiles and away from the Néel-like profiles; this indicates that the Bloch structure is energetically preferred. The Néel segments of the wall have demagnetizing fields set up across the wall in the direction

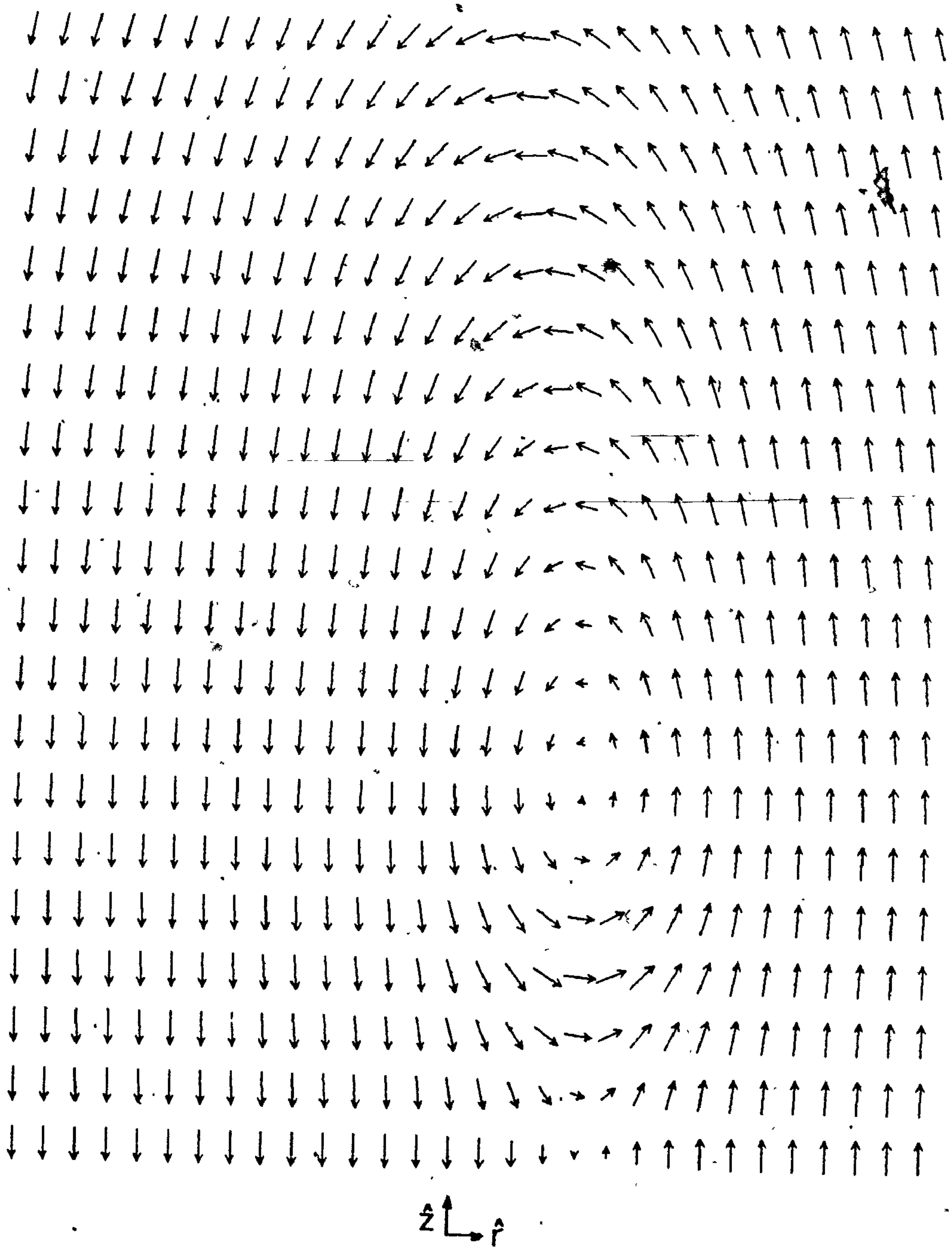

Fig. 5.11 Horizontal Bloch line wall, projections of $\hat{m}_i$ on $\hat{r}$-$\hat{z}$ plane, Q=2.3, $\lambda/T=0.1155$, T=1.2 μm, M_s=35301 A/m.

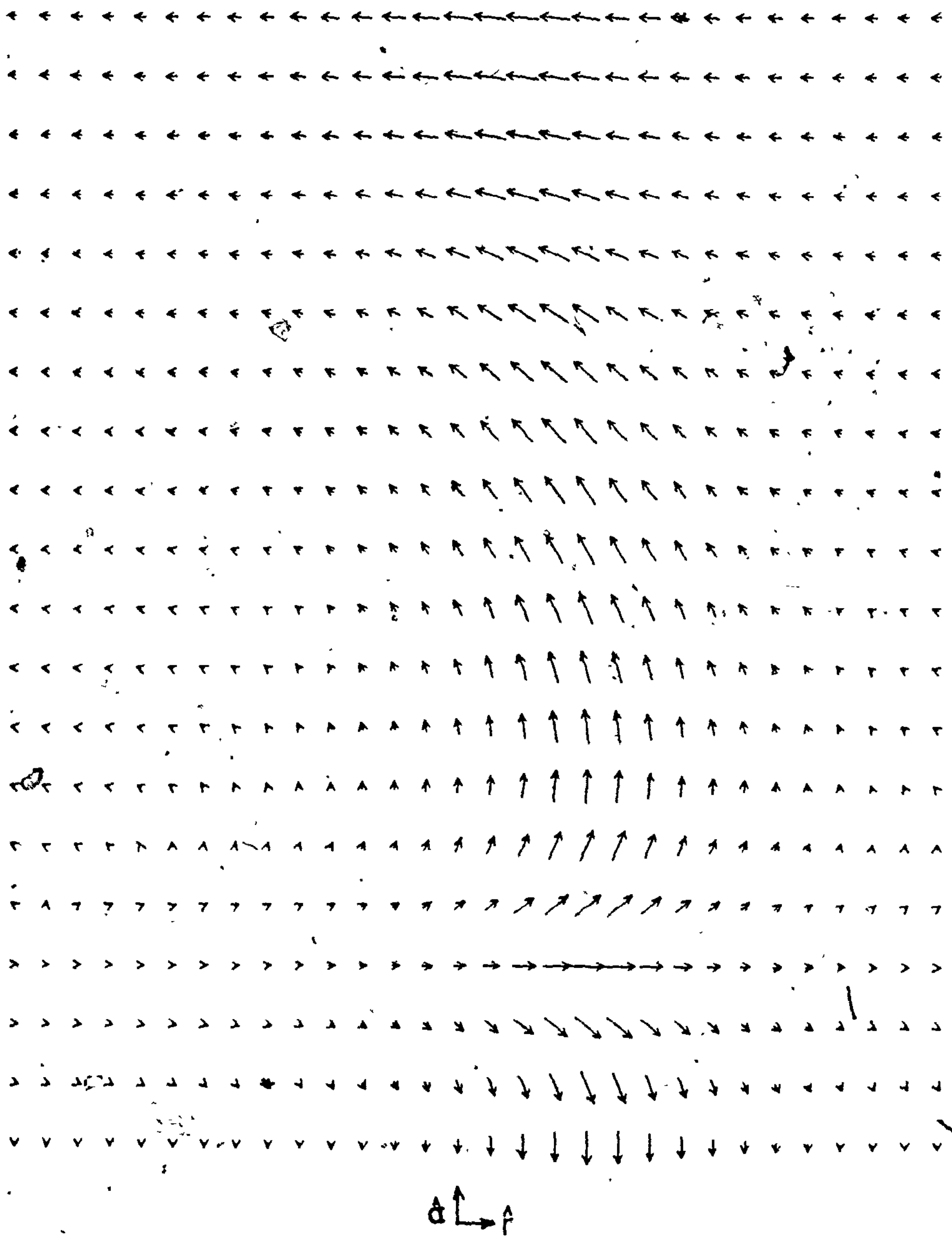

Fig. 5.12 HBL wall, $\hat{m}_i$ projections on $\hat{r}$-$\hat{\alpha}$ plane; film of Fig. 5.11.

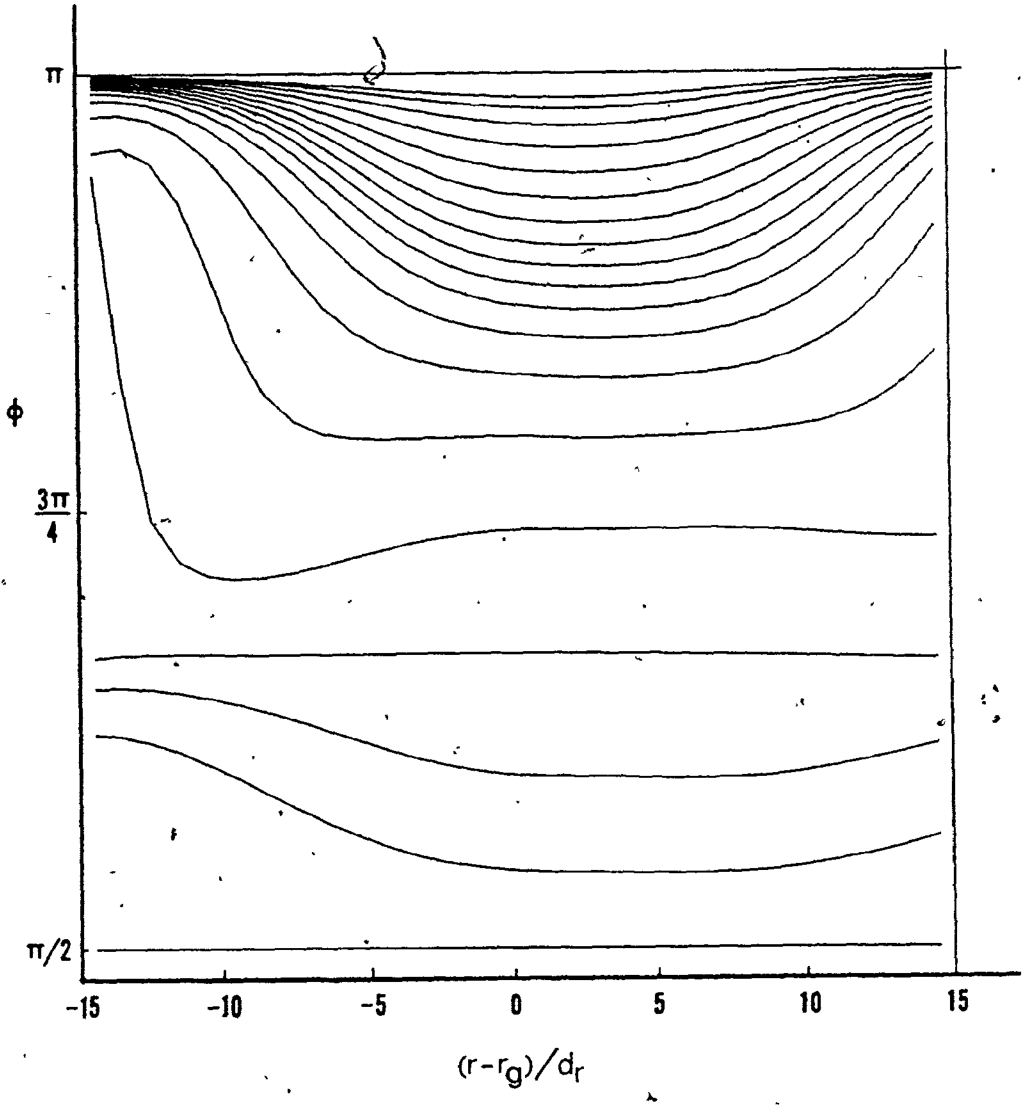

Fig. 5.13 HBL azimuthal angle profiles, $\phi(r)$; film of Fig. 5.11.

opposite to the magnetization, increasing their energy.

Figure 5.14 contains contour maps for an HBL wall in a material having $Q = 4.6$, $\lambda/T = 0.231$, $T = 2.4$ μm, and $M_s = 24962$ Amp/m. The wall is narrower where it is Néel-like ($\phi = 0$) in the HBL [37, p. 85]. The broadening near the surface is due to the tendency to reduce the demagnetizing fields from the film surface. The magnetization is also twisted near the surface to make the wall Néel-like, but the effect of the Néel character there is actually to counteract the broadening, at least near the wall centre (see also section 5.2).

We note also that the radial variation of ϕ, and the width flaring, are confined to the region above the Bloch line.

In the present work, we obtained solutions for two HBL-wall bubbles, the one of Figs. 5.11-5.13 and the one of Fig. 5.14; for the latter, the Q, λ/T, and T were twice those of the former, while M_s was less by a factor of the square root of two. Thus, the two films had the same ratio of classical Bloch wall width to film thickness, $l_w/T = 0.079$, and the respective grids had the same aspect ratio. However, the lower-Q film had a smaller relative Bloch line width; l_{BL} was 0.038 T compared to 0.054 T.

In Fig. 5.15 we see the effect of the smaller relative Bloch line width. The figure shows the $\phi(z)$ profiles for the two walls, plus the profile for a normal wall in the lower-Q film. The ordinate refers to the $Q = 2.3$ curves, referred to the film midplane values ($\pi/2$ for the normal wall, $-\pi/2$ for the HBL walls). Notably, the $Q = 4.6$ and $Q = 2.3$ HBL curves had

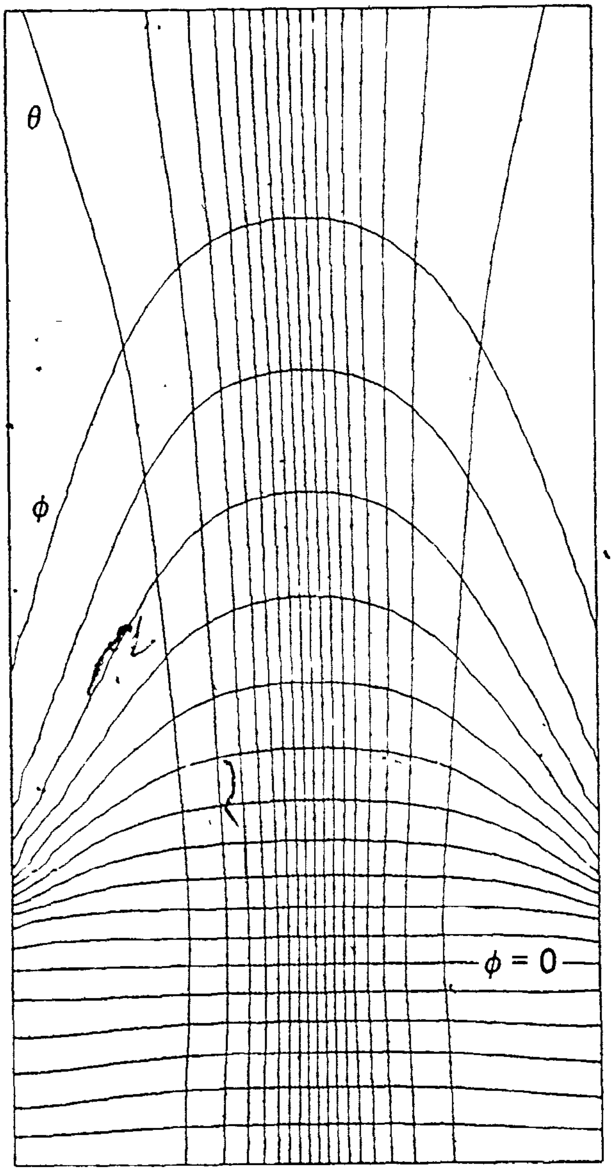

Fig. 5.14 HBL contour maps; λ/T=0.231, Q=4.6, T=2.4 μm, M_s=24962 Amp/m.

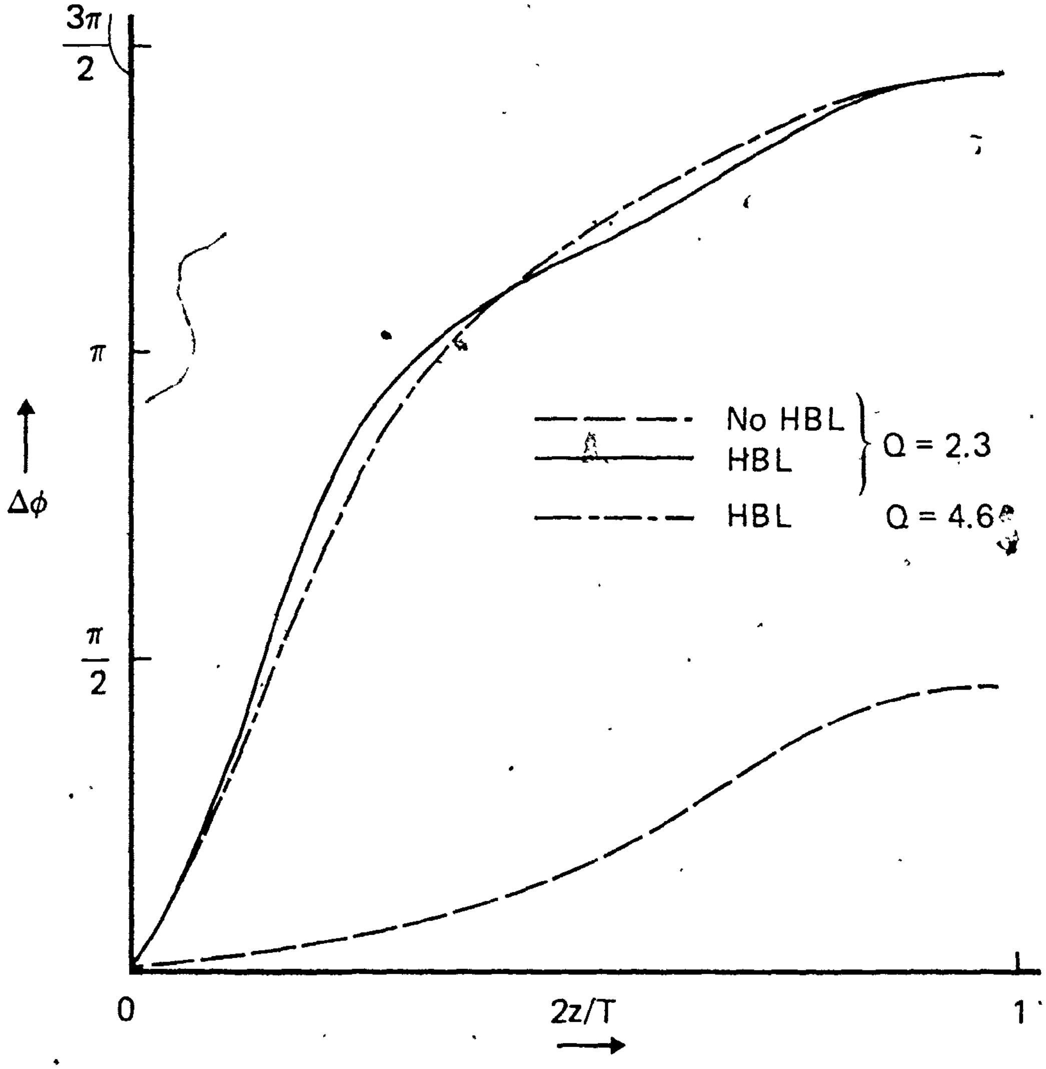

Fig. 5.15 HBL azimuthal angle profiles, $\phi(z)-\phi(0)$, for walls of Figs. 5.11 and 5.14, plus normal wall in films of Fig. 5.11.

maximum values virtually equal, at 1.465π and 1.469π respectively.

We see from Fig. 5.15 that the lower-Q, smaller line width wall had more structure, including a steeper profile in the Bloch line, than the higher-Q wall. The slopes of $\phi(z)$ near the film midplane, between the two Bloch lines, are equal relative to the film thickness; presumably this is a consequence of the equal wall region aspect ratios. Above the Bloch line, the two Q = 2.3 profiles appear to be parallel. Although the Bloch line is really an interval of some width, its structure is isolated within that width and its influence on the wall structure beyond is small.

Figure 5.16 shows the domain radius profiles, $r(z)-r(T/2)$, for the same walls as in Fig. 5.15. The two Q = 2.3 walls bulge about the same; the profile is flattened in the Bloch line region. The higher-Q, lower M_s wall bulges less than the lower Q wall, 0.021 μm to 0.029 μm, as expected; in the graph, the $r(z)$ profiles are normalized to film thickness, which was twice as great for the Q = 4.6 film, so the difference appears much greater.

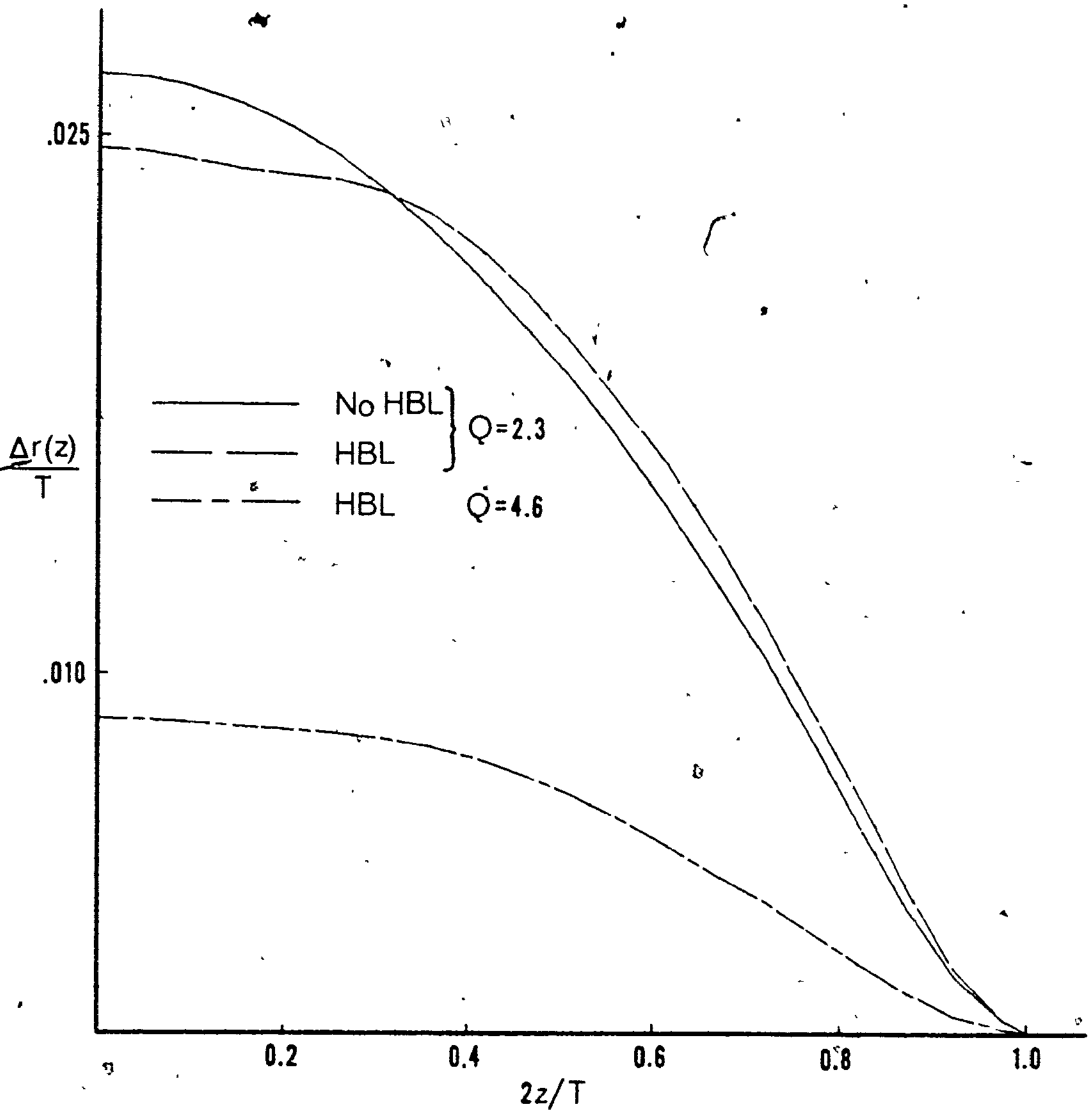

Fig. 5.16 HBL domain radius profiles, (r(z)-r(T/2))/T vs. 2z/T; films of Fig. 5.15.

CHAPTER 6

VARIATIONS OF WALL STRUCTURE PARAMETERS

6.1 INTRODUCTION

In this work, bubbles were modelled for at least three bias fields at each set of film material parameters. The different bias fields resulted in bubbles of different aspect ratios within the range of stability. In each bubble wall, quantities were measured that describe specific features of wall structure: total width flaring, maximum azimuthal twist, radial bulging, wall surface energy density, and characteristic widths of the twist and width flaring profiles. This chapter discusses the dependence of these quantities on bubble and film parameters.

One principal feature of this work is that it is distinguished from the plane-wall models by its ability to identify variation in structural features with wall curvature, or at least with domain aspect ratio. The imbalance of stray fields from the domain regions inside and outside the bubble (inside the curvature and outside it, for general curved walls) is probably more important than the local wall curvature itself.

We have plotted graphs of the aforementioned structural quantities as functions of reciprocal aspect ratio, $1/a_0$ (which we refer to as "curvature"), because for a plane wall, $1/a_0 = 0$

so the extrapolation for comparison to plane-wall studies is straightforward.

As was noted above, the different aspect ratios were obtained under different bias fields. The direct effects of bias field variations were neglected; after the bubble reaches its equilibrium aspect ratio, the $\hat{z}$-component of the demagnetizing field would at least partly counteract the change in bias field that altered the aspect ratio.

The structural quantities were measured from the final wall configurations. Profiles were obtained by interpolating cubic splines of θ calculated for each row, as described in section 5.4.2. Values of the quantities at the film surface were calculated by extrapolation of the cubic polynomial associated with the surface boundary condition and with Eq. (2.38). The locations where the respective quantities were equal to half their surface values were determined by interpolation of a cubic spline of the profile.

The material parameters were chosen as follows. The film thickness, T, and uniaxial anisotropy constant, K_u, were fixed at 1.2 μm and 1800.87 J/m^3 respectively. Materials then were fully defined by pairs of values of $Q = 2K_u/\mu_o M_s^2$ and normalized material length $\lambda/T = 4\sqrt{AK_u}/\mu_o M_s^2 T$. (These symbols are defined in section 1.2.)

This meant that, with K_u and T fixed, increasing M_s caused λ/T and Q to decrease, producing smaller bubbles (λ/T decrease) and reducing their stability (Q decrease). This is true to experience in bubble technology. However, it should be noted that decreasing λ/T at fixed Q, M_s, T, and K_u causes A to decrease as $(\lambda/T)^2$. The exchange constant is not easily measured, but is commonly assumed not to vary much with film composition, so this dependence of A on λ/T should be remembered when studying the results presented here.

Table 6.1 displays the material parameters of all the films studied. The first material parameters, $\lambda/T = 0.231$, $M_s = 35301$ Amp/m, $T = 1.2$ µm, were obtained from Almasi [2], where $\lambda = 0.227$ µm, $4\pi M = 443.6$ Oe, $T = 1.2$ µm, and Q was not given. The other parameters were set to be factors and multiples of these, subject to the need to keep the grid away from the bubble axis (hence the lowest Q was 1.4), and to fill the gap between $\lambda/T = 0.231$ and 0.462.

Secondary material parameters of interest are the Bloch wall width, $l_w = \pi\,(A/K_u)^{\frac{1}{2}}$ and the Bloch line width [37, p. 85] $l_{BL} = (2A/\mu_o M_s^2)^{\frac{1}{2}}$. The first gives a rough idea of the relative width of the bubble wall region while the second suggests the amount of "structure", or $\partial^2\phi/\partial z^2$, in a wall having azimuthal-angle twist.

The two widths would characterize their respective profiles in the same way (Eq. (1.9)) if the expression for l_{BL} were preceded by π; but we will maintain their conventional definitions) Table 6.2 lists the values of l_w and l_{Bl} for the films of Table 6.1. As indicated by the discussions of sections 5.4.3 and 5.5, these numbers are for comparison only. Actual wall structures are not as simple as they suggest.

Table 6.1. Material Parameters

	Q:	1.4	2.3	4.6
	M_s (Amp/m):	45207	35301	24962
	$4\pi M$ (Oe):	568.1	443.6	313.7
λ/T	$A(10^{-11}$ J/m):			
0.05775		0.1099	0.0409	0.0102
0.1155		0.440	0.1635	0.0409
0.231		1.759	0.654	0.1635
0.3465		3.957	1.471	0.368
0.462		7.035	2.616	0.654

$T = 1.2\ \mu m$, $K_u = 1800.87\ J/m^3$.

Table 6.2. Wall Structure Characteristic Widths

	Q:	1.4	2.3	4.6
	l_w/λ:	1.122	0.683	0.341
λ/T	l_w/T, l_{BL}/T:			
0.05775		.0648	.0394	.0197
		.0244	.0190	.0135
0.1155		.129	.0789	.0394
		.0488	.0381	.0269
0.231		.259	.158	.0789
		.0976	.0762	.0539
0.3465		.389	.237	.118
		.146	.114	.0808
0.462		.518	.316	.158
		.195	.152	.108

The mean stable aspect ratio for a film is a strong function of its normalized material length, λ/T (see Fig. 1.3). This means that the dependence of structural quantities on aspect ratio and material parameters could be confused. After various graphs of subsets of the data were plotted and found to leave physical relationships obscure or incompletely depicted, the following approach was adopted.

The structural quantity to be studied was measured from each bubble wall configuration and plotted on the same graph as a function of curvature, $1/a_o$. That is, every bubble modelled, in every film, supplied a point to the graph. The points for different aspect ratios in each film were grouped in the graph by a curve or straight line drawn manually (not numerically fitted) through them.

The four digits labelling each curve (1406, 2323, etc.) were determined as follows. The first pair of digits are equal to ten times the film's Q value, while the latter pair are equal to one hundred times the λ/T value (see Table 6.1).

Although these graphs contain many data points and lines, from the associated discussions it will be apparent that they give more insight than separate collections of median values or slopes would.

6.2 WALL WIDTH

The wall width, a function of z, is defined in section 5.4.3. In this section we discuss two aspects of its variation.

6.2.1 Bloch Wall Width at the Film Midplane.

At the centre of the film, where by symmetry the wall is of the pure Bloch type (m_r=0), the width w(0) was found to be slightly less than the material characteristic Bloch wall width, $l_w = \pi\sqrt{A/K_u}$ [17]. Values of $w(0)/l_w$ were in the range 0.90 to 0.99; most were between 0.94 and 0.97.

There were no apparent trends in the variation of $w(0)/l_w$, except that for the film having Q = 1.4 and λ/T = .05775, there seemed to be an increase in $w(0)/l_w$ with decreasing aspect ratio. The linear least-squares fit was $0.867 + 0.048/a_o$, with a correlation coefficient of 0.994.

Although the wall is of the Bloch type exactly at the film centre, stray fields from above and below that point evidently have the effect of slightly narrowing the wall profile there. Since for the 1406 film the effect was reduced, that is, w(0) approached l_w as the bias field increased, the bias field is ruled out as the direct cause of the w(0) narrowing. The increase in effective uniaxial anisotropy from the α-variation of $\hat{m}$ in the exchange field expression (section 2.2.4) would also narrow the wall, but again, the trend would be opposite to that observed in the 1406 film. This leaves as the possible cause the aforementioned stray demagnetizing fields; the situation is similar to the narrowing of Néel wall segments [37].

6.2.2 Total Wall Width Flaring.

To reduce the demagnetizing fields and energies at the film surface, the polar angles of the magnetic moments near the wall there are increased, so that the magnetization is reoriented toward the film plane and the wall is broadened [43]. We define the relative wall width flaring as

$$\Delta w = (w(T/2) - w(0))/w(0). \qquad (6.1)$$

In Fig. 6.1, this quantity was plotted against curvature, $1/a_o$ for all the films studied.

It is apparent from the figure that the flaring decreased as $1/a_o$ increased; as the bubble interior shrank so did its contribution to the total stray field. The flaring increased strongly with M_s (decreasing Q); the effect of the increasing exchange constant A (Table 6.1) was allowed for by defining the flaring to be normalized to w(0), which is also dependent on A.

There is also shown a decrease in flaring with increasing material length. This trend was in opposition to the aspect ratio dependence. (We note that the 4606 data did not follow this pattern; this film did not permit convergence for the smaller aspect ratios, and the inconsistent results will be noted again in later sections.) At fixed Q, the smaller material lengths correspond to smaller values of l_w and therefore of w(0), so the relative flaring (Eq. (6.1)) increased with decreasing material length.

The absolute wall width flaring, w(T/2)-w(0), not shown, followed the opposite trend, decreasing with decreasing material length. The reason is that in this work, the exchange constant decreased with material length, reducing its contribution to broadening the θ profile.

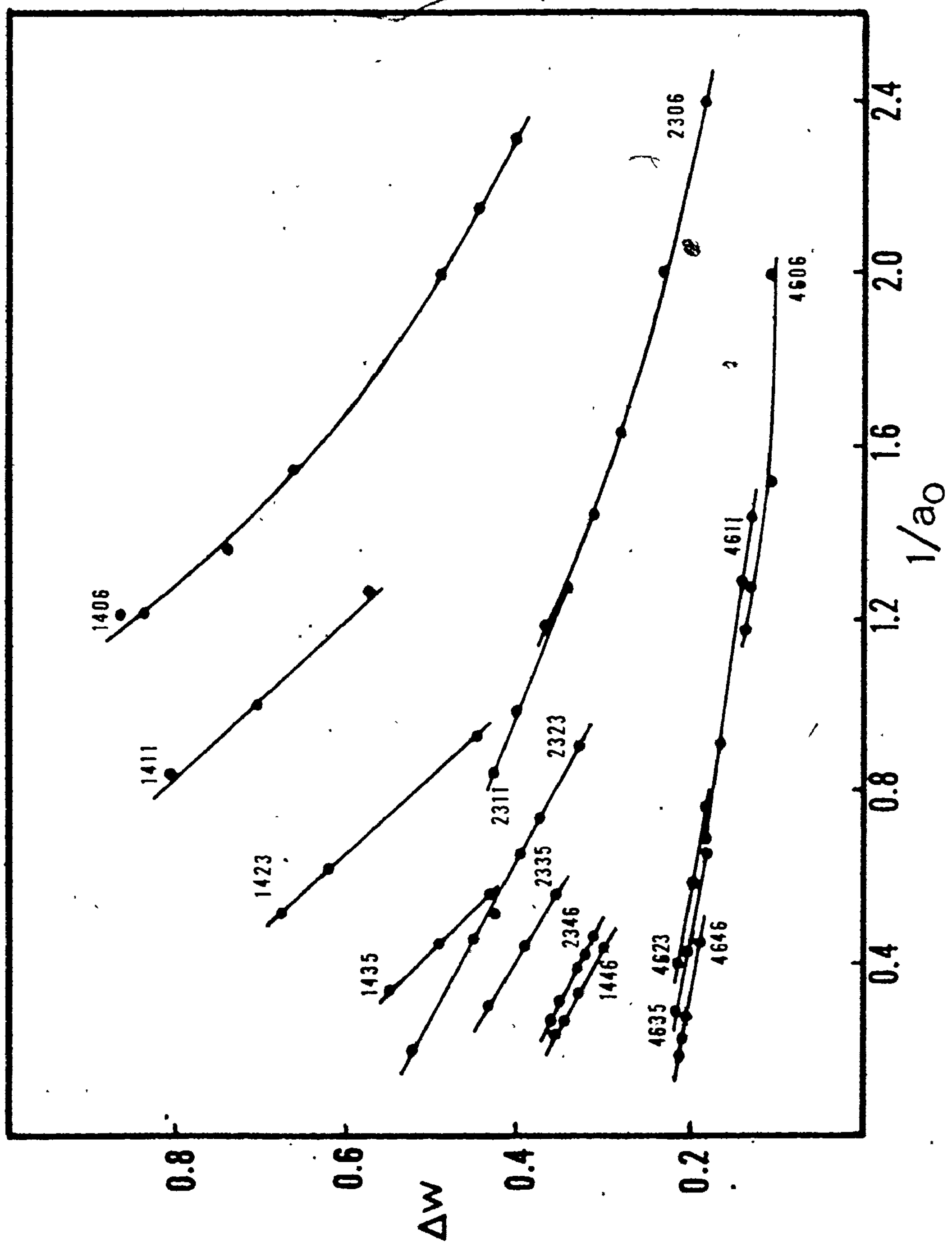

Fig. 6.1 Relative wall width flaring, Δw, vs. $1/a_o$, all bubbles.

In the range of stability of each film, the flaring was close to a linear function of $1/a_o$, except for the $\lambda/T = .05775$ films. For the small aspect ratios that occurred near collapse in those films, the flaring appears to level off as a function of $1/a_o$.

The linearity of the other curves is striking, as is the similarity in slopes for films having the same Q. For $Q = 1.4$, including the low-curvature points of the $\lambda/T = 0.05775$ curve but excluding the $\lambda/T = 0.462$ curve, the slopes were $-0.535 \pm .020$. For $Q = 4.6$, the slopes were $-.094 \pm .003$, except for $\lambda/T = 0.1155$, which gave a slope of -0.071. For $Q = 2.3$ and the 1446 curve which was in the same region of the graph, there was more variation in slopes, which were $-0.245 \pm .05$.

In the 1446 film, the bubbles had large aspect ratios and broad walls and, evidently, a smaller dependence of flaring on aspect ratio than the other $Q = 1.4$ films. In the other films, the slope was a strong function of Q (i.e., M_s), but not of λ/T, nor of $1/a_o$ itself. Thus, not only was the amount of relative flaring a strong function of M_s, but so was its tendency to decrease with the size of the bubble interior.

6.2.3 Localization of Flaring Near the Film Surface.

Another aspect of wall width flaring is how far it extends away from the film surface. The position of the point z at which the flaring was half the maximum value reached at the surface was defined as

$$z[\Delta w(2)] = z[w(z) = (w(T/2) + w(0))/2]. \qquad (6.2)$$

The quantity $z(\Delta w/2)$ was plotted for all the modelled bubbles in Fig. 6.2. The distance from the surface, $z = T/2$, to this point has been called the halfwidth [21].

All films studied had the halfwidth point more than halfway from the film midplane to the surface, probably because $dw(z)/dz$ must be zero at $z = 0$, by symmetry. The 4606 points at high curvature were out of place; the algorithm did not converge for those runs (see section 6.4).

It is also seen from the figure that the larger the nominal wall width (proportional to $Q/(\lambda/T)$; see Table 6.2), the more the wall flaring spreads down from the surface into the film. The controlling variable here is not the Bloch line width (as for twist; see section 6.3); this is confirmed by comparing 2323 and 4635 in the figure and in Table 6.2.

6.3 AZIMUTHAL TWIST, $\phi(z)$

The demagnetizing field from the domain regions, directed across the wall near the film surface, twists the magnetization away from the wall tangent. (It may also be considered, in a sense, to turn the magnetization away from the film perpendicular, producing the width flaring discussed in the last section.) Analytical function approximations of this twisting have been discussed by many authors [39,37,30,21]. It is the basis for the formation of horizontal Bloch lines by breakdown or dynamic conversion [37] in the wall structure, a phenomenon which profoundly affects the motion of bubbles [37,48].

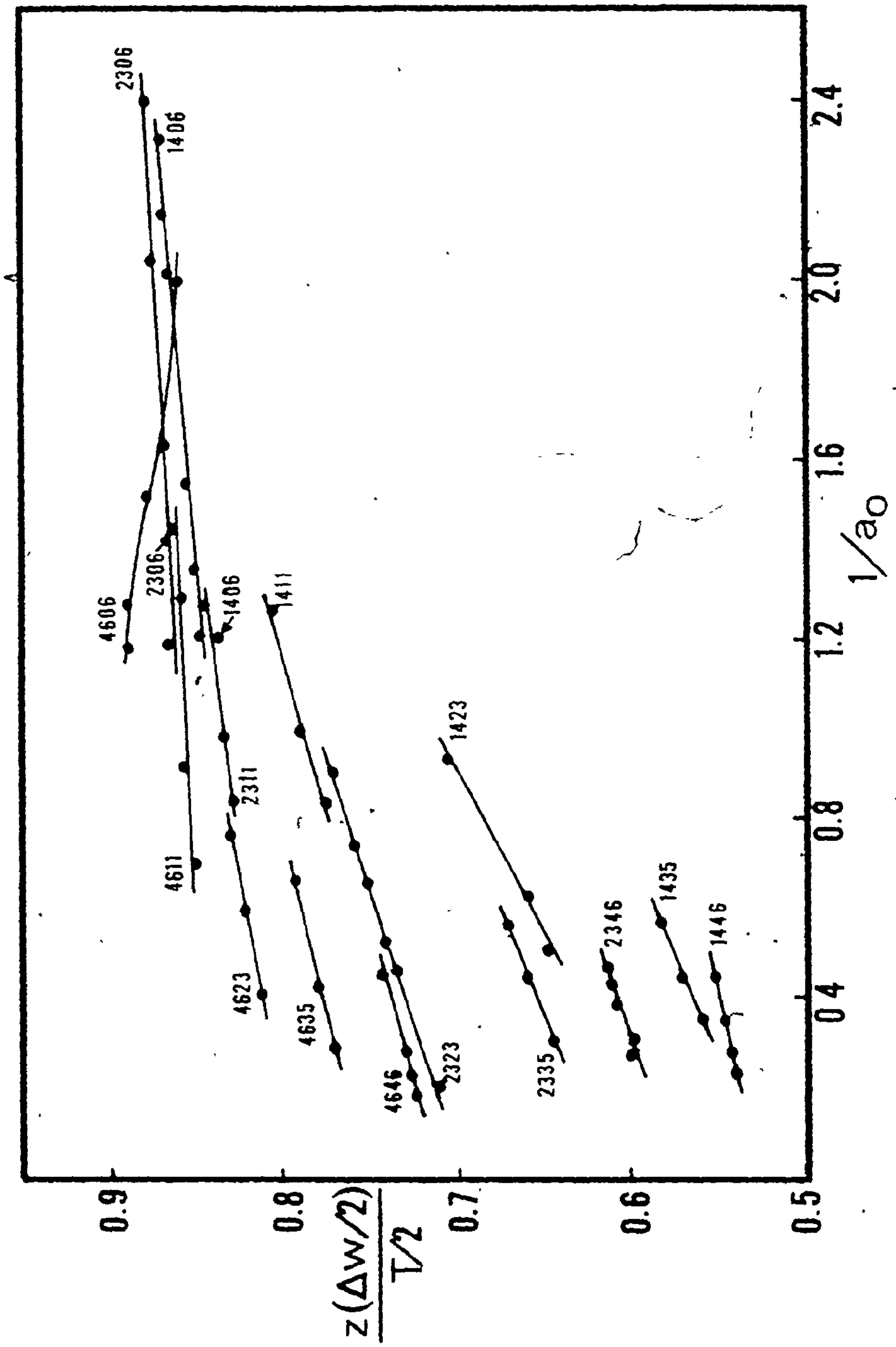

Fig. 6.2 Position of half the total width flaring reached at the surface, $z(\Delta w/2)$, vs. $1/a_o$, all bubbles.

6.3.1 Azimuthal Angle at the Film Surface.

In Fig. 6.3, we plot the amount of azimuthal twist at the top surface of the film, calculated relative to the orientation at the film midplane, $\pi/2$, and normalized to the maximum possible twist, $\pi-\pi/2$. This quantity, denoted by

$$\phi_s = (\phi(T/2) - \pi/2)/(\pi/2). \tag{6.3}$$

was plotted against $1/a_o$.

In all cases, the twist was substantial, indicating that in these uniaxial films, the wall is not at all of the Bloch type. In general, the twist increased with decreasing wall region thickness (increasing Q, decreasing λ/T), the influence of the domain fields getting stronger as the wall narrows.

This observation was also made by DeBonte [21]. We could extrapolate our curves to $1/a_o = 0$ for comparison with his plane wall results [4], but the extrapolation would be imprecise. Besides, his model did not include width flaring, an important factor for surface twist. Rather than relate azimuthal twist to an average wall width or to the classical wall width l_w of the material, we discuss below a more significant parameter, namely the nominal Bloch line width, l_{BL}.

We expect a correlation between azimuthal twist and wall width flaring, because both are due to micromagnetic effects of the demagnetizing field at the wall near the film surface. The graph in Fig. 6.3 does show a decrease in ϕ_s with decreasing a_o (decreasing size of the bubble interior and its stray field), and with increasing λ/T (increasing l_w and l_{BL}, for fixed Q and M_s).

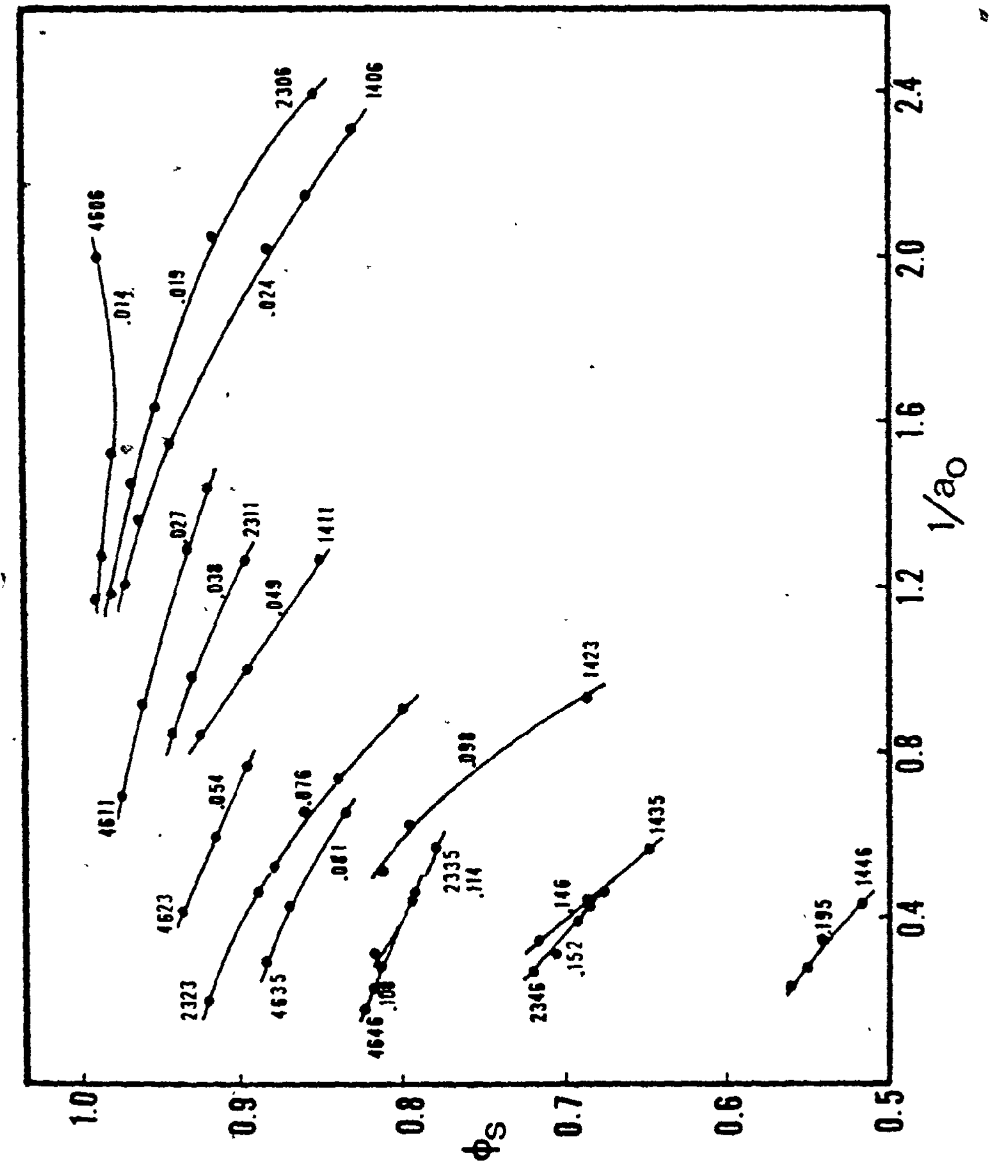

Fig. 6.3 Azimuthal wall twist reached at the film surface, ϕ_s, as normalized, vs. $1/a_o$, all bubbles; labelled by l_{BL}.

However, for fixed λ/T and a_o, the twist decreased with decreasing Q: the wider wall region was more important than the larger M_s, that is, the proximity of the domain regions to the wall centre had a stronger influence than the relative weakness of their stray fields. The effect was enhanced by the strong increase, with decreasing Q, in wall width broadening near the film surface. This result will be discussed below with reference to the material Bloch line width.

While there was a tendency for the flaring variation to level off at the smallest aspect ratios (Fig. 6.1), the opposite trend occurred for azimuthal twisting: as the bubble interiors decreased in size (approximately as the square of the aspect ratio), the decrease in twist accelerated. Also, while the curves for flaring in Fig. 6.1 were relatively straight, the curves for twist in Fig. 6.3 are nonlinear and appear to level off at large aspect ratios (low curvatures) as the wall becomes approximately planar and the domain shape becomes insignificant.

For azimuthal twist, a significant material parameter was the Bloch line width [37, p. 85], discussed in section 6.1 and defined as

$$l_{BL} = (2A/\mu_o M_s^2)^{\frac{1}{2}}. \qquad (6.4)$$

This is a characteristic width (see section 6.1) of a twist of π in magnetization along the centre of the wall, such a twist being a horizontal or vertical Bloch line. We apply it here to twists through lesser angles. The uniaxial anisotropy, K_u, is not a direct factor because the easy axis is parallel to the axis of twist; the exchange broadening of the twist is opposed only by the demagnetizing field (proportional to M_s) within the twisted part of the wall. Table 6.2 may be used to refer to the values of l_{BL} (and l_w) that result from the pairs of Q and λ/T values studied in this work.

The curves in Fig. 6.3 are labelled with their Bloch line widths. We see that, at given $1/a_o$, the twist found in each film was inversely dependent on the Bloch line width for the film. We note that films 4646 and 2335, whose curves almost coincide, have l_{BL} values of 0.108 and 0.114 respectively, and similarly, 2346 and 1435 have l_{BL} values of 0.152 and 0.146.

The Bloch line width can be large due to a large exchange constant, A. The larger the value of A, the more the twisting away from the wall tangent plane was successfully resisted by the exchange interaction, which aligns adjacent magnetic moments.

The Bloch line width can also be large due to small M_s, but the resulting broadening of the twist profile in this case (it costs less demagnetizing energy for the magnetic moments to leave the wall tangent plane) is only part of the cause of the lower total twist reached at the surface. Low M_s simply produces a smaller stray field, across the wall near the surface, from the domain regions; this field is the agent of the twisting.

However, in Fig. 6.3, ϕ_s decreased with increasing M_s (decreasing Q) as discussed above. This is explained by the fact that while M_s was proportional to $Q^{-\frac{1}{2}}$, A was proportional to Q^{-2}, so l_{BL} was proportional to $Q^{-\frac{1}{2}}$. Thus, a direct variation of ϕ_s with Q is consistent with an inverse variation of ϕ_s with l_{BL}.

6.3.2 Localization of Twist Near the Film Surface.

The shape of $\phi(z)$ may be characterized, as in the case of flaring in section 6.2.3, by the position at which $\phi(z)=(\phi(T/2) + \phi(0))/2$. This half-maximum point is, in other words,

$$z(\Delta\phi/2) = z[\phi(0) + [\phi(T/2) - \phi(0)]/2]. \tag{6.5}$$

In Fig. 6.4, this position was plotted as a function of $1/a_o$, for all the films studied.

The dependence of $z(\Delta\phi/2)$ on $1/a_o$ was relatively small; $z(\Delta\phi/2)$ increased slowly with the wall curvature. Evidently as a_o decreased, the decrease in the wall's ϕ twist at the surface was greater than the decrease in twist deeper in the film.

We note a large degree of coincidence among the curves of similar nominal wall width, l_w (proportional to QT/λ). Also, the $z(\Delta\phi/2)$ poi[illegible]e surface with increasing l_w, as predicted by De[illegible] However, the Bloch line width was not a consistent deter[illegible]t of $z(\Delta\phi/2)$; for example, the larger M_s of the 2323 film moved the half-maximum points further from the surface than those of the 4635 film, while the l_{BL}/T values were 0.0762 and 0.0808, respectively (Table 6.2).

In general, the twist extended down from the film surface more than did the wall width flaring (section 6.2.3), and for twist, the half-maximum point was in many cases less than halfway from the film midplane to the surface. The latter property would be likely to occur when $\partial\phi/\partial z$ is not zero at the film midplane.

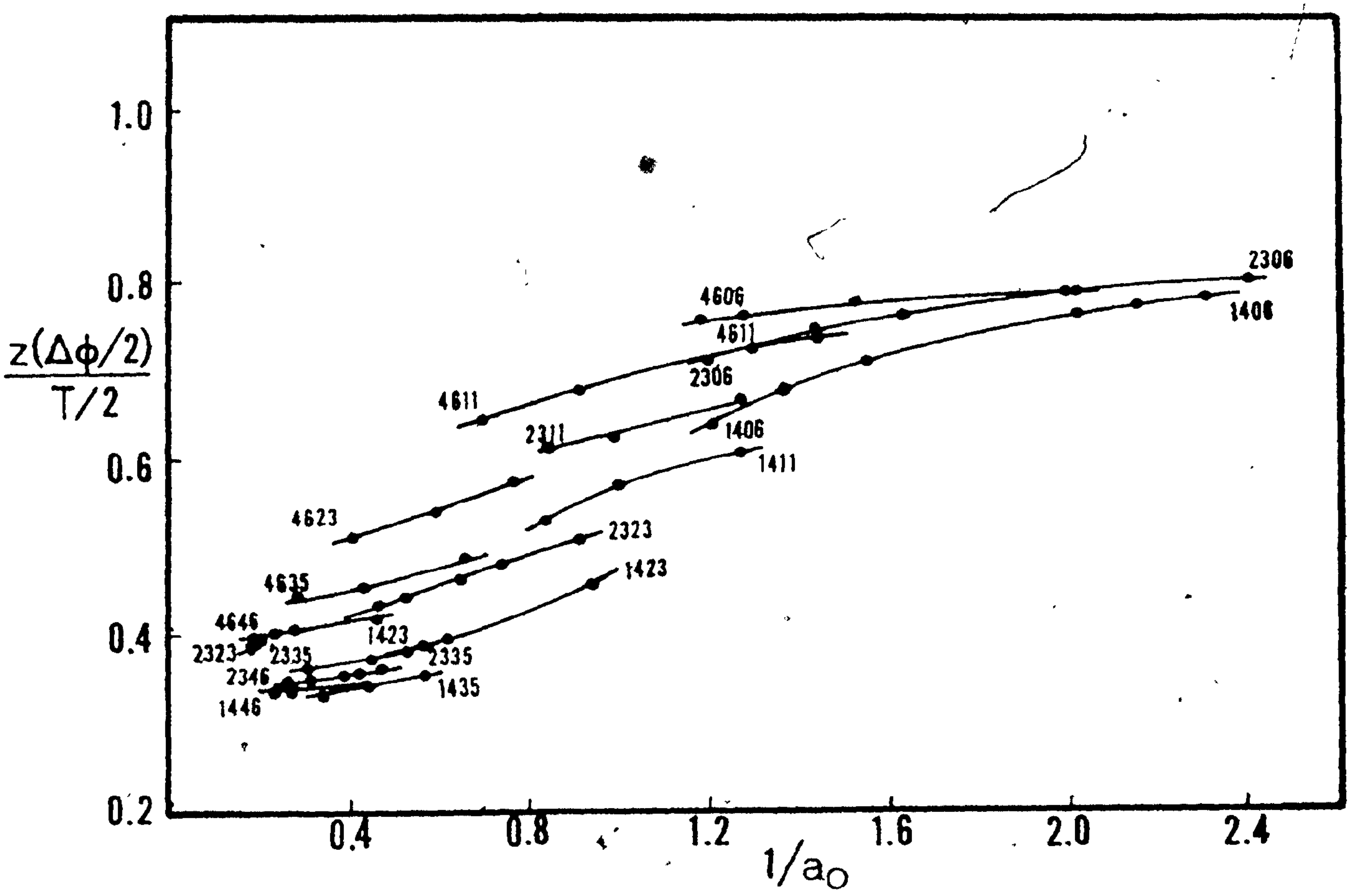

Fig. 6.4 Position of half the maximum (surface) azimuthal twist, $z(\Delta\phi/2)$, vs. $1/a_o$, for all bubbles.

Thus, a comparison of Figs. 6.2 and 6.4 suggests a basic difference between wall width flaring and azimuthal angle twisting. While flaring was localized near the surface, and hence is associated with the removal of magnetic poles on the surface, the twisting, on the other hand, is strictly due to stray fields directed across the wall between the domain regions and therefore extends into the film (as does div$\cdot\vec{M}$), to a degree that depends on the material.

6.4 WALL RADIUS BULGING

As predicted by Thiele [50], the bubble radius (at $\theta=\pi/2$) is larger at the film midplane than at the film surfaces. The $(-\hat{z})$-directed stray field from the infinite domain exterior to the bubble is not completely balanced by the $(+\hat{z})$-directed field from the finite interior of the bubble, and the net field is greatest at the film centre. It opposes the bias field, so wall bulging results.

We define a dimensionless quantity of radius bulging as

$$\Delta r/T = (r(0) - r(T/2))/T. \tag{6.6}$$

This quantity is a measure of how much the wall would appear to bulge if it were viewed in cross-section.

The data from all the modelled bubbles is presented in Fig. 6.5. Within each film, the bulging is seen to increase with decreasing bubble radius, contrary to the prediction of Nedlin [38]. This result was certainly expected; for a given wall thickness, smaller aspect ratio bubbles have a greater imbalance be-

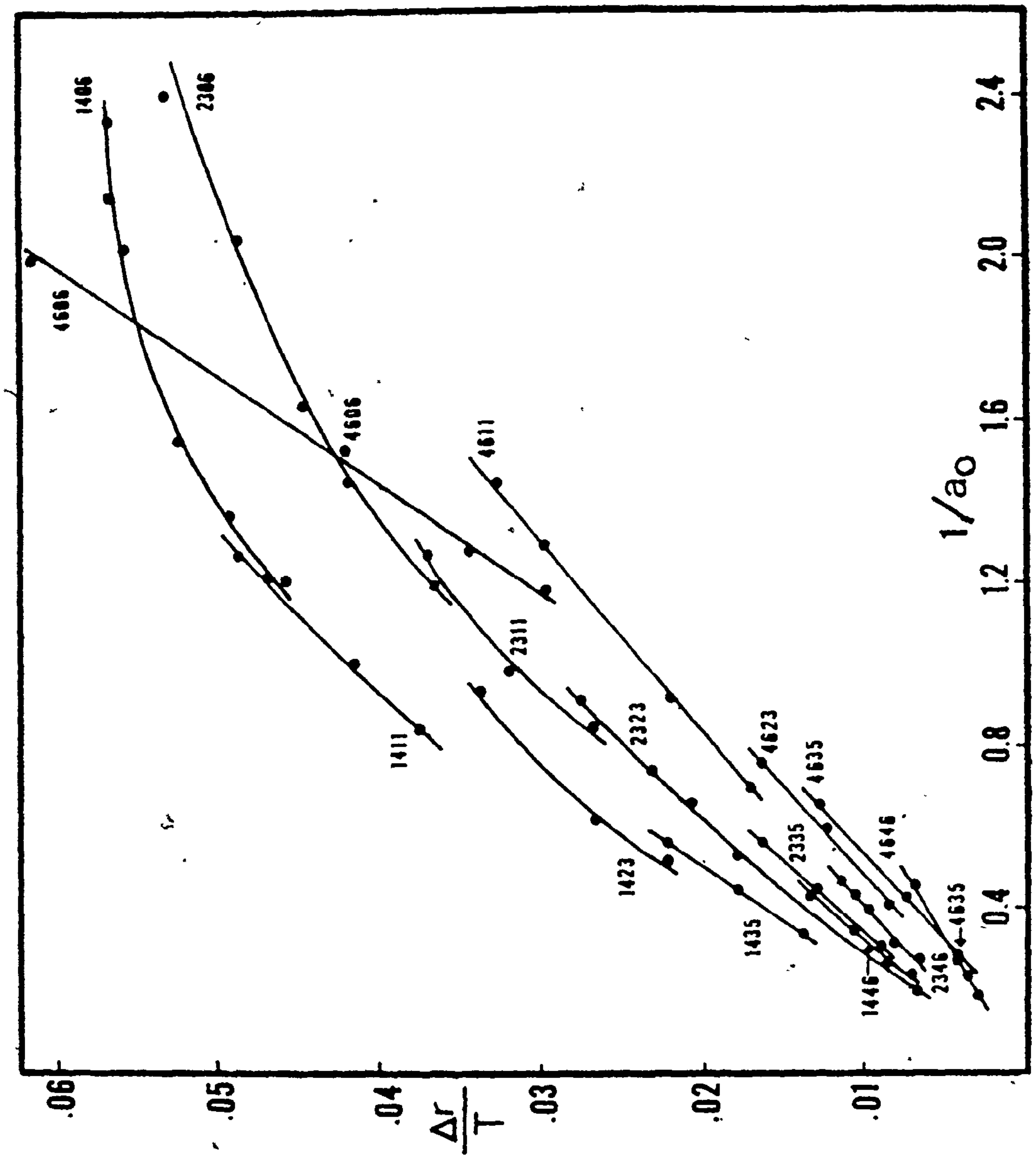

Fig. 6.5 Domain wall radius bulging, (r(0)-r(T/2))/T, vs. $1/a_o$, for all films.

tween the stray z-fields from inside and outside the wall curvature. As l/a_o approaches zero, the bulging tends to vanish, as the symmetry of a plane wall requires.

Each value of λ/T corresponds to a certain range of aspect ratios, over which bulging increased with decreasing Q. In this work, Q was lowered by increasing the magnetization M_s, which produces the stray fields that give rise to the bulging. In addition, decreasing Q at fixed λ/T increased the wall width, so the bubble's smaller interior would also result in a larger imbalance in the stray z-field in the wall.

At the smallest aspect ratios in the films of smallest material length (0.05775), the bulging increase appears to level off, especially for the film having lowest Q(=1.4). There is, of course, a limit to the bulging-inducing imbalance of stray z-fields, as the bubble interior becomes very small, as it does especially when the wall is wide for low Q.

The 4606 solutions, especially those having the two smallest a_o values, were suspect because they did not meet the convergence criterion (section 4.3). We have noted above (section 6.2.2) where the 4606 points did not follow the pattern set by the other films; this behaviour is extreme in Fig. 6.5. The thinness of the 4606 walls, the relatively large bulging, and the high degree of localization of width flaring near the film surface (Fig. 6.2) may have combined to destabilize the bubble [50]. In the 4606 bubbles of smaller aspect ratios, there was a minimum in θ with respect to r ~~just~~ outside the $\theta = \pi/2$ point near the film surface. However, this anomaly could have been due to the approximate surface boundary condition (section 2.3.1) and the coarseness of the grid. A higher-resolution grid might help to understand the problem.

Returning to the other films: while the second derivative of the dependence of bulging on curvature became negative as $1/a_o$ became large, the curves for Q = 1.4, λ/T = 0.462, 0.3465, and 0.231 suggest that it is positive for low curvature. As the wall nears planarity, the bulging approaches zero more slowly.

Within the general form of the graph in Fig. 6.5, for intermediate values of aspect ratio, the bulging varies almost linearly over the limited ranges of bubble stability. Typical slopes were 0.0236 and 0.0382 for the 4635 and 1435 films respectively.

Beyond the stability ranges, it appears that the curves would follow almost parallel paths, converging to the origin, but otherwise displaced vertically by a small amount that depends on the associated material length.

For given values of $1/a_o$, Q and M_s, the bulging increases with decreasing λ/T. This was also predicted by Thiele [50]; the bulging is resisted, as though by a surface tension, by the wall energy. Material length is just a normalized wall energy density. In Fig. 6.5, the effect is clearest for Q = 4.6, where the walls are relatively thin.

6.5 WALL ENERGY DENSITY

The wall structure features previously discussed will obviously influence the important parameter, wall surface energy density. This quantity is useful in domain theories [50,51,6], because its variation gives rise to a wall surface tension, a generalized force tending to minimize total wall area.

We define wall energy density, σ_w, to be

$$\sigma_w = E_w/2\pi\, r_o\, T, \tag{6.7}$$

where r_o is the radius at which $\theta = \pi/2$, averaged over z, and E_w is the total wall energy of the configuration. Thus, E_w is computed, according to the formulation in Ch. 2 and the definitions in Ch. 3, over the volume of the wall region, and then this energy is ascribed to a right cylindrical surface at the mean wall radius.

Normalized to the magnetostatic energy volume density of a saturated film, $\mu_o M_s^2$, the wall energy density becomes a characteristic material length. In Thiele's theory [51], where σ_w is that of a pure Bloch wall, this quantity is further normalized to the film thickness (fixed in the present study). We define the quantity σ_n as an analogue of this normalized material length, the symbol emphasizing the quantity's basis in wall energy (compare to λ^*/T in section 3.3). Thus,

$$\sigma_n = E_w/2\pi\, \mu_o\, M_s^2\, r_o\, T^2. \tag{6.8}$$

In Fig. 6.6 we show the dependence of σ_n on $1/a_o$ for $\lambda/T = 0.231$, Q = 1.4, 2.3, and 4.6. As the wall curvature increased at smaller aspect ratios, the energy density increased

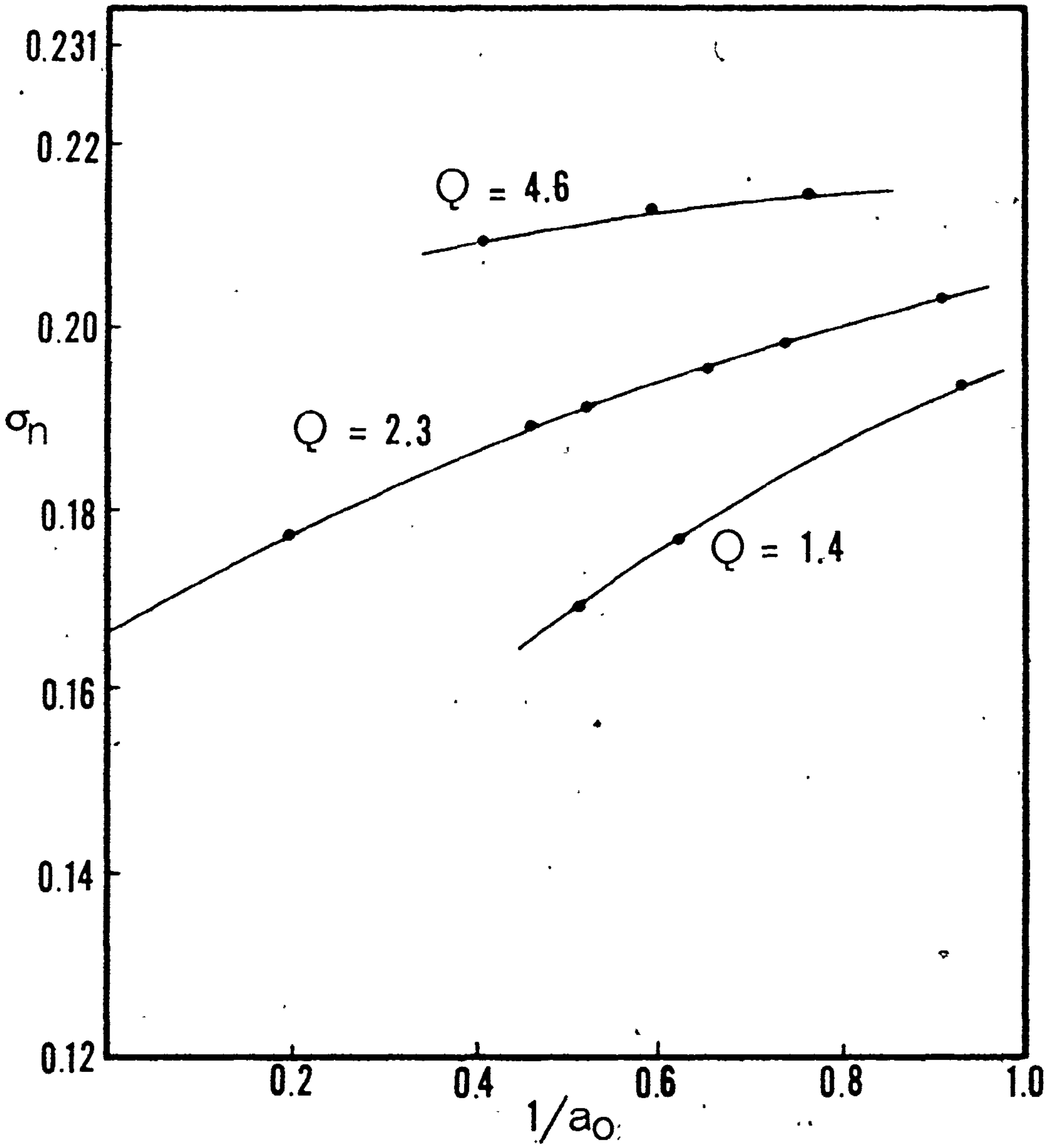

Fig. 6.6 Wall surface energy density normalized to magnetostatic self-energy density, σ_n, vs. $1/a_o$, for λ/T=0.231, Q=1.4, 2.3 and 4.6.

as well. However, all values of σ_n were found to be much less than the nominal normalized material length, 0.231, indicating that the computed wall configuration was relaxed to a lower-energy state than that of a Bloch wall. The energy density for Q = 2.3 was obtained [31] from DeBonte's stripe-wall results [21]; at 0.20, it was also much higher than the comparable large-aspect-ratio value in the figure.

The curves in Fig. 6.6 are second-order polynomials fitted by least squares. The fits are better throughout than the linear regression of [4], especially for the large-a_o point included here for Q = 2.3.

The dependence of σ_n on aspect ratio has significant implications for the static and dynamic properties of bubble domains. The static stability of circular bubbles is investigated in Ch. 7.

In Fig 6.7, we plot all the wall energy density values against $1/a_o$, but normalize to the characteristic Bloch wall energy density in bulk material [17,8]. This quantity,

$$\sigma_A = 4(AK_u)^{\frac{1}{2}}, \tag{6.9}$$

used in Thiele's domain theory [51,9], may be calculated for the films studied here from the data in Table 6.1. Note that, since $\sqrt{A}$ is proportional to M_s^2 for fixed λ/T, the relative variation with $1/a_o$ of the ordinate quantity in Fig. 6.7 is the same as that of $\sigma_w/\mu_o M_s^2 T$ in Fig. 6.6 (which was used in [4,5]).

We see from Fig. 6.7 that (contrary to the situation before normalization) the normalized energy density was lower for

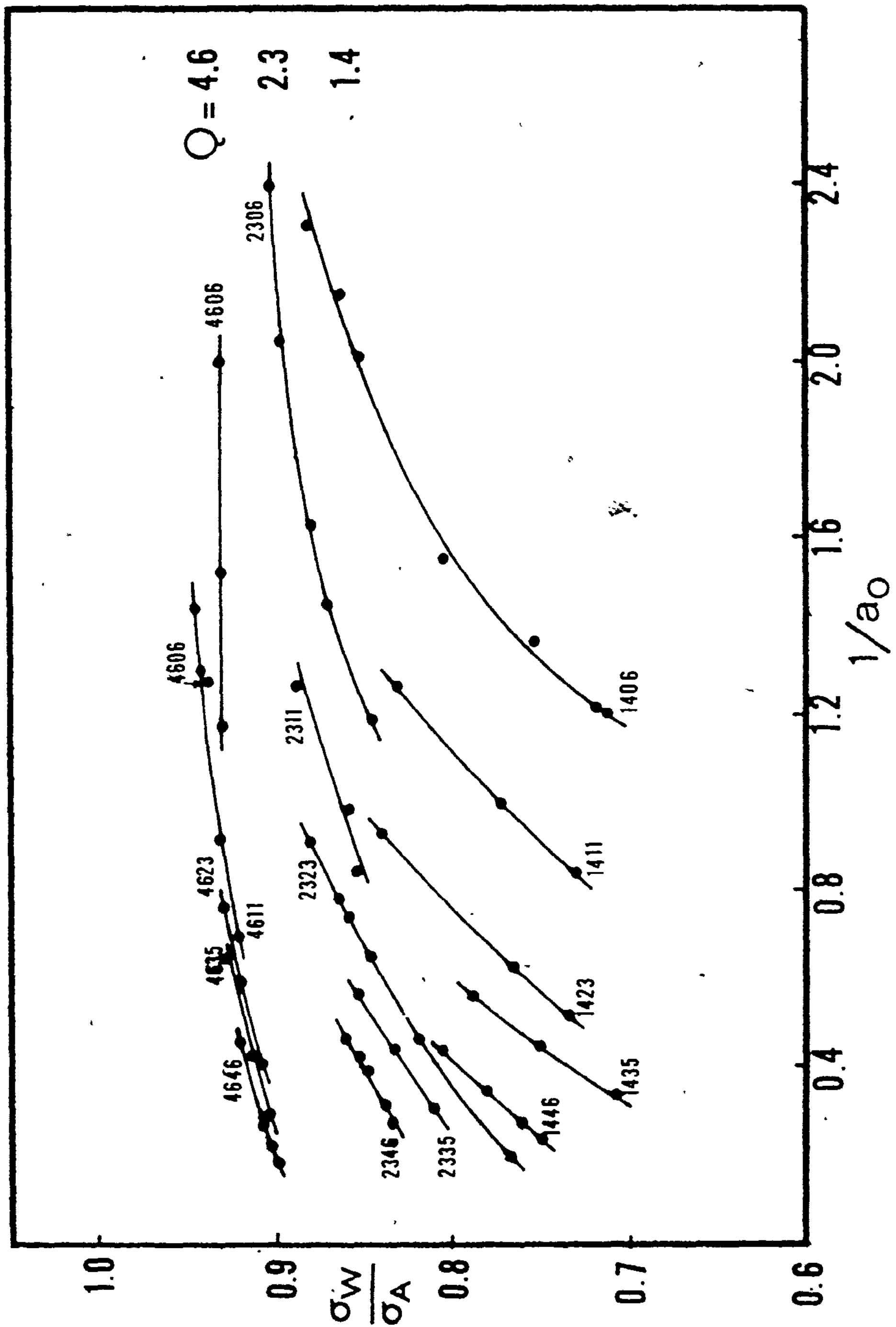

Fig. 6.7 Wall surface energy density normalized to bulk Bloch-wall energy density, σ_w/σ_A, vs. $1/a_o$, for all bubbles.

the lower-Q materials. In any case, the dependence on aspect ratio was stronger for low-Q (high-M_s) materials, as it was for wall width flaring (Fig. 6.1).

We also note that for a given Q, increasing λ/T shifts the normalized wall energy upward, although the wall curvature decreases and aspect ratio increases. M_s is fixed at a given Q, and the increase in A (as $(\lambda/T)^2$) should be normalized out. To be sure, in the respective ranges of bubble stability, the average σ_w/σ_A is about the same for all λ/T, while the range of σ_A is determined (in this work) by M_s (i.e., Q). The exchange interaction (A) broadens the whole wall in order to reduce its exchange energy to some extent.

The reconfiguration of the wall structure, during the computational relaxation, reduces the magnetostatic energy density that arises from the proximity of film surfaces. However, at a given M_s, the energies from bias field and demagnetizing fields were not strong functions of the width of the wall region.

The uniaxial anisotropy energy, of course, did increase strongly with the wall region width, so it and the insufficiently reduced exchange energy dominated the magnetostatic energy. This is an assumption of high-Q theories [37, p. 3]; however, we see from Fig. 6.7 that for Q = 4.6, the wall energy density is only about 0.93 of the bulk Bloch-wall value, σ_A, and at Q=2.3, near the lower limit of Q usable in devices, the ratio is only about 0.86. At values in a region of interest to certain uniaxial magnetic film measurements, Q = 1.4, the ratio σ_w/σ_A may be 0.75 or less.

CHAPTER 7

DOMAIN STABILITY

7.1 INTRODUCTION

In this chapter, we explain how the stability limits were determined in this work, and we present data to describe the margins of bubbles in the films studied. An important aspect of this treatment is that while Thiele's analysis [51,9] commonly used in magnetic bubble technology, effectively assumes infinite Q and thin Bloch-energy walls, the present results will predict Q-dependent stability margins.

As was described in Chapter 1, the stability of bubble domains may be considered in the following terms. The collapse point, or "margin", is characterized by a minimum radius or aspect ratio and a maximum bias field, beyond which the bubble shrinks irreversibly (unless the bias field is reduced early in the collapse) and disappears. The runout, or stripe-out, point is defined in a complementary way.

Limits of stability against collapse and stripe-out depend in part on wall surface energy density (section 1.3.1), and wall energy density depends on aspect ratio (section 6.5). Therefore, a stability limit can be accurately measured theoretically only by locating the aspect ratio at which the computed (or predicted) wall energy density yields the stability criteria for the total energy derivatives. Since in a given film there is a one-to-one correspondence between bubble aspect ratio and bias field (neglecting coercivity), the same procedure can be used to produce the stability limits for the bias field.

7.2 THEORETICAL ANALYSIS OF STABILITY LIMITS

After the modelling algorithm has converged, the wall energy density σ_w, as defined in Ch. 3, can be computed and substituted into the Thiele analysis [51,9] in place of the material Bloch wall energy density, σ_A. This will result in improved predictions for the collapse and stripe-out limits. In section 7.2.1, we discuss this method with respect to the stripe-out limits. For the collapse limits, however, a more specific method was formulated, and it will be described in section 7.2.2.

7.2.1 Stripe-Out Limits.

Bubbles were modelled at several bias fields for the same film, and a graph was plotted of the bias field (aspect ratio) on the abscissa versus the difference between the bias field (aspect ratio) and the predicted [31] Thiele stripe-out field (aspect ratio) on the ordinate. (This ordinate quantity was chosen because the present model does not give direct information on a non-axisymmetric instability such as stripe-out.) The stripe-out limit was obtained by extrapolating the resulting curve to the abscissa intercept. In this work, the curves were very close to straight, so the points were least-squares-fitted by straight lines.

As an example, Fig. 7.1 shows the graph for the stripe-

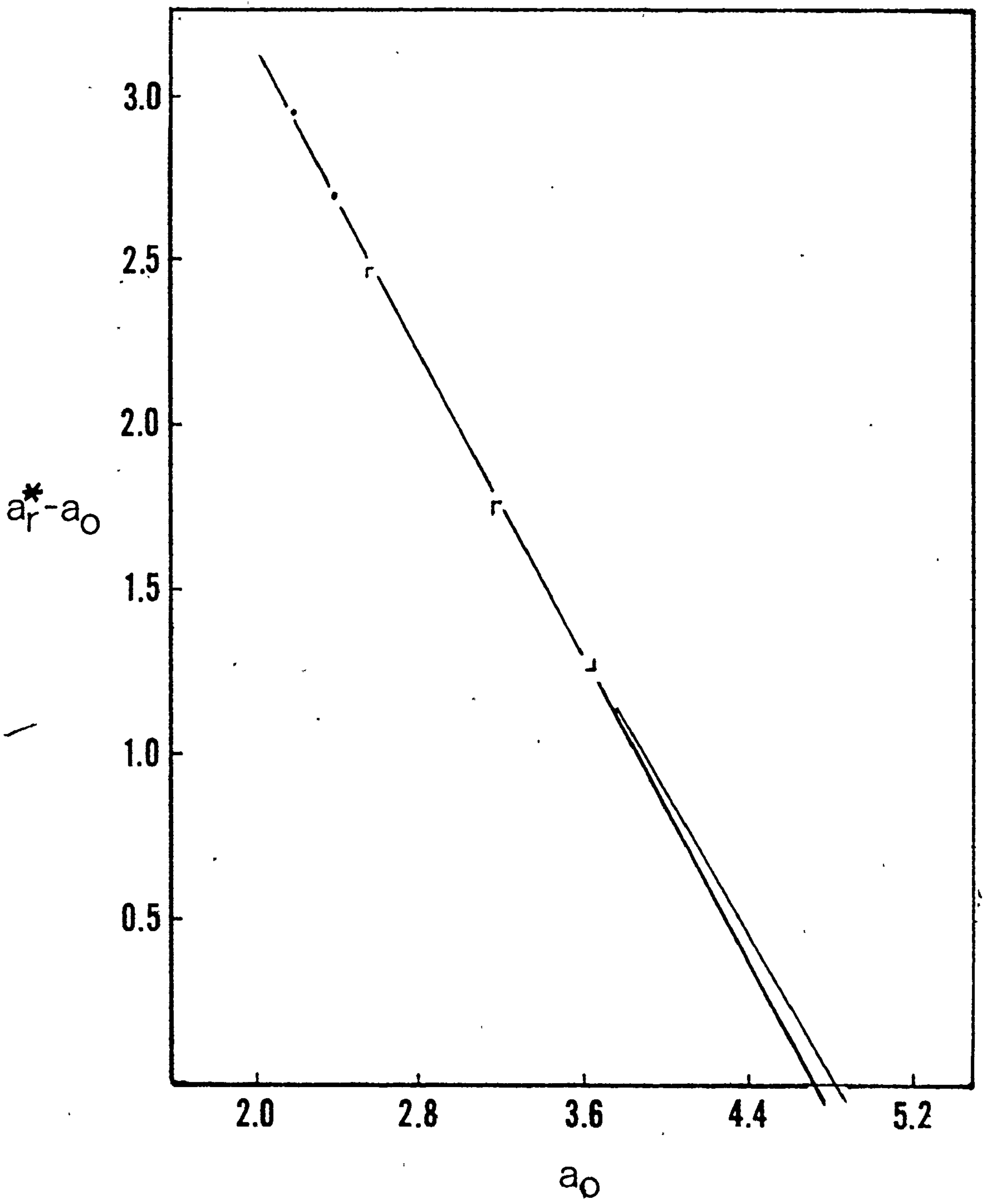

Fig. 7.1 Aspect ratio a_o vs. "distance" to stripeout, $a_r^*-a_o$, for Q=2.3, $\lambda/T=0.462$.

out aspect ratio of a film having $\lambda/T = 0.462$, $Q = 2.3$. This graph was chosen for the figure because the points appeared to fall on a line of greater than usual curvature, small though the curvature is. The "error" bars indicate the change in radius being called for by the algorithm of Ch. 3 when the convergence criterion (section 4.3) was reached.

The intercept uncertainty estimates were taken to be twice the difference between the value of the actual intercept and of the intercept of the linear extrapolation from the two nearest data points of positive ordinate. This uncertainty shows clearly in Fig. 7.1. Such a definition allows for the possibility that the true line through the data points is slightly curved.

Of course, the resulting stripe-out field should be consistent with the corresponding stripe-out limit aspect ratio; that is, the modelling algorithm would be expected to produce a bubble of that aspect ratio for a bias field equal to that stripe-out field. The graphs from which the data of section 7.3.2 were obtained indicated that this was indeed the case.

7.2.2 Collapse Limits.

The collapse bias field is an important measurable quantity, used in the determination of bubble film magnetic parameters [25,31,7]. Fortunately, the radius-calculation algorithm in this work leads to a straightforward analysis of stability against collapse. In contrast to stripe-out, bubble collapse is an axisymmetric instability and can be treated directly within our model.

The method used to determine H_c, the bias field at collapse, will be described first. The corresponding procedure for the determination of the corresponding aspect ratio, a_c, will then be discussed.

Since the derivative of the bubble's total energy is approximated by a quadratic polynomial (section 3.1.1),

$$\frac{\partial E_t}{\partial a} = c_0 + c_1 a + c_2 a^2, \qquad (7.1)$$

the energy itself, $E_t(a)$, has the functional form of a cubic polynomial. This is in agreement with [35,37 p. 20,15]; for stable radii there is a potential-energy wall preventing bubble expansion and a relatively low potential barrier preventing collapse to zero radius.

The three-part Fig. 7.2 illustrates schematically the situation near collapse. In Fig. 7.2(a) we see that, for $H_B<H_c$, the roots of the quadratic polynomial for $\partial E_t/\partial a$ occur at stable and metastable equilibria, depending on the sign of the second derivative. From the familiar formula for the roots of a quadratic, the discriminant between the roots is

$$D_q = \frac{1}{2c_2} (c_1^2 - 4 c_2 c_0)^{\frac{1}{2}}. \qquad (7.2)$$

As the bias field increases, the roots move closer together until they meet when $H_B = H_c$, in Fig. 7.2(b). At this bias field, the discriminant vanishes and the energy function has a critical point of metastability at a_c.

At bias fields beyond collapse, depicted in Fig. 7.2(c), the roots of the quadratic are imaginary, so D_q^2 is negative. The

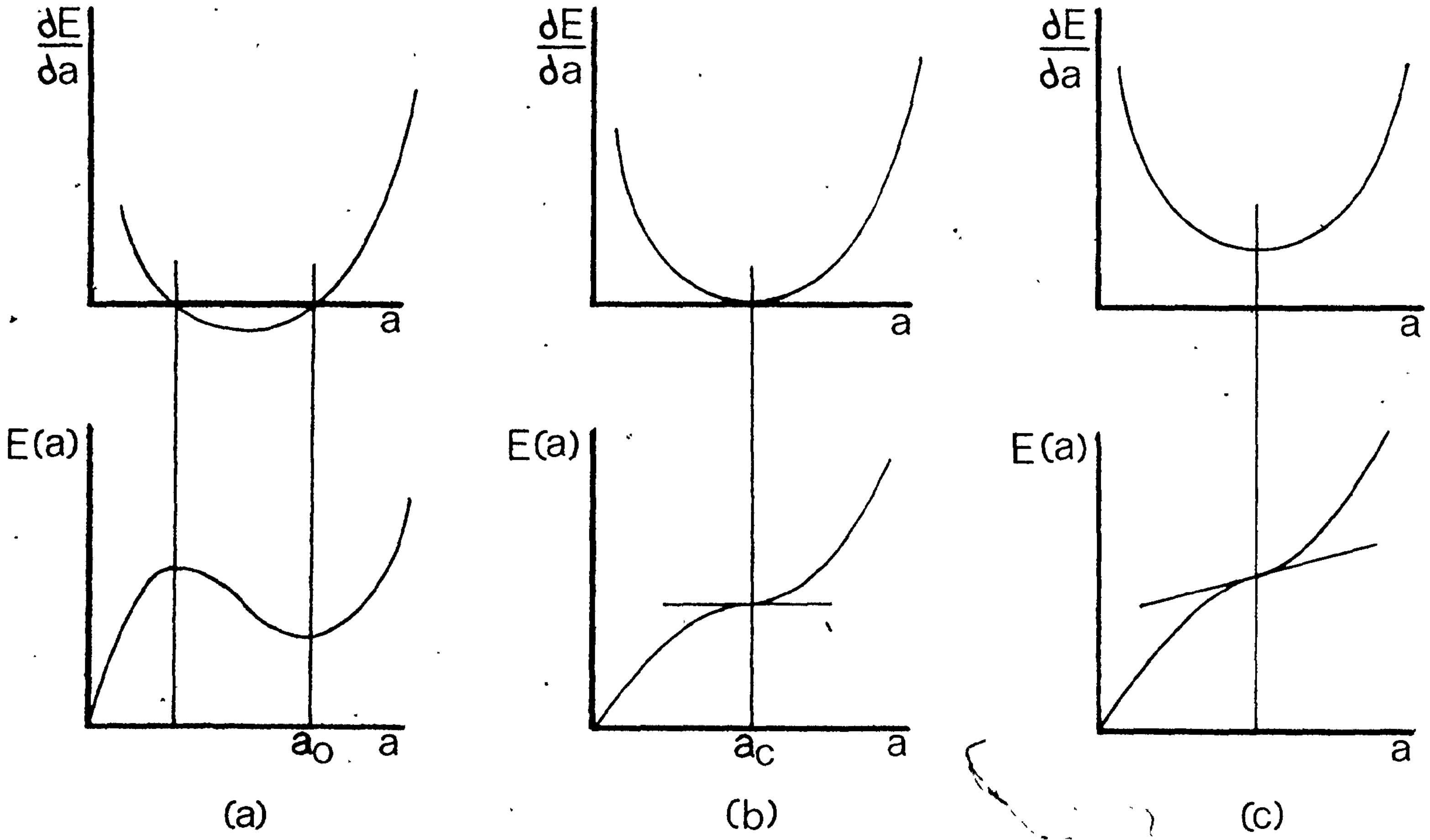

Fig. 7.2 Functional forms of $E_t(a)$ and $\partial E_t/\partial a$ near bubble collapse, a_c; schematic.

energy function has no local minimum: the bubble will shrink until it disappears.

Thus, the collapse point coincides with the intercept, at $D_q^2 = 0$, of the graph of D_q^2 vs. H_B. Bubbles were modelled at several different bias fields for each film and the curves of D_q^2 vs. $h_B = H_B/M_s$ were extrapolated to the abscissa to locate the (normalized) collapse field, $h_c = H_c/M_s$.

An example of a family of typical graphs, for $\lambda/T=0.3465$, Q=1.4, 2.3, and 4.6, is Fig. 7.3. The curves were drawn with a French curve; drawing families of nearby curves together allowed information from each curve to help ascertain the form of adjacent ones. The nature of the extrapolation was further clarified by the existence of some points very near collapse. The curves were drawn and extrapolated in this way after second-order Lagrangian fits had been tried and produced parabolas which for some films had improbable intercepts or none at all.

An estimate of the uncertainty in the value of an intercept was taken to be the difference between that value and the value of the intercept of the linear extrapolation from the two nearest data points.

Similar graphs having aspect ratio on the abscissa produced intercepts at shallow angles and were impossible to interpolate accurately. A typical example is shown in Fig. 7.4, which contains the curves drawn for $\lambda/T=0.3465$, Q=1.4, 2.3, and 4.6. The value of an intercept clearly depends on the somewhat arbitrary way the curve is drawn.

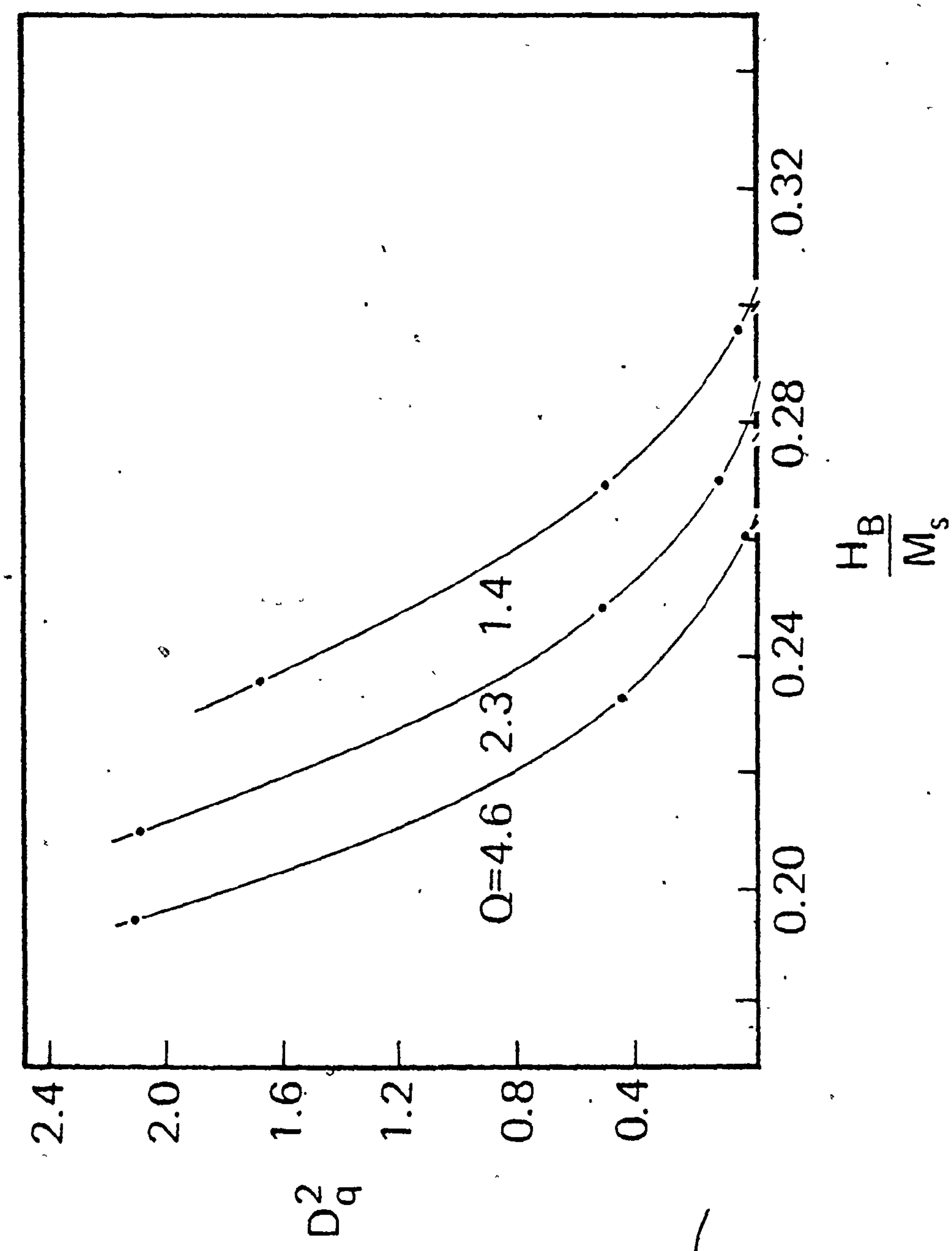

Fig. 7.3 Square of discriminant versus bias field; extrapolation to abscissa determines collapse field. $\lambda/T=0.3465$.

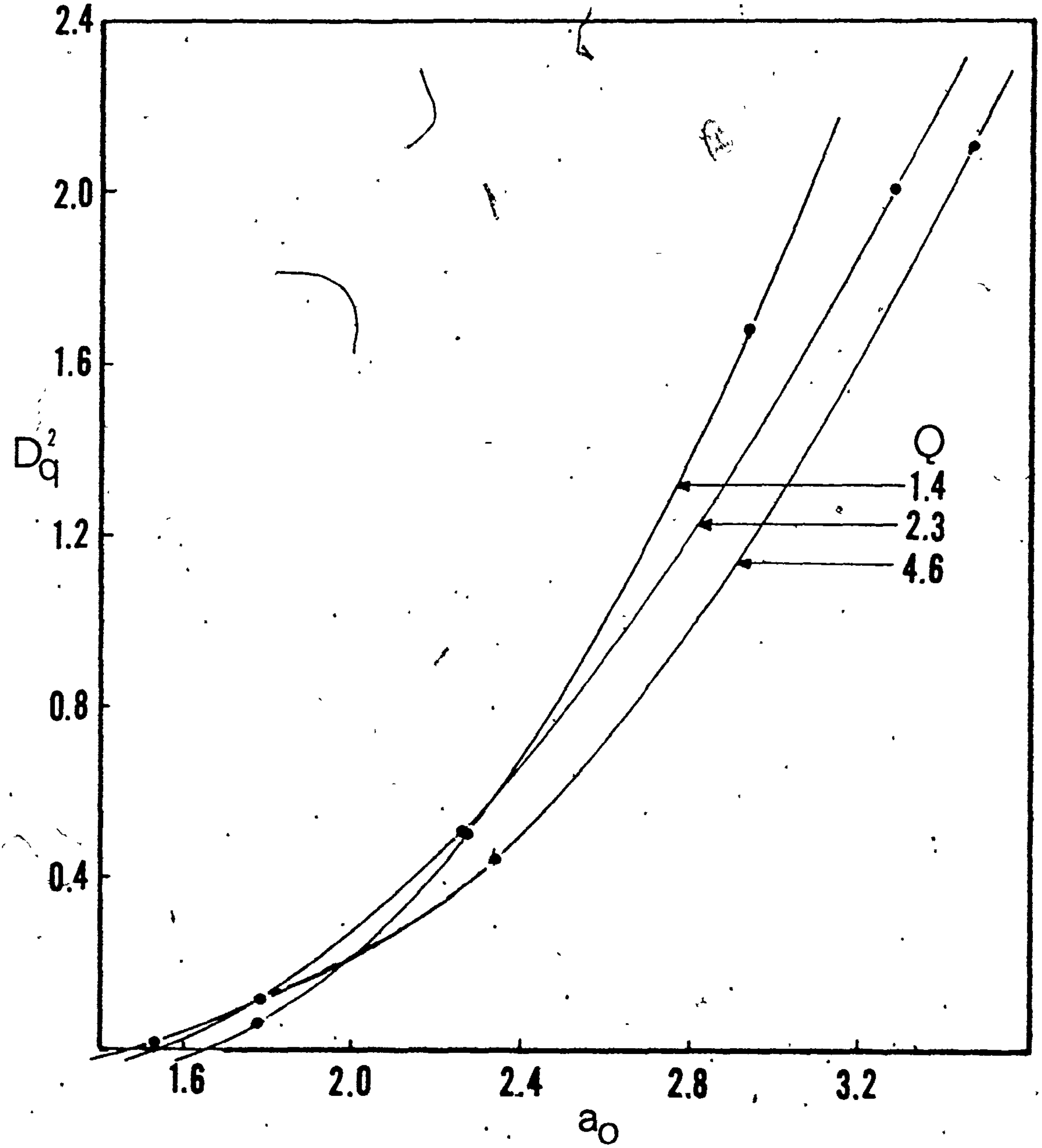

Fig. 7.4 Square of discriminant versus aspect ratio; extrapolation to abscissa determines collapse aspect ratio. $\lambda/T=0.3465$.

In an attempt to find a more precise method, graphs were plotted of a_o against $(H_c-H_B)/M_s$, where H_c had been found by the method of Fig. 7.3. The intercepts were often even shallower, as might be expected from Thiele's prediction [51] that at collapse, $\partial a_o/\partial H_B=0$. The present results reinforce this prediction.

The collapse radius is also found experimentally to be an ill-defined quantity. It appears that our model is realistic enough to reproduce this unfortunate behavior. Therefore, the results related to collapse aspect ratios, which were calculated by the method of Fig. 7.4 and are presented in section 7.3.2, are to be regarded as only approximate.

7.3 RESULTS OF THE DOMAIN STABILITY ANALYSIS

7.3.1 Collapse Field, H_c.

The collapse field will be considered separately because it is easily measured experimentally and it is useful in the characterization of bubble films' magnetic properties.

Experimentally, the static behavior of bubble domains is characterized [7] by the film thickness T, the saturation magnetization M_s, the nondimensional anisotropy coefficient $Q = 2K_u/\mu_o M_s^2$, and the material length $\lambda = 4\sqrt{AK_u}/\mu_o M_s^2$. The thickness is measured by optical interference, but the other parameters, M_s, Q, and λ are usually not measured directly.

In a common technique described by Fowlis and Copeland [25] following Thiele's theory [51], the material parameters other than Q are calculated from measurements of film thickness, zero-bias periodic stripe width, and the bubble collapse field H_c. Thus, Q is neglected; it may be added to the set of parameters by measuring also the difference between anisotropy field and magnetization,

$$H_K^* = H_K - M_s = (Q-1)\,\mu_o\,M_s. \tag{7.3}$$

The purpose of this section is to present results of our model regarding the dependence of H_c on ~~material~~ parameters. We will assume the "true" value of material length has somehow been found; in fact, its determination from stripe-width measurements is also Q-dependent. The formulation of the entire analysis, from the set of four measured quantities through a self-consistent calculation to the four material parameters, is the subject of [7].

Experimental values for collapse and stripe-out bias fields and aspect ratios can be obtained from Almasi [2] for $\lambda/T=0.231$. However, the present results are based on the assumption that λ/T and M_s were determined by an accurate, Q-dependent method [7], and the film studied in [2] was not measured by such a method. In fact, Q was not given in [2]. For these two reasons, agreement between our results and the stability limits quoted in [2] cannot be expected.

Each value of λ/T is associated, by Thiele's theory [51,9], with a single Q-independent collapse field, H_c'. We define a quantity H_{Cc} to be our predicted relative correction to the collapse field obtained from Thiele's theory. This correction is a function of Q as well as of λ/T. Therefore, the set of modelling runs produced a relative correction for each different Q,

$$H_{Cc}(Q,\lambda/T) = (H_c - H_c') \,/\, H_c'. \tag{7.4}$$

This quantity was plotted in Fig. 7.5.

Trial functions $H_{Cc}(Q,\lambda/T)$ were fitted to the data in the least-squares sense. The curves of H_{Cc} versus $\sqrt{\lambda/T}$ suggested the familiar Bloch wall profile function, which required two coefficients to specify its position in the $(Q,\lambda/T)$ plane, and two more to specify its width and height. (The two low-λ/T points for $Q=4.6$ were smoothed slightly, but kept well within their uncertainty limits.)

After the coefficients were determined and found to be monotonic in Q, they were fitted to linear functions in different powers of Q. The form of the final expression was adjusted to give it suitable properties of extrapolation to large and small values of Q and λ/T. The result was

$$H_{Cc} = q_1 \tan^{-1} \exp(q_2\sqrt{\lambda/T} - q_3) + e^{q_4} \tag{7.5}$$

where $q_1 = -0.133 + 0.442\, Q^{-1/2}$

$q_2 = 9.811 - 3.373\, Q^{-1.4}$

$q_3 = 5.649 - 2.072\, Q^{-4/3}$

$q_4 = -4.121 - 0.0011\, Q^4$.

This formula was used to produce the family of curves in Fig. 7.5. It may be noted from this graph that if the true λ/T is known, the correction made by the micromagnetic bubble model to the prediction, by Thiele's theory, of the collapse field are substantial. For $\lambda/T > 0.4$, the correction would approach 10%

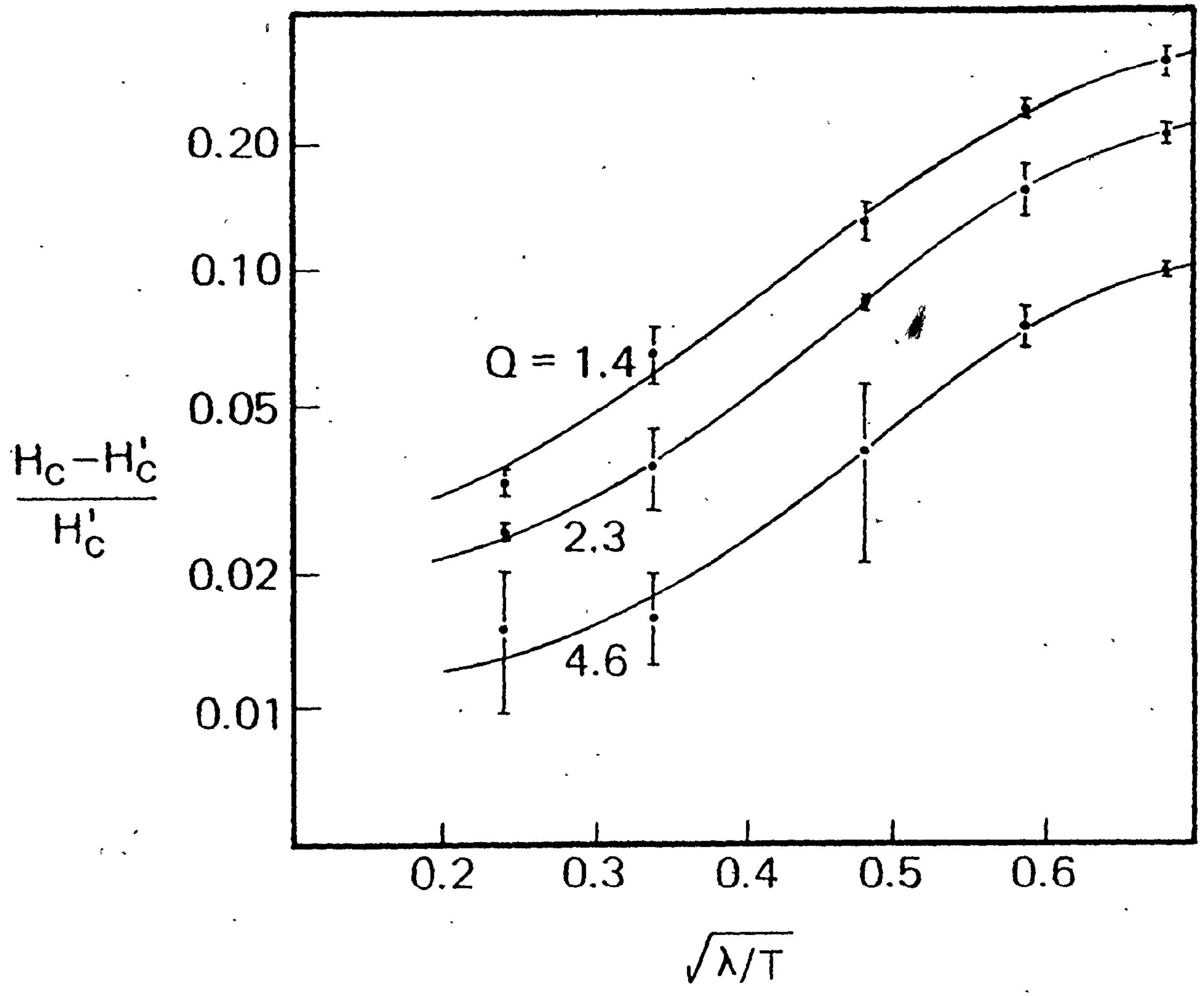

Fig. 7.5 Relative correction of Thiele-theory collapse field versus $\sqrt{\lambda/T}$, with fitted curves.

even for large Q near 4.6, while for small Q near 2.3, the correction approaches 20%. For $Q \cong 1.4$, near the minimum value consistent with the stability of bubbles, the correction would be nearly 30%.

In Fig. 7.6, the actual collapse fields, calculated according to section 7.2.2 and Fig. 7.3, are plotted against normalized material length, λ/T. For comparison, the curve of Thiele-theory collapse field, H_c'/M_s, versus λ/T is included. The curves through the data points were obtained by adding the curves of Fig. 7.5 to this H_c'/M_s curve.

If the values of λ/T, 0.231, and M_s, 443.6 Oe, of the film studied in [2] were accepted, the collapse field for that film would lie on the Thiele-theory H_c'/M_s curve. Of course, this suggests that the Fowlis-Copeland method [25] was used in [2] to determine M_s from the collapse-field measurement.

7.3.2 Other Stability Limits.

The stripe-out fields, found by the method described in section 7.2.1, are plotted as functions of λ/T in Fig. 7.7. This graph has a form similar to that for collapse field, Fig. 7.6. In this case, the curves through the data points were drawn manually; no function-fitting was carried out.

The runout field is not accurately measurable experimentally and is not commonly used in material characterization. For comparison, the "experimental" point of Almasi [2] is included as though its associated λ/T and M_s were reliable (see section 7.3.1). Since its Q is unknown as well, the closeness of agreement can not

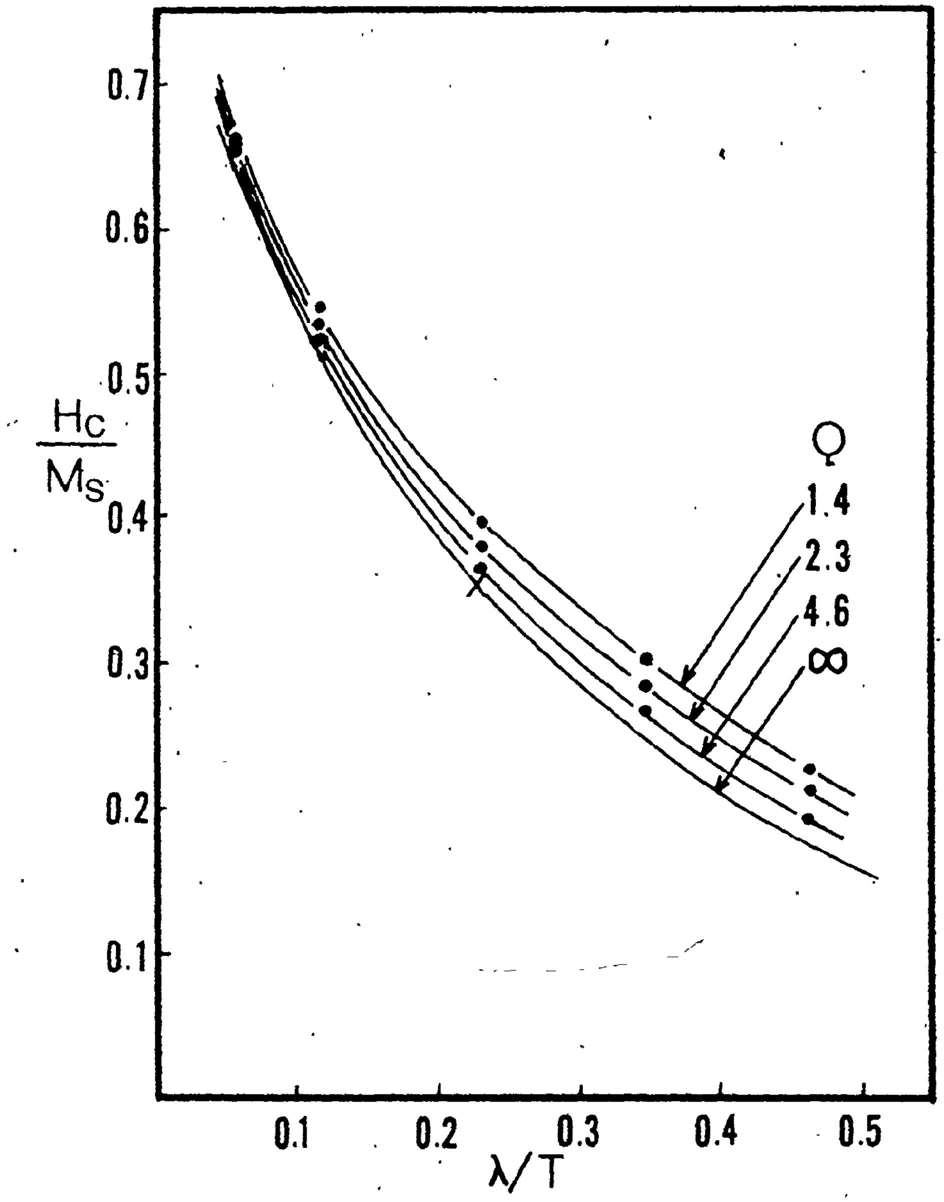

Fig. 7.6 Normalized collapse field versus normalized material length, with fitted curves.

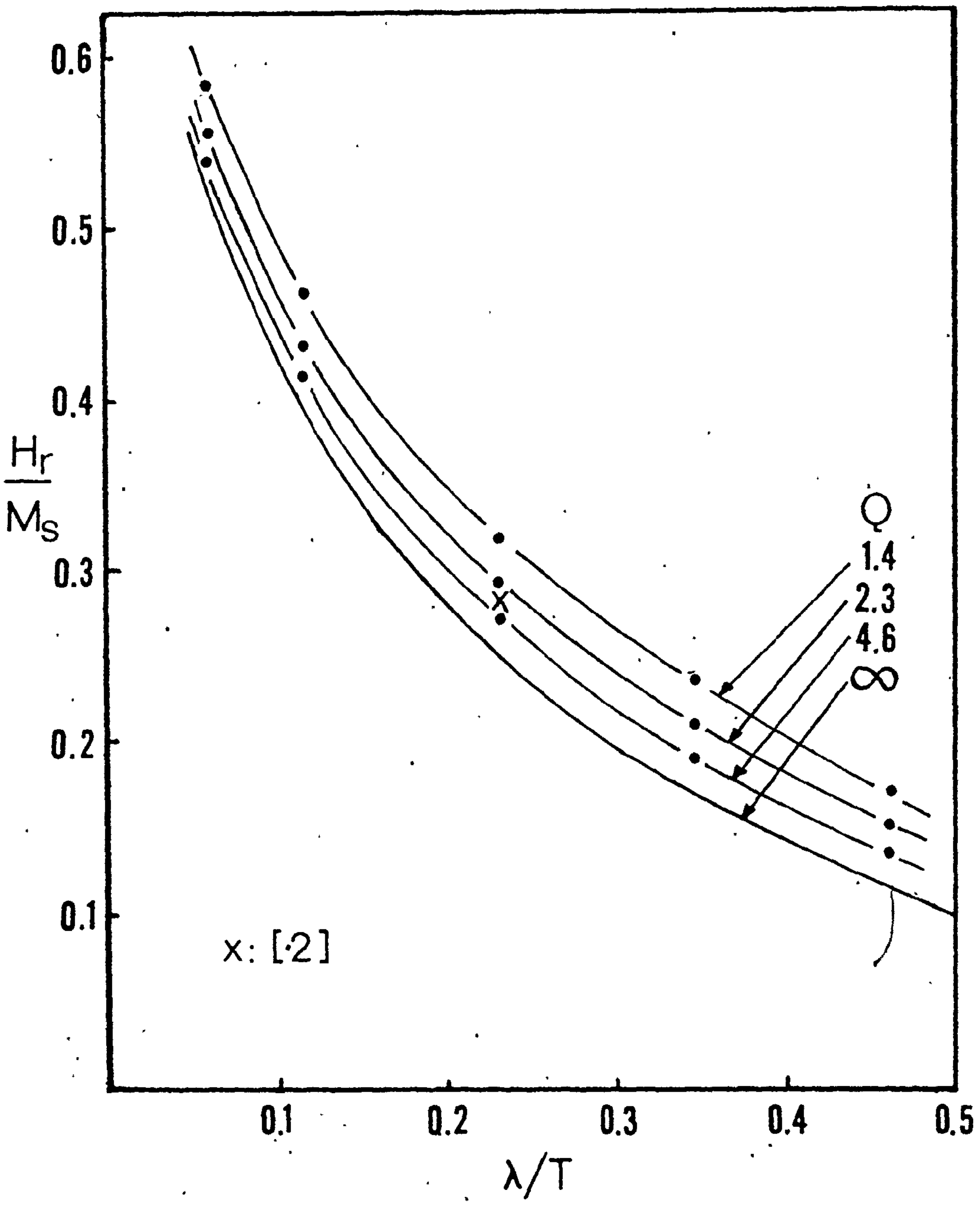

Fig. 7.7 Normalized stripeout field versus normalized material length.

be judged.

A quantity of interest in magnetic bubble technology is the relative bias margin,

$$\frac{\Delta H}{H_B} = \frac{H_c - H_r}{(H_c + H_r)/2} \tag{7.6}$$

which is plotted, in Fig. 7.8, as a function of λ/T with Q (therefore M_s) as a parameter. The prediction of Thiele's Q=∞ analysis [51] is included for comparison. For clarity, only half of each derived uncertainty bar is shown. The curves were drawn through the uncertainty bars. Bearing in mind the caveats of section 7.3.1, the experimental point from [2] was added.

There is qualitative agreement with the Thiele domain theory, which predicts larger bias margins than does our finite-Q treatment. The relative margins are seen to decrease with decreasing Q (increasing M_s), for fixed λ/T.

In Fig. 7.9 we present the results obtained for stripe-out and collapse aspect ratios as functions of λ/T. The stripe-out aspect ratio determinations were well-behaved and the points appear to fall on smooth, parallel curves. On the other hand, the collapse diameter is ill-defined, experimentally and in the present model, and there is a substantial amount of scatter in the data points for the lower values of Q.

The experimental points from [2] are included, and there is disagreement, as expected (see section 7.3.1). In this case, part of the discrepancy could be due to a larger-than-expected Q of the experimental material. The discrepancy would also be

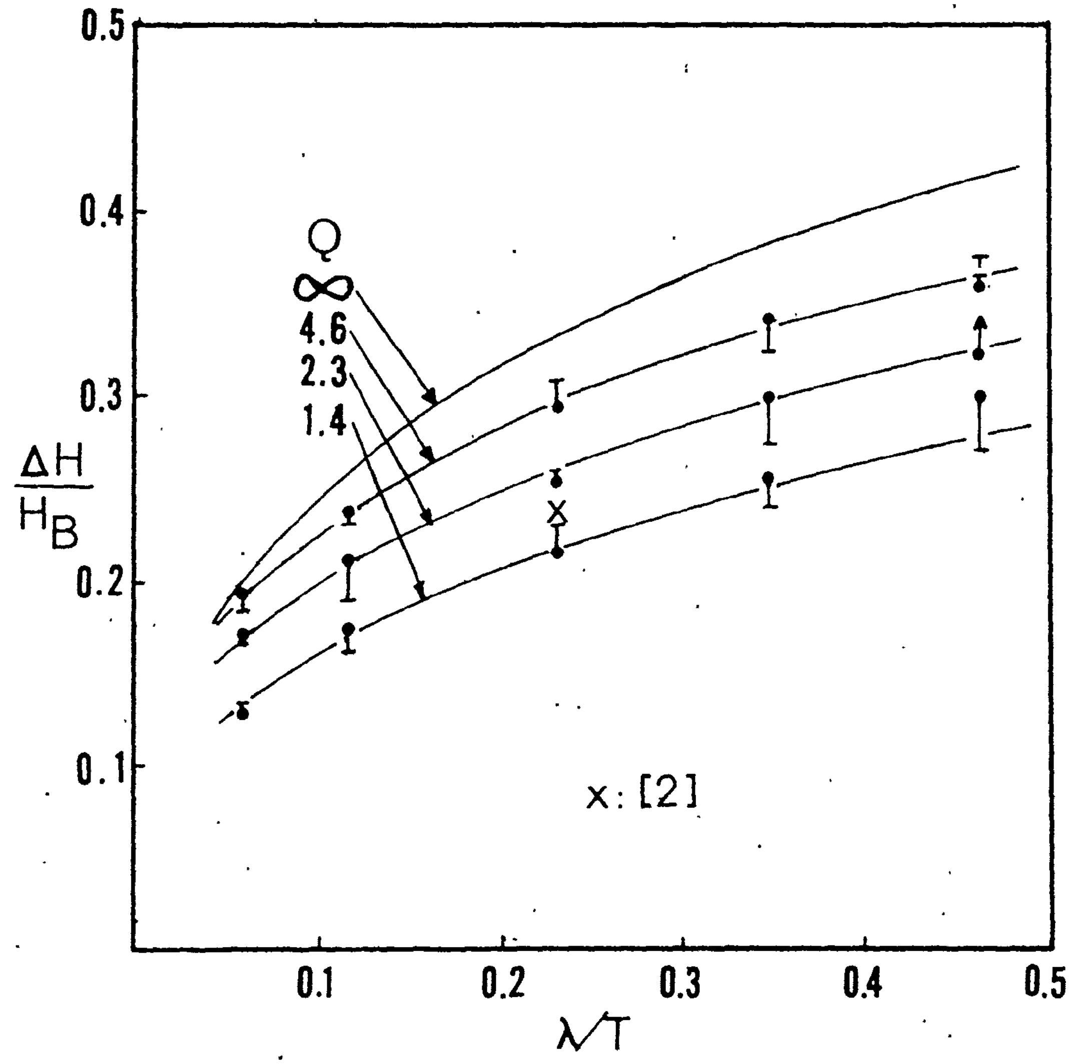

Fig. 7.8 Relative width of bias field stability region, $\Delta H/H_B$, versus normalized material length.

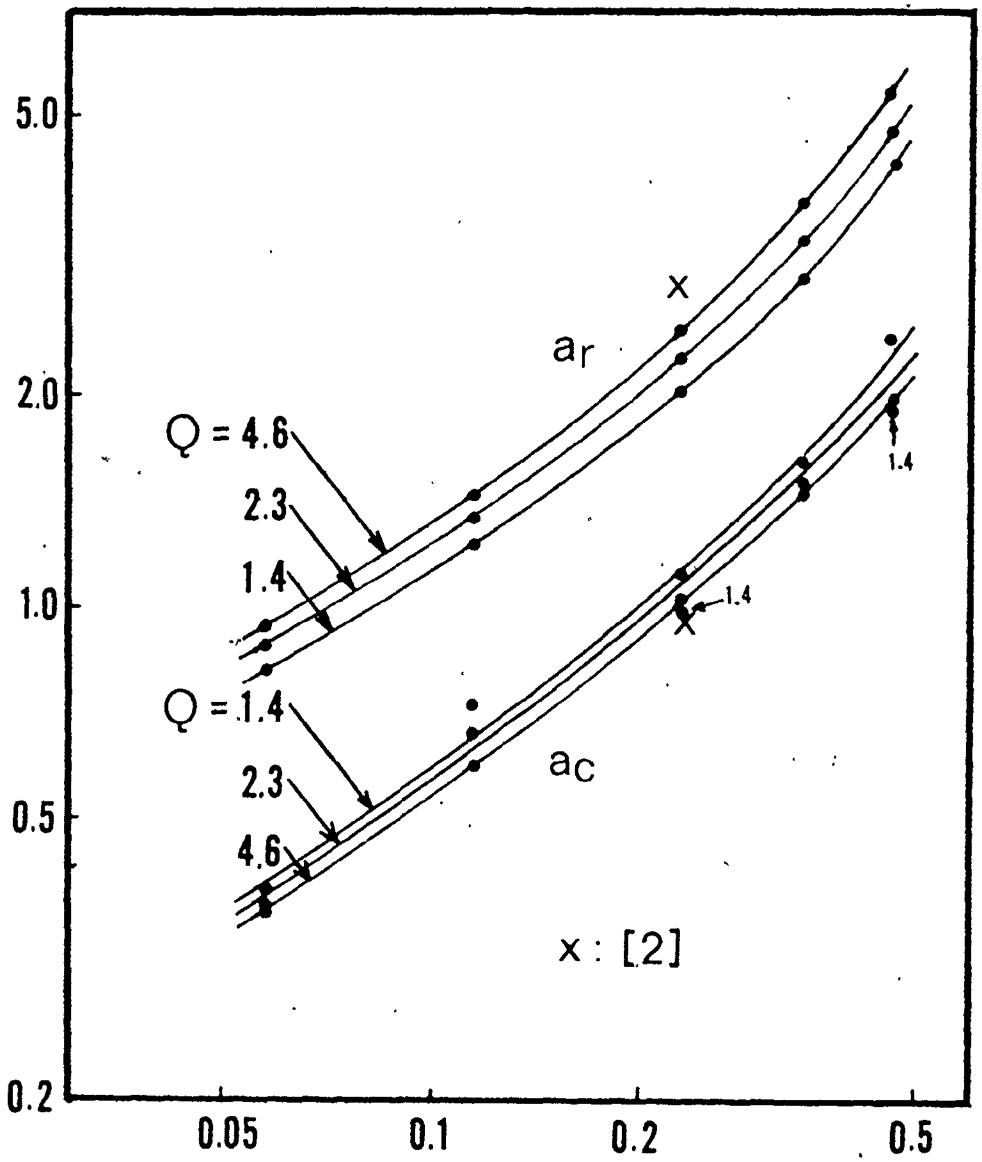

Fig. 7.9 Aspect ratios at collapse and stripe-out versus normalized material length.

in the direction observed if stripe-out and collapse were being resisted by coercivity, which is not included in our model.

Thiele [51,9] has presented a graph of the stability limits of bubble size as a function of film thickness, both normalized to material length. For comparison, in Fig. 7.10 we add to this graph our Q-dependent results. Of course, film thickness T was fixed in the present work, and it was material length λ that was varied.

The results for stripe-out are well-behaved and follow the Thiele-theory curve. This might be expected, since the stripe-out aspect ratios were obtained (section 7.2.1) by means of close linear fits to points calculated [27] from that theory, using the computed grid-wall energies.

The scatter in the collapse aspect ratios at low Q is carried over to Fig. 7.10. However, it can be said from a comparison of the manually drawn curves to the Thiele-theory curve that the prediction of a sudden rise for large λ/T is not supported by the present results.

Another indication of magnetic bubbles' performance in memory devices is the ratio of stripe-out to collapse diameters. This is plotted, in Fig. 7.11, as a function of reciprocal normalized material length, T/λ, after Thiele [51,9]. The curves were drawn to pass smoothly through the data points. (The point for the film having Q=2.3 and T/λ=4.32 seems to be inconsistent with the other data; the reasons for such anomalies as this will

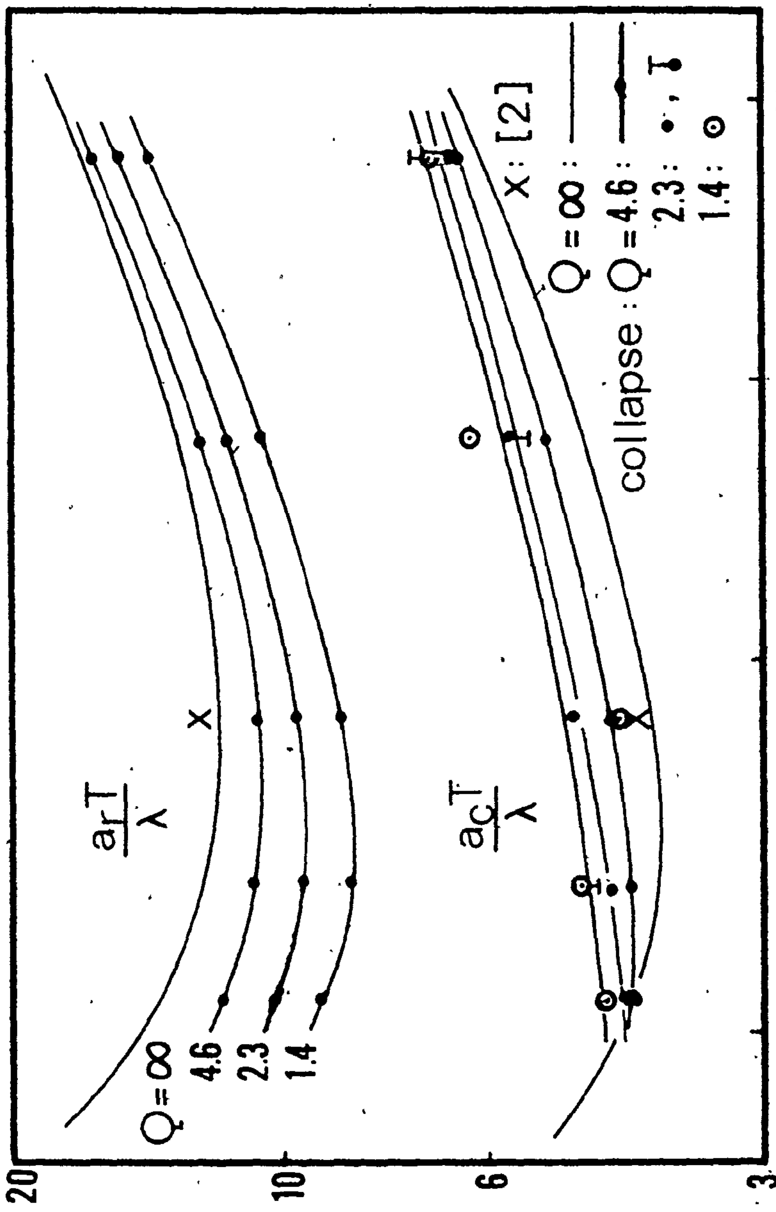

Fig. 7.10 Bubble diameters at collapse and stripe-out versus film thickness T, all normalized to material length, λ.

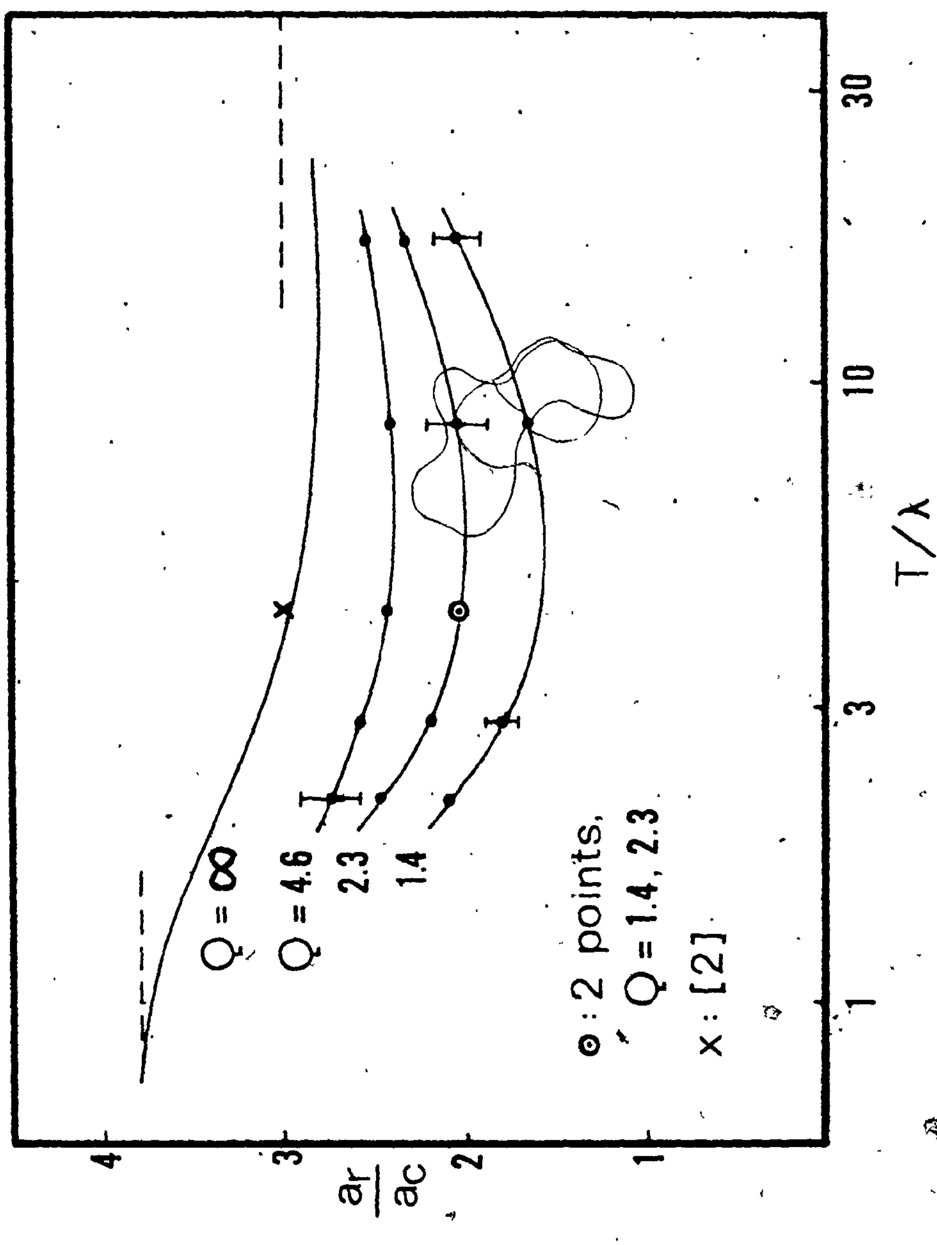

Fig. 7.11 Ratio of stripe-out to collapse diameters, a_r/a_c, versus normalized film thickness.

be discussed in Chapter 8.)

In the figure it is seen that the range of stable bubble aspect ratios decreases with decreasing Q, more so at smaller values of Q. Although the uncertainties in a_c produce large bars on the data points, it appears that the minimum in a_r/a_c, predicted by Thiele, is more pronounced at lower Q.

CHAPTER 8

CONCLUSIONS

In this work, we have presented an algorithm comprising the merger of an axisymmetric-wall micromagnetic model with a thin-film magnetic domain model. The derivation of the domain model was given, and the considerations involved in the interactions between the two analyses of different kinds were analyzed.

The composite algorithm was found to seek minimum-energy configurations of magnetic bubble size and wall structure with reasonable efficiency. It is believed to be powerful enough to successfully model bubbles in all films that will be found experimentally to support bubbles.

In this present work, studies were carried out for wide ranges of material parameters, and quantitative results were presented. Notably, structural parameters of the axisymmetric walls were studied as functions of domain radius. Previous two-dimensional micromagnetic analyses [43,29,34] have studied plane walls.

In general, it was found that many of the approximations of variables-separable and high-Q theories are inaccurate. There was strong and complex dependence of θ on z (flaring, bulging) as well as on r, and of ϕ on r as well as on z. Also, of interest in domain theories, at moderately low Q, wall surface energy densities are significantly less than the bulk Bloch wall value, $4\sqrt{AK_u}$.

However, the value of the physical insights and ease of computation associated with more approximate and simplified treatments must be recognized.

A dual scan of film material parameters was performed, and relationships between different films in terms of trends in wall structure quantities were observed. Specific results in this area were noted in Chapter 6.

Also investigated were the ranges of stability of the bubble domains for the aforementioned film parameters. Approximate agreement with limited experimental data was found, but stability predictions were not directly comparable to experiment for reasons stated in section 7.3.1: the derivation of material parameters from magnetic measurements must take into account the Q-dependence of domain properties. In particular, this must be done in the derivation of material length from stripe-width measurements [7], which is outside the realm of the present cylindrical-domain model.

Of course, the numerical results of the present algorithm were not absolutely precise. The uncertainty was not so much due to round-off (thirteen digit arithmetic was used) or truncation error (the convergence criterion was very small), as it was to the discrete nature of the grid adjustments. If a criterion was met for the alteration of the wall configuration radius, then a substantial change was made; and the test was made only periodically. This policy was necessitated by the inevitable limitation on computation time. A change in the grid radius or width requires a recalculation of all the demagnetization factors, which takes a time equal to that of many wall relaxation iterations.

Such a source of error is inherent in a numerical model of this kind. It can theoretically be made arbitrarily small (above computational arithmetic error) by tolerating a large enough computation time.

From the work of this thesis there emerge a number of possibilities for further investigation and for directions of future research.

The data recorded for the bubbles modelled here could be studied in more detail. For example, the various contributions to wall energy - anisotropy, exchange, and especially, demagnetizing field - could be analyzed in terms of their variations with bubble aspect ratio and material parameters, separately and relative to each other (see section 6.5).

Without further development of the algorithm, bubbles could be modelled for sets of material parameters chosen differently, to study each specifically in its effects on wall structure. For example, the exchange coefficient A could be held constant; Q could be varied by changing K_u and keeping M_s fixed; or film thickness T alone could be varied.

A simple addition to the computer program would allow a study of the distributions of energy contributions among the different regions of the wall.

The dynamic properties of axisymmetric bubble walls could be investigated if the energy-relaxation algorithm were replaced by a Landau-Lifshitz-Gilbert torque formulation [43]. The motion of horizontal Bloch lines could be observed, more generally if the symmetry about the film midplane were removed [44]. Dynamic properties could be further characterized by means of gyrovector maps of the wall and measurements on them [5,52].

The treatment of wall structure periodic in α (e.g., vertical Bloch lines) would be a more fundamental extension, but the mathematics could be included under the present structure of the overall algorithm.

The data presented here or acquired in future could be used in the development of analytical models which would explain the relationships between wall bulging, flaring, and twisting on domain and wall region aspect ratios.

Other questions have been raised in the course of the discussions in Chapters 5 and 6. There is clearly no shortage of problems yet to be resolved in the subject of magnetic domain wall structure and its relationship to domain properties.

APPENDIX

EXCHANGE ENERGY FROM AXISYMMETRIC MAGNETIZATION

The α-variation term in the exchange field calculation (section 2.2.4) must be treated separately, as follows:

$$\frac{1}{r^2}\frac{\partial^2}{\partial\alpha^2}\vec{M} = \frac{1}{r^2}\left[M_r\frac{\partial^2}{\partial\alpha^2}\hat{r} + M_\alpha\frac{\partial^2}{\partial\alpha^2}\hat{\alpha} + M_z\frac{\partial^2}{\partial\alpha^2}\hat{z}\right]. \tag{A.1}$$

Writing the derivatives of the unit vectors explicitly in terms of the infinitesimal variation Δα,

$$\frac{1}{r^2}\frac{\partial^2}{\partial\alpha^2}\vec{M} = \frac{1}{r^2}\left[M_r\frac{\partial}{\partial\alpha}\left(\frac{|\hat{r}|\ \Delta\alpha\ \hat{\alpha}}{\Delta\alpha}\right) + M_\alpha\frac{\partial}{\partial\alpha}\left(\frac{-|\hat{\alpha}|\ \Delta\alpha\cdot\hat{r}}{\Delta\alpha}\right)\right]. \tag{A.2}$$

Repeating the procedure,

$$\frac{1}{r^2}\frac{\partial^2}{\partial\alpha^2}\vec{M} = -\frac{1}{r^2}\left(M_r\ \hat{r} + M_\alpha\ \hat{\alpha}\right). \tag{A.3}$$

The resulting exchange energy density is then, from Eqs. (2.19) and (2.20),

$$dE_{x\alpha} = \frac{A}{M_s^2}\left(\frac{M_r\hat{r}+M_\alpha\hat{\alpha}}{r^2}\right)\cdot\vec{M} = \frac{A}{M_s^2 r^2}\left(M_r^2 + M_\alpha^2\right). \tag{A.4}$$

Since $M_s = |\vec{M}|$,

$$dE_{x\alpha} = \frac{A}{M_s^2 r^2} (M_s^2 - M_z^2) \tag{A.5}$$

and since $M_z = M_s \cos\theta$,

$$dE_{x\alpha} = \frac{A}{r^2} \sin^2\theta, \tag{A.6}$$

which has the same θ dependence as the uniaxial anisotropy energy density, Eq. (2.7).

BIBLIOGRAPHY

1. A. Aharoni, "Two-dimensional domain walls in ferromagnetic films. IV. Wall motion", J. Appl. Phys. 47, No. 7 (July 1976), pp. 3329-3336.

2. G.S. Almasi, "Gap-tolerant half-disk bubble device margins", IEEE Trans. Magnetics, MAG-14, No. 2 (Mar. 1978), pp. 40-45.

3. J.W. Bandler, "Numerical Methods of Optimization", course notes, Faculty of Engineering, McMaster University, March 1978; see also general references in numerical optimization, including [14].

4. T.G.W. Blake and E. Della Torre, "Micromagnetic analysis of S=1 magnetic bubbles with curvature effects", J. Appl. Phys. 50, No. 3 part II (Mar. 1979), pp. 2192-2194.

5. T.G.W. Blake and E. Della Torre, "Static and kinematic parameters of magnetic bubble walls having a horizontal Bloch line pair", J. Appl. Phys. 50, No. 11 part II (Nov. 1979), pp. 7868-7870.

6. T.G.W. Blake and C.C. Shir, "DOM: the simulation of flexible magnetic bubbles", IBM Research Division Report RJ2812(35728) (May 1980); accepted for publication in IEEE Trans. Magnetics.

7. T.G.W. Blake, C.C. Shir and Y.O. Tu, "Effects of finite anisotropy parameter Q in the determination of magnetic bubble material parameters", IBM Research Division Report RJ2834(36120) (June 1980).

8. F. Bloch, Z. Physik. 74 (1932), p. 295.

9. A.H. Bobeck and E. Della Torre, "Magnetic Bubbles", vol. XIV of "Selected Topics in Solid State Physics", ed. E.P. Wohlfarth, North-Holland, Amsterdam, 1975.

10. W.F. Brown, "Magnetostatic Principles in Ferromagnetism", Elsevier North-Holland, Amsterdam and New York, 1962.

11. W.F. Brown, "Micromagnetics", Wiley, New York, 1963; reprinted with corrections, 1978.

12. "Special issue honoring William Fuller Brown, Jr.", IEEE Trans. Magnetics, MAG-15, No. 5 (Sept. 1979).

13. R. Bulirsch, "An extension of the Bartky-transformation to incomplete elliptic integrals of the third kind", Numer. Math. 13, (1969), p. 266.

14. D.A. Calahan, "Computer Aided Network Design", revised edition, McGraw-Hill, New York, 1972.

15. J.A. Cape and G.W. Lehman, J. Appl. Phys. 42 (1971), p. 5732.

16. H. Chang, ed., "Magnetic Bubble Technology", IEEE Press, 1975; see also IEEE Intermag Conf. Proc. and AIP Magnetism and Magnetic Materials Conf. Proc. of later years.

17. S. Chikazumi, "Physics of Magnetism", Wiley, 1964.

18. M.I. Darby and B.K. Middleton, "Energies of circular domain walls", J. Phys. D: Appl. Phys., 6 (1973), pp. 116-122.

19. W.J. DeBonte, "Theory of the static stability of thick-walled cylindrical domains in uniaxial platelets", AIP Conf. Proc. No. 5, Magnetism and Magnetic Materials - 1971, AIP, 1972, pp. 140-144.

20. W.J. DeBonte, "Properties of thick-walled cylindrical magnetic domains in uniaxial platelets", J. Appl. Phys. 44, No. 4 (April 1973), pp. 1793-1797.

21. W.J. DeBonte, "Twisted domain wall structure for stripe domains in bubble films", IEEE Trans. Magnetics, MAG-11, No. 1 (Jan. 1975), pp. 3-11.

22. E. Della Torre and C.V. Longo, "The Electromagnetic Field", Allyn and Bacon, Boston, 1969.

23. E. Della Torre, C. Hegedus and G. Kadar, "Wall structure of cylindrically symmetric magnetic domains", AIP Conf. Proc. No. 29, Magnetism and Magnetic Materials - 1975, pp. 89-90.

24. E. Della Torre, "Numerical micromagnetic calculations", IEEE Trans. Magnetics, MAG-15, No. 5 (Sept. 1979), pp. 1225-1228.

25. D.C. Fowlis and J.A. Copeland, "Rapid method for determining the magnetization and intrinsic length of magnetic bubble domain materials", AIP Conf. on Magnetism and Magnetic Materials, AIP Conf. Proc. Series, No. 5 (1972), pp. 240-243.

26. R.W. Hamming, "Numerical Methods for Scientists and Engineers", second edition, McGraw-Hill, New York, 1973.

27. C.J. Hegedus and E. Della Torre, "On the efficient calculation of bubble functions", J. Appl. Phys. 49, No. 2 (Feb. 1978), pp. 942-943.

28. C.J. Hegedus, G. Kadar and E. Della Torre, "Demagnetization matrices for cylindrical bodies", J. Inst. Math. and its Appl. 24 (1979), pp. 279-291.

29. G.R. Henry and B.R. Brown, "Calculation of micromagnetic structure by a relaxation method", AIP Conf. Proc. No. 24, Magnetism and Magnetic Materials - 1974, pp. 751-752.

30. A. Hubert, "Statics and dynamics of domain walls in bubble materials", J. Appl. Phys. 46, No. 5 (May 1975), pp. 2276-2287.

31. W.S. Ishak and E. Della Torre, "BUBMAT", IEEE Trans. Magnetics, MAG-13 No. 2 (Mar. 1977), pp. 964-965; W.S. Ishak and E. Della Torre, "BUBMAT2 - package for bubble material parameters calculation", Faculty of Engineering, McMaster University, Hamilton, Ont., Canada, Report SOC-181 (Oct. 1977); W.S. Ishak and T.G.W. Blake, "BUBMAT3", private communication on further refinements of the calculation, 1978-1979.

32. G. Kadar, C.J. Hegedus and E. Della Torre, "Cylindrical demagnetization matrix", (Fortran program), IEEE Trans. Magnetics, MAG-14 No. 4 (July 1978), pp. 276-277.

33. R. Kirchner and W. Doring, "Structure and energy of a Néel wall", J. Appl. Phys. 39, No. 2 (1 Feb 1968), pp. 855-856.

34. A.E. LaBonte, "Two-dimensional Bloch-type domain walls in ferromagnetic films", J. Appl. Phys. 40, No. 6 (May 1969), pp. 2450-2458.

35. Y.S. Lin and Y.O. Tu, "Micromagnetic solutions for bubble domains", Appl. Phys. Lett. 18, No. 6 (Mar. 1971), pp. 247-249.

36. Y.S. Lin, D.B. Dove, S. Schwarzl, C.C. Shir, "Charged wall behavior in 1-μm bubble implanted structures", IEEE Trans. Magn., MAG-14 No. 5 (Sept. 1978), pp. 494-499.

37. A.P. Malozemoff and J.C. Slonczewski, "Magnetic Domain Walls in Bubble Materials", Academic Press, New York, 1979.

38. G.M. Nedlin, "Shape of bubbles", AIP Conf. on Magnetism and Magnetic Materials (Nov. 1978), paper 2B-7.

39. E. Schlömann, "Twisted domain structure in bubble films", Appl. Phys. Lett. 21, No. 5 (1 Sept 1972), pp. 227-229.

40. E. Schlömann, "Domain walls in bubble films. I. General theory of static properties", J. Appl. Phys.. 44, No. 4 (April 1973), pp. 1837-1849.

41. E. Schlömann, "Domain walls in bubble films. II. Static properties of thick films", J. Appl. Phys. 44, No. 4 (April 1973), pp. 1850-1854.

42. E. Schlömann, "Domain walls in bubble films. III. Wall structure of stripe domains", J. Appl. Phys. 45, No. 1 (Jan. 1974), pp. 369-373.

43. C.C. Shir, "Computations of the micromagnetic dynamics in domain walls", J. Appl. Phys. 49, No. 6 (June 1978), pp. 3413-3421.

44. C.C. Shir, private communications, 1979-1980.

45. M. Shirobokov, "On the theory of the mechanism of magnetization of ferromagnetics", Zh. Eksp. Teor. Fiz. 15, No. 1-2 (1945), pp. 57-76.

46. J.C. Slonczewski, "Dynamics of magnetic domain walls", Intern. J. Magnetism 2 (1972), pp. 85-97.

47. J.C. Slonczewski, "Theory of domain-wall motion in magnetic films and platelets", J. Appl. Phys. 44, No. 4 (April 1973), pp. 1759-1770.

48. J.C. Slonczewski, "Theory of Bloch-line and Bloch-wall motion", J. Appl. Phys. 45, No. 6 (June 1974), pp. 2705-2715.

49. R.F. Soohoo, "Magnetic Thin Films", Harper and Row, New York, 1965.

50. A.A. Thiele, "The theory of cylindrical magnetic domains", Bell Syst. Tech. J. 48, No. 10 (Dec. 1969), pp. 3287-3335.

51. A.A. Thiele, "Device implications of the theory of cylindrical magnetic domains", Bell Syst. Tech. J. 50 (Mar. 1971), pp. 727-775.

52. A.A. Thiele, "Applications of the gyrocoupling vector and dissipation dyadic in the dynamics of magnetic domains", J. Appl. Phys. 45, No. 1 (Jan. 1974), pp. 377-393.

53. Y.O. Tu, "Determination of magnetization of micromagnetic wall in bubble domains by direct minimization", J. Appl. Phys. 42, No. 13 (Dec. 1971), pp. 5704-5709.